# STRUCTURAL STUDIES OF HUMAN ENTEROVIRUSES

by

**Jianing Fu**

**A Dissertation**

*Submitted to the Faculty of Purdue University*

*In Partial Fulfillment of the Requirements for the degree of*

**Doctor of Philosophy**


Department of Biological Sciences

West Lafayette, Indiana

August 2020

# THE PURDUE UNIVERSITY GRADUATE SCHOOL
# STATEMENT OF COMMITTEE APPROVAL

**Dr. Richard J. Kuhn**
Department of Biological Sciences

**Dr. Nicholas Noinaj**
Department of Biological Sciences

**Dr. Cynthia V. Stauffacher**
Department of Biological Sciences

**Dr. Angeline Lyon**
Department of Chemistry

**Dr. Michael G. Rossmann**
Department of Biological Sciences

**Approved by:**
Dr. Janice P. Evans.

Praise Father Lord for His Grace

To my parents,
for their continuous love and support.

# ACKNOWLEDGMENTS

I would like to express my sincere appreciation to Dr. Michael G. Rossmann. I started working in the Rossmann Lab my junior year at Purdue. After getting my bachelor's degree, I joined the Ph.D. program in 2016 and was a graduate student in Michael's lab until he passed away in May 2019.

I am fortunate that I began my research with Michael. He taught me to be curious, strong, persistent, focused and humble about science. I still remember when he initially described different projects and we discussed which project I should start. Then he checked the progress of my work and guided me on what to do next, he read my first abstract and suggested how to make the writing better… and so on. I thank Michael, deeply, for these unforgettable, wonderful, priceless and warm memories; for the opportunities; for his generous guidance and help; for always being friendly and gentle (even when he was not feeling well); and for trusting, supporting and defending me.

I especially want to thank Michael for times when he treated me like a family member. He told me personal stories such as about the Second World War and his traveling experiences. He remembered my birthday (and asked the group to sing Happy Birthday) and had also told me he would teach me chess. As the last Rossmann-Lab Ph.D. student, it was sad and difficult to lose him, but I am both lucky and honored to have been his student. Thank you, Michael, for teaching me, for caring about me, and for providing many lovely and unforgettable memories. You are deeply missed, both personally and professionally.

My deepest gratitude goes to my original committee chair and current principle investigator, Dr. Richard J. Kuhn, who allowed me to complete my Ph.D. studies as his graduate student. I still take comfort in the hug he gave me soon after Michael passed away, it was a great consolation and offered encouragement. Since then, Richard has worked with me on projects and in planning for my future career as well as helping me through school life in general. Having Richard as my advisor has made me feel safe during a time of uncertainty.

Richard, a well-established virologist, has a keen grasp of project ideas and holds a wealth of knowledge. He is also clear thinking and articulate. He has trained me to be an explorer and equipped me with skills essential to a successful scientist, including aspects of oral communication and presentation, scientific writing, critical and creative thinking, poster design, and the planning of experiments. I am fortunate to have benefited from Richard's oversight while I explored science and learned to overcome associated obstacles.

It is hard to express enough thanks to Dr. Thomas Klose, a senior scientist and cryo-EM expert. To me, Thomas is a humble and outstanding scientist, a talented teacher, a great friend and a friendly big brother who always provides generous help and guidance. He has taught me so many things, particularly electron microscope data collection and data processing. With his assistance, I was able to solve my first virus structure. He also provided comments and suggestions toward improving manuscripts, figures and other scientific text as well as patiently explaining many confusing concepts. Thank you, Thomas, for your help, your time and your patience.

I am also grateful to have had Dr. Nick Noinaj, Dr. Angeline Lyon and Dr. Cynthia V. Stauffacher as my committee members. They provided inspiration as well as invaluable comments and suggestions during individual meetings, preliminary exam and committee meetings. I thank each of them for their patience, guidance and support. Thank you also to Dr. Wen Jiang who first described cryo-electron microscopy to me and trained me to solve my first structure using online practice data. I am also thankful for the experiences shared with faculty I've worked under during my time at Purdue: Drs. Jeffery R. Lucas, Mark Browning and Sean E. Humphrey.

Thank you to my outside collaborators, particularly Dr. Frank van Kuppeveld and his group at Utrecht University (The Netherlands) and Dr. James C. Crowe and his group at Vanderbilt University. I thank Angela Jia (Johns Hopkins Medicine) for her guidance, both scientific and personal. I am also grateful to numerous established scientists, many of whom were once Rossmann Lab member themselves, who generously provided me with invaluable input and support at key times. I am further grateful for the support of many Purdue friends and colleagues throughout my graduate studies. This includes a wonderfully helpful and supportive Rossmann

Lab family, a welcoming Kuhn Lab group, and numerous other Biology faculty, staff and students who provided me with their support, assistance and friendship.

My life in graduate school would not have been fun without the many new friends I met in school and at church. I am particularly thankful to know Rui Yan, Jessica Monjaras, Kristi McElmurry, Paul and Arleen Mullikin, Amy Chenchen Xu, Steve Wilson, Sheryl Kelly, Nanami Miyazaki, Heejeong Kim, Aaron Gall, Chen Sun, Dan Xie, Runrun Wu, Yang Yi, Zhe Sun, Chennai Li, Leang- Chung Choh and Elaine Mihelic. These friendships have influenced and enriched my life. I would also like to express my appreciation to my hometown friends: Tianyi Huang, Li Han, Shimeng Li, Yu Zhao and Sophia Wen. Each of these friendships has lasted more than 10 years and, even though we now reside far away from each other, we still care about and cherish each other. Thank you all for your trust, encouragement, advice and for being there for me. I am also thankful to have shared this time with my rabbit friend who has been my special companion and security blanket.

I cannot sufficiently thank my family (parents, grandparents, aunts, uncles and cousins) for a lifetime of thoughtful kindness, love and support. Most importantly, however, I thank my parents. My education and research work were possible only with their encouragement and support. I thank them for their constant care, trust and love. Thank you for sharing my happiness and sadness; for innumerable video chats and online messages since my arrival at Purdue; for providing a warm, peaceful and safe harbor; and for being the best parents and wonderful friends. I am grateful and honored to be your daughter. I appreciate you. I love you.

# TABLE OF CONTENTS

# LIST OF TABLES

# LIST OF FIGURES

# ABBREVIATIONS

| | |
|---|---|
| 2D | Two-dimensional |
| 3D | Three-dimensional |
| β (B, C, D…) | β-strand (B, C, D…) |
| Å | Angstrom |
| ℃ | Celsius |
| μm | Micrometer |
| μL | Microliter |
| AFM | Acute flaccid myelitis |
| A-particle | Altered particle |
| ATCC | American Type Culture Collection |
| Cα | Alpha carbon |
| CAR | Coxsackievirus and adenovirus receptor |
| CDR | Complementarity-determining region |
| CNS | Central nervous system |
| Cryo-EM | Cryo-electron microscopy |
| C-terminal (terminus, termini) | Carboxy terminal (terminus, termini) |
| CTF | Contrast transfer function |
| CVA | Coxsackievirus group A |
| CVB | Coxsackievirus group B |
| DAF | Decay-accelerating factor |
| DMEM | Dulbecco's Modified Eagle Medium |
| DMSO | Dimethyl sulfoxide |
| DNase | Deoxyribonuclease |
| ECV | Echovirus |
| EDTA | Ethylenediaminetetraacetic acid |
| EV | Enterovirus |
| FSC | Fourier shell correlation |
| HEPES | 4-(2-hydroxyethyl)-1-piperazineethanesulfonic acid |

| | |
|---|---|
| HI-FBS | Heat inactivated fetal bovine serum |
| HRV | Human rhinovirus |
| ICAM | Intercellular adhesion molecule |
| Ig-like | Immunoglobulin-like |
| IRES | Internal ribosome entry site |
| mAb | Monoclonal antibody |
| mg | Milligram |
| mL | Milliliter |
| mM | Millimolar |
| MOI | Multiplicity of infection |
| NIm | Neutralizing immunogen |
| N-terminal (terminus, termini) | Amino terminal (terminus, termini) |
| NTR | Noncoding region |
| NEAA | Non-essential amino acids |
| ORF | Open reading frame |
| PBS | Phosphate-buffered saline |
| PV | Poliovirus |
| RD | Rhabdomyosarcoma |
| RPM | Revolutions per minute |
| r.m.s.d | Root-mean-square deviation |
| RNA | Ribonucleotide acid |
| Tris | Tris(hydroxymethyl)aminomethane |
| VP | Viral polypeptide/protein |
| VPg | Viral protein genome-linked |
| WIN | Winthrop |

# ABSTRACT

*Enterovirus* (EV), a genus within the *Picornaviridae* family, contains icosahedral positive-stranded RNA viruses linked to different human and mammalian diseases with a variety of symptoms ranging from the common cold to central nervous system infection. An important member within this genus is EV-D68. Unlike many enteroviruses that use the gastrointestinal tract as the transmission and propagation route, EV-D68 infects the respiratory tract and causes respiratory illness, especially in children. Severe infections of EV-D68 also lead to acute flaccid myelitis (AFM), a polio-like neurological disease. Especially in recent years, EV-D68 has been on a global upswing. However, no antiviral interventions against EV-D68 infection have been developed to date. Antibodies neutralizing EV-D68 have significant vaccine and therapeutic potentials. Here, the structures of the immune complex between EV-D68 and the Fab molecules of EV-D68 human monoclonal antibodies have been reconstructed using cryo-electron microscopy (cryo-EM). These structures show two Fab binding loci on the virion surface as well as the essential amino acids involved in binding. In addition to antibodies, a drug candidate against EV-D68 has been investigated in this work as an antiviral strategy. It is likely that this drug blocks viral entry through binding in the hydrophobic pocket underneath the viral protein 1, the largest structural protein of EV-D68. Furthermore, the morphogenesis of EV-D94, another causative virus of polio-like disease, which is closely related to EV-D68 with 85% sequence identity, has been investigated using cryo-EM. Compared to EV-D68, the shape of the canyon and the loops containing the immunogenic recognition sites are different in EV-D94. The structures of each of the three stages of EV-D94 particles (the full native virion, the uncoating intermediate, and the empty virion) were identified and delineate the viral uncoating process. These findings reveal useful knowledge and new insights to develop treatments against human EVs.

# 1. INTRODUCTION

## 1.1 Overview of Enterovirus infection

*Enterovirus* (EV) is a genus within the *Picornaviridae* family, which contains a large number of small, non-enveloped, positive-sense single-stranded RNA viruses with an icosahedral capsid of approximately 300 Å in diameter[1], [2]. Many of these small viruses are closely associated with human diseases (**Table. 1.1**). The clinical progression of an EV infection can be characterized by poliomyelitis, a neurological complication represented by muscle weakness and flaccid paralysis which could be irreversible or even fatal[3]. In the late 19$^{th}$ century both Europe and the United States suffered major outbreaks of poliomyelitis, which then continued as a worldwide health issue until late 20$^{th}$ century. The origin of this disease is Poliovirus (PV), a virus which is able to infect the central nervous system (CNS)[4]–[6]. In addition to poliomyelitis, symptoms of PV infections also include aseptic meningitis and encephalitis[3], [7], [8]. However, scientific research soon thereafter revealed that not only PV (and there are 3 serotypes), but also many EVs, which are phylogenetically related to PV, can be responsible for the similar clinical features.

The isolation of coxsackievirus group A (CVA) occurred first during a poliomyelitis outbreak in mid-20$^{th}$ century, soon followed by the discoveries of coxsackievirus group B (CVB) and echovirus (ECV). On the basis of their pathogenesis in cell culture and the diseases caused in mice and humans, these three viruses, together with PV, comprised the original classification of EV[6], [9]. The virus diversity within each species, categorized as serotypes, were investigated and evaluated based on surface antigens and animal raised antisera. However, this method proved too laborious as more and more EVs were discovered[6], [10]. Thus, in the current classification scheme, members within an EV genus are sorted into 15 species depending on certain sequence similarity of the structural and non-structural protein regions[6], [11], [12]. Seven species are specifically infectious to humans, including EV-A, EV-B, EV-C, EV-D, human rhinovirus (HRV)-A, HRV-B and HRV-C[13], [14].

Nowadays, other than PV, numerous EVs, such as EV-A71, EV-D68, CV-A16, ECV-21, and HRV-1A[14], [15], are present worldwide with symptoms ranging from mild infections with

common cold and conjunctivitis to severe or even potentially fatal infections causing illnesses like hand foot and mouth disease, inflammatory cardiomyopathy and polio-like CNS lesions (**Table 1.1**) [6], [14], [16]–[19]. In addition, the neurological complications caused by EV infections most frequently occur in children with over 80 percent of EV patients under 15 years of age representing the key disease group [6], [19]. The classical transmission pathway of EVs is the oral-fecal route[6]. Many EVs, like polio- and coxsackieviruses, are able to propagate in the alimentary tract due to their stability at low pH[6], [7]. Some acid-sensitive EVs, such as EV-D68 and the HRVs, have a predilection for the respiratory tract[14], [20], [21]. Interestingly, some EVs, like EV-D94, are able to proliferate in pancreatic cells, making them potentially diabetogenic[22].

## 1.2 Virion Structure

### 1.2.1 Background of EV structural studies

Our current understanding of picornavirus structure is based on the three-dimensional (3D) structures of two EVs: PV-1 and HRV-B14. The structures were solved in 1985 using X-ray crystallography[23], [24]. This method has since been broadly used in contemporary virology[14], [23]–[25]. The morphologies of different virion capsids, viral components and the virus-receptor interactions, such as the structures of EV-A71[26], [27], EV-D68[2] and CVA-9[28], as well as the virus-receptor complexes of CVA-21 with intercellular adhesion molecule (ICAM) 1[29] and ECV-7 and 12 with decay-accelerating factor (DAF)[30], [31], were all investigated using this method. However, for virus-protein complexes, solving the structures using X-ray crystallography is not a simple task, and it was usually hard to obtain a resolution at atomic levels[32].

**Table 1.1**
**Typical clinical features and demographics of different EV infections.**

| Diseases | High Risk Age Groups | Notable Causative or Related EV and Classification | | References |
|---|---|---|---|---|
| Poliomyelitis | Children <5 years old | PV-1, 2, 3 | EV-C | [6], [7], [33] |
| Polio-like CNS complications | Children, juveniles and young adults<22 years old | EV-A71 | EV-A | [6], [34]–[39] |
| | | EV-D68 | EV-D | |
| | | EV-D94 | | |
| | | EV-D70 | | |
| Encephalitis and meningitis | Children and juveniles between 5-14 years old | CVA-9 | EV-B | [6], [17], [34], [39] |
| | | ECV-21 | | |
| | | EV-A71 | EV-A | |
| Cardiomyopathy | Young adults between 20-39 years old | CVB-3 | EV-B | [6], [40] |
| Hand, foot and mouth disease | Children <10 years old | EV-A71 | EV-A | [19], [34], [41]–[43] |
| | | CVA-16 | | |
| | | CVA-10 | | |
| Common cold and related respiratory illness | Infancy to early childhood | HRV-C15 | RV-C | [44]–[47] |
| | | EV-D68 | EV-D | |
| Acute hemorrhagic conjunctivitis | Juveniles and young adults | CVA-24 | EV-C | [6], [48]–[53] |
| | | EV-D70 | EV-D | |
| | | ECV-7 | EV-B | |
| Diabetes | Potential high risk in children | CVB-4 | EV-B | [6], [22], [54]–[56] |
| | | EV-D94 | EV-D | |

Nowadays, many virologists are using cryo-EM to study virus structure. In fact, electron microscopy was the traditional way of observing the shapes and sizes of viruses and the interactions between viruses and hosts before X-ray crystallography became widely used[32], [57]. For example, in the 1970s 3D virus structures were produced based on negative stained samples. However, uneven staining and distortions of the sample due to the staining limited the reconstruction quality. These issues were avoided by the use of cryo-EM, which preserves viruses in vitreous ice by flash-freezing them at liquid nitrogen temperatures[32], [58]. By using cryo-EM, the electron density maps of not only EVs, but also many larger icosahedral viruses, often can be resolved to atomic levels and sometimes even beyond 3Å resolution[59]–[62]. In particular, for the virus-receptors and virus-antibodies complexes, a higher resolution, usually better than 4 Å, is also achievable through cryo-EM[32], [61], [63]–[65].

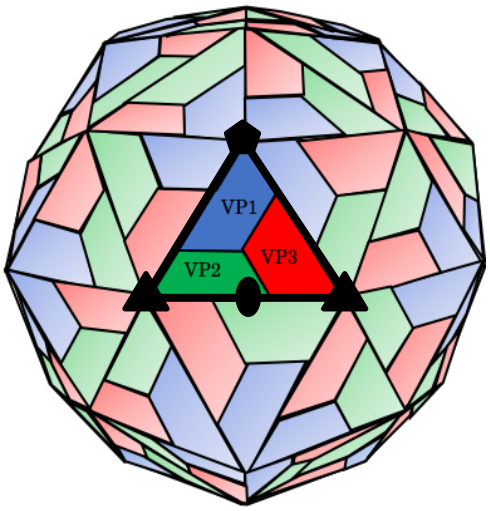


**Fig. 1.1 A schematic view of an EV capsid.** The VP1, VP2 and VP3 are colored in blue, green and red, respectively. An asymmetric unit is outlined in a black triangle, and VP1, VP2 and VP3 are emphasized using darker colors. The pentagon, oval and triangles indicate the five-fold, two-fold and three-fold axes, respectively. The same color scheme and geometric labeling are used throughout the thesis.

### 1.2.2 Capsid framework

A mature EV virion has an icosahedral capsid with a peripheral diameter of about 300 Å following pseudo T=3 symmetry[1], [14], [23], [24], [32]. The T number, fully named as the triangulation number, represents the quantity of protein subunits that are structurally similar to each other within one asymmetric unit[66]. The external shell of an EV capsid is built using 60 copies of three structural viral polypeptides (VPs) : VP1, VP2 and VP3, each about 35 kDa in size[1], [32] **(Fig. 1.1)**. The three structural proteins are divergent in sequence but conserved in topology: a wedge-shaped 8-stranded beta (β)-barrel jelly roll motif that is composed of two β-sheets and two helices. Each β-sheet is made of four anti-parallel β-strands. The β-strands for the larger and twisted β-sheet are labeled as B, I, D and G, whereas the β-strands for the smaller β-sheet are labeled as C, H, E and F [14], [32], [66], [67] **(Fig. 1.2)**. The β-strands

are connected by loops, and the sequence variability between the loops provide structural distinctions in different EVs. Some of the hypervariable loops that decorate the external shell serve as antigenic sites[1], [14]. The internal side of an EV capsid is coated with 60 copies of VP4[1], [14], [23], [24], each about 4 kDa in size[32].

### 1.2.3 Inner capsid interactions

Interior protein interactions are essential to the stability of an EV capsid. A protein network underneath the capsid surface near each three-fold axis contributes to the stability between the capsid pentamers[14], [67]. A β-sheet structure is formed not only by the C, H, E and F β-strands of VP3 and some residues on the N-termini of VP1[14], [67], but also the N-terminal extensions of VP2 which bind to the RNA genome and associated with the carboxy (C)-termini of VP4 in the meantime[67].

Around each five-fold axis, five copies of the amino (N)-termini of VP3 form a 5-stranded cylindrical structure. This structure also interacts with the N-termini of VP1 and VP4, which contributes to pentamer stability. In particular, VP4 is myristylated[1], [14], [67], [68], and presumably makes contacts with the cell membrane, assisting in RNA dissociation from the capsid during the uncoating process which usually happens during viral entry or antigenic conversion[1], [68]–[70]. The myristylation of VP4 also contributes to capsid stability. Previous research found that for PV-1 and many picornaviruses, myristylation occurs at the N-terminal glycine residue of VP4, and the myristic acid directly interacts with the VP3 cylindrical structure[14], [68]. In addition, even though the first 25-28 amino acids on N-terminus of VP4 are disordered[1], [71], [72] for HRV-B14, HRV-A1 and HRV-A16, a density corresponding to a myristate moiety is present close to the center of each pentamers.

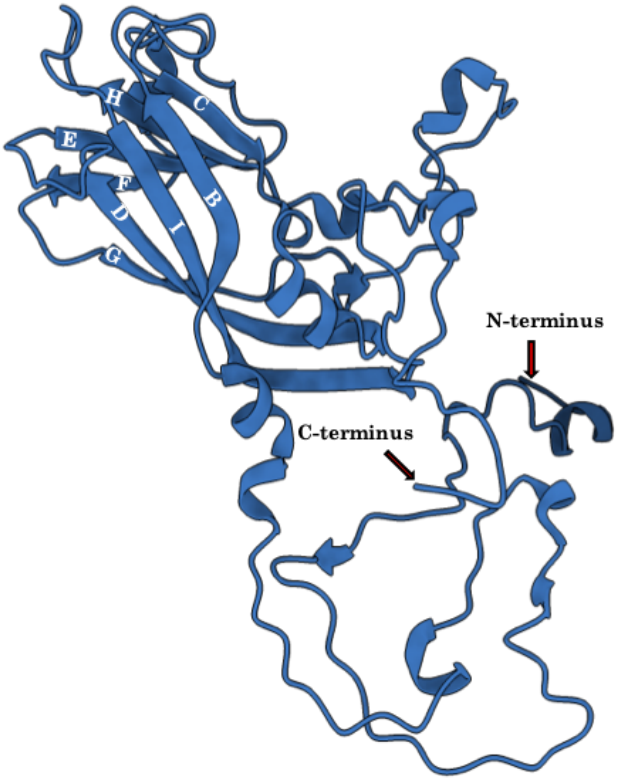


**Fig. 1.2. A typical β-barrel jelly roll motif shown in ribbon diagram.** This figure is generated by UCSF ChimeraX[73] using the VP1 structure of EV-A71(PDB: 3vbs)[27].The two sets of anti-parallel β-strands are labeled with BIDG and CHEF. The N- and C-termini are marked with red arrows.

### 1.2.4 Capsid dynamics

The N-termini of VP1 and VP4, even though deeply buried, are sometimes exposed to the surface, resulting a repeated structural expansion and contraction. This process is called "breathing"[14], [74]–[76]. Previous research found that antibodies against a portion of the VP1 N-terminus that is usually located inside the virus and against VP4 were able to neutralize PV-1 particles. This process is reversible as viral infectivity is recovered after disruption of antibody-virus complexes by freezing, indicating a reinternalization of the exposed VP1 and VP4 portions[77]. Similar dynamics are also found in HRV-B14[74], [78]. The extrusion of VP4 in CVB-4 as well as the extrusion of the N-termini of VP1 and VP3 in both CVA-9 and swine vesicular disease virus (EV-B species) were later described, suggesting that the "breathing" process is common to many EVs[78]–[81]. This interesting "breathing" phenomenon explaining

transient and reversible movements has been proposed to be relevant to viral entry and genome release[77], [82], [83].

### 1.2.5 Surface features

The surface of an EV is not flat. At each five-fold axis, residues on VP1 protrude from the surface and extend up to 165 Å away from the virus center forming a plateau region[24]. The plateau region is surrounded by an important hallmark of EVs: the "canyon"[14], [23], [24]. This canyon, just as the name implies, is a deep depression on the surface of an EV virion with a depth about 25 Å and a width about 12-30 Å **(Fig. 1.3A)**[23]. The north rim of the canyon is formed by VP1, and the south rim of the canyon is formed by VP2 and VP3 **(Fig. 1.3B)**. Specially, the GH loop of VP1 plays a role in the formation of not only the canyon floor, but also part of the south rim together with the C-termini of VP1 and VP3[1]. The canyon is hypothesized to be the site for host cell receptor binding[1], [14], [23], [84]. Another broad and elevated region that stretches about 150 Å from the virus center is formed at each three-fold axis by residues on VP2 and VP3. The surface height around each two-fold axis, however, is much lower which causes a disconnect between the two neighboring elevated regions **(Fig. 1.3A)**[24].

The capsid surface is decorated by loops connecting the β-strands of the three larger capsid proteins and their C-termini. Some of the hypervariable loops contains antigens that antibodies recognize and bind. These antigenic sites were first characterized in HRV-B14 back in 1985 and 1986 using monoclonal antibodies and virus mutants [23], [85]–[87]. The first group of sites are located on the loops between β-strands (β)B and βC of VP1 and VP3 and are labeled N-AgI and N-AgII[88]. These were later changed into neutralizing immunogen (NIm)-IA and NIm-III in order to represent that they locate on VP1 and VP3. In addition, the carboxyl ends of βB and βD correspond to the NIm-IB site, and the most external part of a large extended loop between βE and βF of VP2 corresponds to the NIm-II site[23]. The four NIm sites are located on the canyon rim **(Fig. 1.3B)**. Other than these NIm sites, the N-termini of the internal buried structural proteins, which may be exposed to the capsid surface during the breathing, are also potential immunogens[78]–[81].

### 1.2.6 Canyon hypothesis

The canyon itself was proposed and later confirmed as the host cell receptor binding site, with canyon formation an apparent strategy that viruses use to protect the receptor binding site in a surface crevice that is hard for antibodies to access[23], [84]. The amino acids lining the canyon are much more conserved than the amino acids exposed on the virus surface[84], and mutagenesis of the amino acids at the canyon base changes the affinity of receptor binding[89]. Interestingly, viruses that infect plants, which have no immune systems, tend to have flatter protrusion and depression on their surface compared to animal viruses[1]. This hypothesis has also been proven using many virus-receptor structures, including HRV-B14, HRV-A16, CVA-21 and CVA-24 in complexes with ICAM-1[29], [90], [91], CVB-3 in complex with coxsackievirus and adenovirus receptor (CAR)[92], PV-1 in complex with poliovirus receptor[93] and so on. Receptor binding into the canyon, the primary and most essential step of EV infection, triggers conformational change and promotes uncoating and the release of the genome[82]. Even though the canyon region is used as the receptor binding site for the majority of EVs, there are still exceptions. For example, the low-density lipoprotein binds to some HRV-A viruses, like HRV-A2, at the five-fold plateau regions[82], [94], [95]. Another example is the structure of HRV-C15 in complexes with cadherin-related protein 3 which showed that this receptor binds to the viral surface around the three-fold axis[96].

### 1.2.7 Hydrophobic pocket

A hydrophobic pocket **(Fig. 1.3B,C)** is found within the VP1 core underneath the canyon floor[1], [14], [82]. Many EV structures, such as PV-1, EV-A71, EV-D68, CVA-21 and CVB-3[14], have electron density corresponding to a lipid molecule within the pocket, called the pocket factor, that is closely associated with hydrophobic side chains[67]. However, not all EV structures have pocket factor densities, such as HRV-B14[14], [71], [72] and EV-D68 US/MO/14-18947 circulating strain[97], indicating a weak binding[1] or absence of the pocket factor[14], [97]. Moreover, the length of the pocket factor varies in different EVs **(Table. 1.2)**.

**Table 1.2 Pocket factor length for typical EVs.**

| EV | Pocket factor length | References |
|---|---|---|
| PV-1 | 18Carbon long (C) | [67] |
| CVA-16 | 18C | [41] |
| CVA-10 | 18C | [43] |
| EV-A71 | 12C | [26] |
| CVB-3 | 16C | [98] |
| ECV-7 | 12C | [30] |
| HRV-A16 | 8C | [71] |
| HRV-B14 | Absent or weak binding | [1], [23] |
| EV-D68 | 10C | [2] |

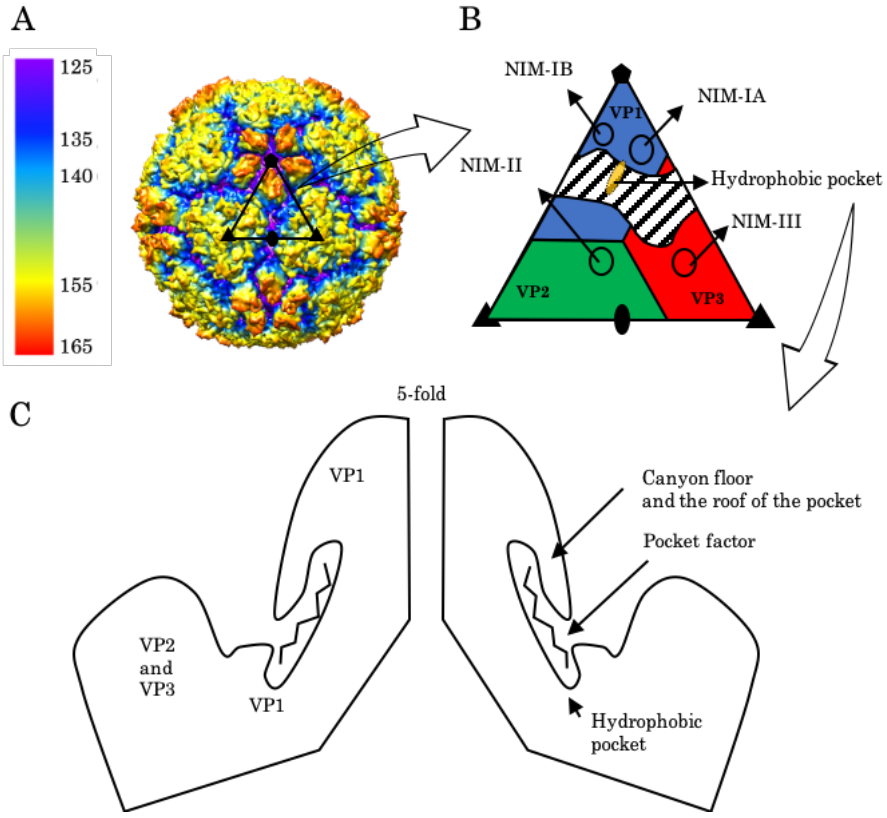


**Fig. 1.3. Representations of the essential EV features. (A)** A schematic model of HRV-B14 (PDB: 1ncq[99]) colored radially. This panel is generated with UCSF Chimera[100]. The coloring of the model is based on the radius from the virus center (in Å). The "plateau", "canyon" and the "broad and elevated region" are distinguished based on color. **(B)** A schematic diagram of the canyon in an asymmetric unit. The canyon is shown as a shaded region. The hydrophobic pocket underneath the canyon is illustrated by an orange oval. The four neutralizing immunogens are outlined in circles. This figure is based on the following references: [1], [86]. **(C)** Side view of the canyon region. This figure is made based on the following references: [1], [82].

The GH loop of VP1 which forms the canyon floor is also the roof of the pocket **(Fig. 1.3C)**, indicating a potential competing relationship between the pocket factor and receptor. It has been proposed that the pocket factor stabilizes the virus capsid before a virus binds to the receptor and, once binding occurs, the pocket factor is expelled from the capsid in order to initiate the uncoating process[1], [101]. A series of Winthrop (WIN, named after the drug company that developed them – Sterling-Winthrop) compounds[102], which are antivirals with higher binding affinity to the pocket than naturally existing pocket factors, are able to occupy the pocket and stabilize capsid conformation from uncoating and, in some cases, block the host cell receptor attachment[1], [82], [84], [85], [102]–[104]. For instance, WIN compounds were found to replace the pocket factors of PVs and HRV-1A which causes inhibition of the uncoating process. Furthermore, a WIN compound is able to easily occupy the pocket space in wild type HRV-14 that contains no or only a weakly bound pocket factor, where it contorts the shape of the pocket roof/canyon floor which affects receptor binding into the canyon[1], [105]. Other pocket binding inhibitors, such as vapendavir and pleconaril, have been developed against HRVs and have been found to be effective not only against HRVs, but are also inhibiting some EVs such as EV-A71 and EV-D68[2], [106]–[109].

### 1.2.8 Genome structure

The genomic material of an EV is a 7.5kb single, positive-stranded RNA molecule[14], [110]. The 5’ end of the RNA is capped with a protein called VPg (viral protein genome-linked), a primer for RNA synthesis[14], [111], [112]. The genome contains one open reading frame (ORF), which is flanked by a 5’-noncoding region (NTR) and a 3’-NTR. The 5’-NTR has an internal ribosome entry site (IRES) that promotes ribosome binding[14], [113]. The ORF encodes the viral polyprotein, which is processed and converted to various viral proteins after the translation of the viral proteases. Initially, the polyprotein is divided into three precursor proteins, P1, P2, and P3. The capsid proteins which form the virion structure, VP1-VP4, come from P1, whereas the other non-structural proteins that are required for protein processing and genome replication (such as the proteases 2A, 3C and 3CD, the RNA polymerase 3D and the RNA synthesis primer 3B which is the VPg protein) come from P2 and P3[14], [114]. In addition, 2A also cleaves cellular proteins[115], [116], and sometimes these are associated with human diseases[115]. The ORF is

followed by the 3'-NTR and a polyadenylation tail, and the latter found essential for viral infectivity[14]**(Fig. 1.4)**.

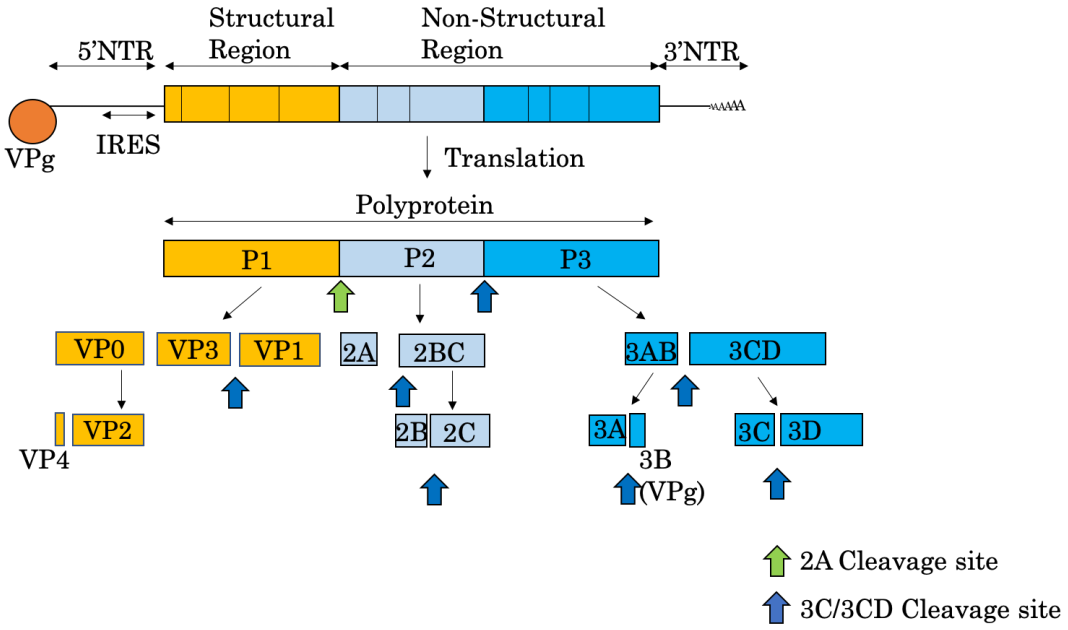


**Fig. 1.4. EV genome and processing of proteins.** The genomic material components are highlighted in this diagram. The RNA encodes the essential information of the structural and non-structural proteins, which are cleaved by the viral proteases. The 2A cleavage site is marked by a green arrow, whereas the 3C (or 3CD) cleavage site is marked by a blue arrow. This figure is drawn based on the following references: [14], [112].

## 1.3 Life cycle

### 1.3.1 Viral entry and uncoating

Attachment to the cell surface is the first step of EV infection and is primarily dependent on cell surface receptors. Specific receptors have been identified for some EVs.

Some receptors, such as ICAM-1, the receptor for 90 HRVs[117] and some coxsackieviruses-like CVA-21[29] and CVA-24[91], facilitate viral entry by binding to the canyon **(Fig. 1.5A)** using the most N-terminal immunoglobulin-like (Ig-like) domains, destabilizing the capsid and triggering uncoating and genome release[82]. In addition, ICAM-5, another member of the ICAM family, has been found to be the receptor of EV-D68[118]. Other than proteins, some glycan molecules also serve as entry receptors, for instance, sialic acid has been found to be the entry

receptor of EV-D68[119]. However, binding to sialic acid triggers pocket factor release but not uncoating, indicating the importance of an additional proteinaceous receptor, or a special chemical condition[76], [119].

Another type of receptor, DAF, promotes viral attachment to the host cell. The interactions between DAF and some EVs have high association and dissociation rates because of low binding affinity and do not lead to structural changes in virus particles, but probably promote attachment to other cellular factors[14]. The structures of DAF binding to ECV-7[30], [92], ECV-12[31], ECV-6[120] and CVB-3[121] also show that DAF binds near the two-fold axis **(Fig. 1.5B)** instead of the canyon. What DAF does in some EV infections is to accumulate viruses on the cell surface and bring viruses closer to the entry receptors[14], [82]. For example, CVB-3 binds to DAF at the beginning of infection, which triggers actin rearrangements and brings the virus to the tight junctions where the entry receptor CAR is hidden from the apical surface[82], [122].

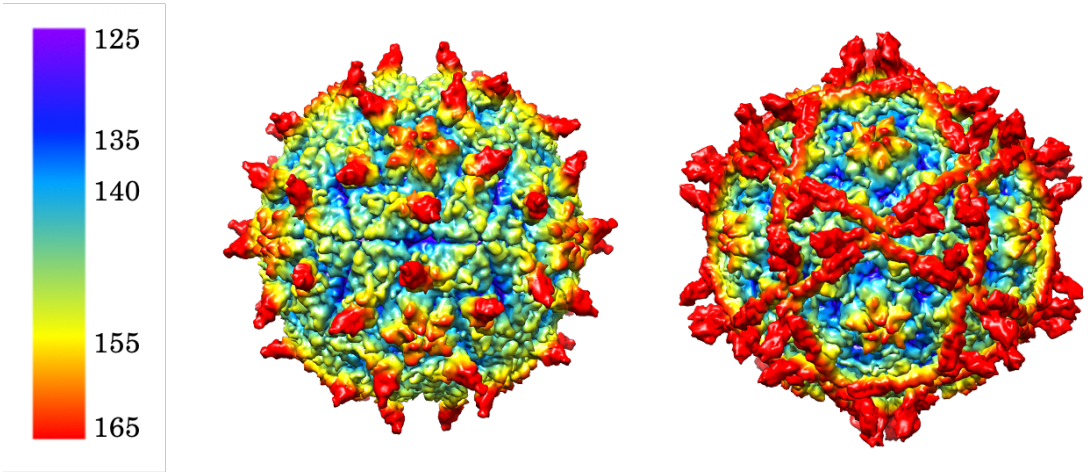


**Fig. 1.5. Comparison between EV entry and attachment receptors.** This figure is generated with UCSF Chimera[100]. (A) Schematic model of CVA-24 and the two most N-terminal domains of the entry receptor ICAM-1 (PDB: 6eit[91]). The entry receptor binds to the canyon region. (B) Schematic model of ECV-7 and full-length attachment receptor DAF (PDB: 3iyp[30]). Unlike the entry receptors that bind to the canyon, DAF binds near the two-fold axis and left the canyon region open. The models are colored radially.

After receptor binding, EVs are taken up by the cell through endocytosis. Previous studies show that the clathrin-mediated pathway, which is a commonly utilized cellular uptake strategy,

is used in the entry of many EVs like different HRVs and EV-A71[14], [82], [123]. Other EVs, such as CVB-3 and ECV-1, have been found to use the caveolin-mediated endocytic pathway[14], [82]. Receptor binding not only triggers endocytic uptake, but also induces uncoating, a process of important structural changes which are critical for genome release and the subsequent replication process. Once the entry receptor binds to the canyon, contacts between the receptor and the canyon floor VP1 GH loop destabilizes the capsid[76]. Dramatic conformational changes are then induced in the capsid framework, including the expulsion of the pocket factor, externalization of VP1 N-termini and the loss of VP4. These structural changes turn a native EV virion into an expanded altered (A)-particle, representing an intermediate stage before the EV particle can completely release its genome into the cytosol[14], [76], [82], [124]–[126]. For most of the EVs, receptor binding is the most critical determinant for this process. A recent study on EV-D68 also showed that during the uncoating process, the GH loop of VP3 is extended and interacts with the external VP1 N-terminal regions, which presumably facilitate the externalization of VP1 N-terminus. Furthermore, around each two-fold axis, some VP2 residues get displaced, which opens up a hole as a potential exit for the genomic RNA[97]. Importantly, for some EVs like HRVs and EV-A71 to become fully uncoated, endosomal low pH is another important uncoating requirement[14], [76], [127]. Specifically, in EV-D68, low pH is able to induce conformational changes from a native virion to an A-particle *in vitro* without receptor binding[97]. On the contrary, acid-stable EVs, such as the PVs, do not require low pH as an uncoating trigger[128].

An A-particle, as an uncoating intermediate, has higher affinity to the host cell membrane due to the amphipathic property of the VP1 N-termini[14], [125], [129]. Importantly, it is hypothesized that the externalized VP1 N-termini and VP4 form pores on the cell membrane in order to translocate the RNA genome[76], [82]. A study on HRV-A16 suggests that VP4 is responsible for pore formation and the externalized VP1 is presumably involved in making the pores larger, which increases membrane permeability for RNA translocation[70].

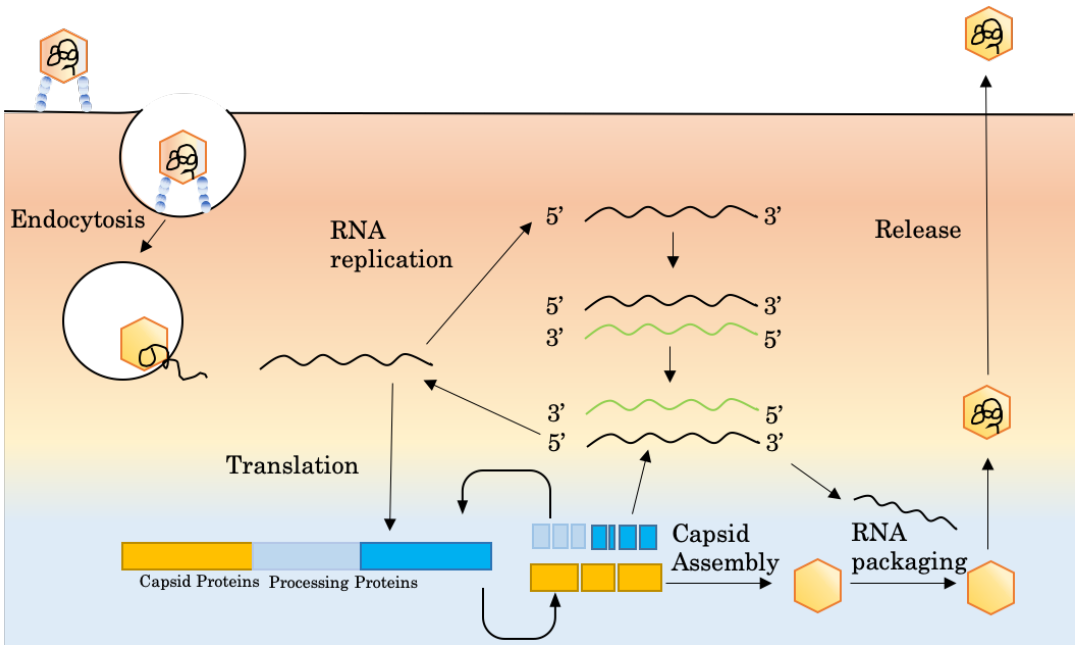


**Fig. 1.6. Schematic representation of the EV life cycle.** An EV virion attaches to the host cell surface and binds to receptors for entry. Receptor binding and endosomal low pH trigger the uncoating process. With these conformational changes, the native mature virion transforms to an A-particle and deposits the RNA genome into the cytosol, which is later translated into structural proteins and non-structural processing proteins that are essential in capsid formation and RNA replication. When a new capsid is formed and packed with an RNA molecule, virion maturation is induced. Newly produced viruses are released from the host cell through lytic and non-lytic pathways. This figure is made based on the following references: [76].

### 1.3.2 Replication

As soon as an EV is uncoated and the genetic material is released into the cytosol, VPg is cleaved[130]. A ribosome binds to IRES, followed by scanning of the initiation codon, which is located 50-100 nucleotides after the 3' end of the IRES [14]. Protein synthesis proceeds based on the translation of the ORF. However, the polyprotein does not accumulate during cell infection because it is cleaved into capsid proteins VP0, VP1 and VP3 and a set of non-structural processing proteins once the coding regions of the viral proteases 2A, 3C and 3CD are translated (**Fig.1.4**). Another product of polyprotein cleavage is the RNA polymerase 3D, which further synthesizes a negative-stranded RNA based on the original positive-stranded RNA. The negative-stranded RNA plays a role as a template for synthesizing more positive-stranded RNAs, which provides either the resources to make more RNA molecules or the genetic material needed for the assembly of new virus particles[14], [76]. The packaging of RNA into the capsid induces an autocatalytic

mechanism that cleaves VP0 into VP4 and VP2, resulting in the mature EV virion[76], [131]. It is believed that the mature EV virions, in order to be released, induce cell death and lyse the host cells via apoptosis[132]–[134]. However, many recent studies have found that EVs are able to exit host cells through vesicles, which enhances the infection yield[76], [132], [133], [135].

### 1.4 Prevention and control

Fortunately, PV vaccines have been developed and PV infections have been reduced dramatically. However, for non-polio EVs, which also cause severe human diseases, there are no vaccines to protect against infections[6]. However, major progress has been made on a vaccine for EV-A71, the causative agent in hand, foot and mouth disease[6], [13]. The EV-A71 viral-like particles, generated for vaccine purposes, showed strong immune responses *in vitro* and efficient protection *in vivo*[136], [137]. Using VP1 as a neutralizing antigen has also been attempted by many researchers, and the successful immune responses in both cell and animal experiments have revealed the strong potentials of developing recombinant VP1 vaccines[138], [139]. However, many factors such as the high cost of vaccine development and unwanted immune responses, have brought limitations and challenges in vaccine design and optimization[140].

There are also no approved drugs against EV infections. However, potential antiviral candidates have been developed[6], [141] such as WIN compounds[102]. These compounds interfere with the life cycle of many EVs (for example, PV-1 and HRV-B14) at the entry step by replacing the pocket factors. This either simply stabilizes the capsid and prevents the uncoating process or causes large conformational changes on the canyon floor which further inhibits receptor binding[1], [6]. Pleconaril, another pocket binding compound, has a broad efficiency against 90% of HRVs[107] and 215 clinical EV strains including different coxsackieviruses and echoviruses[108]. A structural study of EV-D68 also showed that pleconaril is able to replace the pocket factor to inhibit viral infection[2]. Many therapeutic designs, especially in the field of EV-A71, have used pleconaril as a template[142]. Other than pleconaril, additional capsid binding inhibitors, such as vapendavir[106] and pocapavir[143], have been developed and found to be efficient in inhibiting the entry process of many HRVs and PVs as well as some other EVs[109], [144]. However, overall side effects and drug resistance resulting from virus mutations have brought challenges in developing therapeutic strategies against EV infections[6], [145].

# 2. CRYO-ELECTRON MICROSCOPIC STRUCTURES OF HUMAN ENTEROVIRUS D68 IN COMPLEX WITH HUMAN MONOCLONAL ANTIBODIES

Most of the content of this chapter has been published in *Science Immunology*: [146].

## 2.1 Abstract

Human enterovirus 68 (EV-D68) is an important human pathogen within the Enterovirus genus that causes respiratory illness in children and severe infections can lead to neurological disorders. Recently, a rising incidence of infections and outbreaks suggest that EV-D68 has emerged as a public threat globally. However, to date, there are no specific vaccines to prevent EV-D68 infections. Antibodies with potent neutralization abilities are potentially therapeutic agents. Here, we present the cryo-electron microscopy (cryo-EM) structures of EV-D68 in complex with two EV-D68 human monoclonal antibodies, EV68-159 and EV68-228, at a resolution of 2.9 Å and 3.1 Å, respectively. These structures demonstrate that Fab molecules of EV68-159 and EV68-228 bind the EV-D68 viral capsid at two distinctive loci around the three-fold and five-fold axes, respectively. The neutralization of EV-D68 is likely achieved by blocking viral entry through two different pathways. Furthermore, the structures also revealed the amino acids involved in binding which presumably play important roles in controlling neuro-invasion.

## 2.2 Introduction

The Enterovirus (EV) genus contains a large number of icosahedral positive sense RNA viruses with a diameter of about 300 Å. Many members within this genus infect humans and cause diseases with various symptoms from mild to severe. The most noted member is poliovirus, the causative agent of poliomyelitis[6], [14]. However, starting from the 21$^{st}$ century, Enterovirus D68 (EV-D68), a childhood respiratory disease-causing agent that is also capable of causing polio-like acute flaccid myelitis (AFM), has been described as the "new polio". Especially since the year of 2014, noticeable numbers of AFM outbreaks have been reported across the globe, which suggests that EV-D68 is a serious human pathogen that should not be overlooked[16], [147]. However, there is are no vaccines or drugs against EV-D68 infections thus far.

Like other EVs, the capsid structure of EV-D68 is consist of 60 copies of viral protein (VP) 1, VP2, VP3 and VP4, following an icosahedral pseudo T=3 symmetry[2]. The smallest protein, VP4, forms a network on the interior wall of the capsid and interact with the RNA, whereas the three larger proteins, VP1-3, each having a typical jelly roll fold pattern, form the capsid surface[2], [23], [93]. A deep surface depression around each five-fold axis, called the "canyon", is the receptor binding site during viral entry[1], [23]. A glycan receptor, sialic acid, has been found to bind to the canyon of EV-D68 and causing conformational changes including the expulsion of the pocket factor which regulates capsid stability[119]. In addition, capsid stability is also influenced by the N-termini as well as some specific β-strands of the VPs[67].

Several surface loops on VP1-3 close to the canyon, called neutralizing immunogens (NIms) and numbered as NIm-I, II, III, respectively, have significant roles in antibody binding[23], [86]. A recent structural study between EV-D68 and two murine monoclonal antibodies (mAbs) shows that some of these classical immunogenic sites are recognized by and interact with these mAbs. The bindings of the two mAbs occur at two loci, one around the three-fold axes and the other around five-fold axes[148]. However, it is essential to further study human mAbs against EV-D68, since identifying additional or confirming already described epitopes recognized by human mAbs will be important for vaccine and drug design against EV-D68.

We have obtained two human mAbs, EV68-159 and EV68-228 from the laboratory of Dr. James. E Crowe, Vanderbilt. Here, we describe two structures, EV-D68:Fab EV68-159 and EV-D68:Fab EV68-228 of these complexes, at a resolution of 2.9 Å and 3.1 Å, respectively. The Fab molecules EV68-159 and EV68-228 bind around the three-fold axes and the five-fold axes, at unique epitopes compared to the previous complexes of EV-D68 and murine mAbs[148]. These structures show at atomic level the similarities and distinctions between the EV68-159 and EV68-228 neutralization mechanisms and reveal essential amino acids which could be the targets for future therapeutic developments.

## 2.3 Materials and methods

### 2.3.1 Cell lines and viruses

Human Rhabdomyosarcoma (RD, CCL-136, American Type Culture Collection) cells were cultured in the medium containing Dulbecco's Modified Eagle Medium (DMEM, Sigma-Aldrich), 10% heat inactivated fetal bovine serum (HI-FBS, Sigma-Aldrich) together with 1X nonessential amino acids (NEAA, Life Technologies). The EV-D68 US/MO/14-18947 strain (EV-D68 MO strain) (GenBank accession no. AIS73051.1) was obtained from BEI Resources, National Institute of Allergy and Infectious Diseases, National Institute of Health. Viruses were passaged in RD cells and stored at -80 ℃ before large scale propagation.

### 2.3.2 Virus purification

RD cells were grown to 80% confluency and were infected with EV-D68 at a multiplicity of infection of 0.01. Two days post infection, the cells were collected together with the supernatant and spun down. The cell pellets were collected and after multiple freeze/thaw cycles spun down to remove cell debris. All supernatants were combined and pelleted at 210,000 x *g* for 2 hours. The pellets were incubated and resuspended in 250 mM HEPES (pH=7.5), 250 mM NaCl buffer, then supplemented with final concentration 5 mM $MgCl_2$, 0.01 mg/mL deoxyribonuclease (DNase) (Sigma-Aldrich), 0.8 mg/mL trypsin, 15 mM EDTA and 1% (w/v) n-lauryl-sarcosine. The sample was then pelleted at 210,000 x *g* for 2 hours, resuspended, and loaded onto a potassium tartrate gradient (10 to 40%, w/v) for the last round of ultracentrifugation at 160,000 x *g* for 2 hours. The purified virus sample, which was observed as a blue band in the middle of the tube, was extracted and buffered exchanged into 20mM Tris, 120mM NaCl, 1mM EDTA (pH=8.0) buffer to remove potassium tartrate.

### 2.3.3 Fab fragment purification

The two mAbs, EV68-159 and EV68-228, were provided by the laboratory of Dr. James Crowe, Vanderbilt University. The Fab fragments were generated and purified with a Pierce Fab Preparation Kit (Thermo Fisher Scientific). The Immobilized Papain vial spin column and Zeba Spin Desalting Column were equilibrated with digestion buffer (35 mg cysteine·HCl per 10mL of supplied Fab Digestion Buffer, pH~7.0) before use. The NAb Protein A Plus Spin Column was

equilibrated with PBS buffer before use. The original IgG samples were prepared through Zeba Spin Desalting Column, and 0.5mL of the prepared IGg samples were applied on the Immobilized Papain vial and incubated at 37 ℃ for 5 hours fab digestion. The digested samples were then added to NAb Protein A Plus Spin Column, and the fab fragments were purified with IgG Elution Buffer. The final Fab fragments were buffer exchanged to PBS and stored at 4 ℃.

### 2.3.4 Cryo-EM

For both EV-D68:Fab EV68-159 and EV-D68:Fab EV68-228 complexes, purified EV-D68 viruses and Fabs were mixed at a molar ratio of 1:200. After incubation at room temperature for 45 to 60 minutes, 3.5 μL of virus-Fab mixture sample were added to a glow-discharged 400 mesh lacey carbon film copper grid (Ted Pella Inc.). Grids were plunge frozen (Cryoplunge 3 system, Gatan) in liquid ethane after being blotted for 3.5 seconds in 75 to 80% humidity. Cryo-EM datasets were collected on a 300 kV Titan Krios Microscope (Thermo Fisher Scientific). The EV-D68:Fab EV68-159 dataset was acquired with a K2 Summit direct electron detector (Gatan) at a nominal magnification of 81,000X, resulting in a super resolution pixel size of 0.874 Å, with a defocus range from 0.7 to 3.5 μm. A total electron dose of 31.4 electrons/Å$^2$ over 12 seconds of exposure was split into 60 frames. For the EV-D68:Fab EV68-228 dataset, movies were collected using the program Leginon[149] with a K3 Direct Detection Camera (Gatan) at a magnification of 64,000X, resulting in a super resolution pixel size of 0.662 Å, with a defocus range from 0.7 to 2 μm. A total electron dose of 44.2 electrons/Å$^2$ over 2.6 seconds of exposure was recorded over 50 frames. Overall, 732 movies and 462 movies were acquired for the EV-D68:Fab EV68-159 and EV-D68:Fab EV68-228 datasets, respectively.

### 2.3.5 Image processing, model building and refinement

For both datasets, motion correction was performed on the raw movie frames with MotionCor2[150] as implemented in Appion[151] during data collection. The contrast transfer function (CTF) was estimated on the aligned frames with CTFFIND4[152]. Particle picking templates were generated using the Appion Manual Picker[151] and templates for auto picking were obtained through two-dimensional (2D) classification in XMIPP[153]. These templates were then used for auto-picking in FindEM[154] and particles were extracted using RELION[155].

These particles were then subjected to multiple rounds of 2D and 3D classifications in RELION[155]. This resulted in 20,194 and 30,554 particles for the EV-D68:Fab EV68-228 and EV-D68:Fab EV68-159 datasets which were selected for final 3D icosahedral reconstructions using the program JSPR following the gold-standard refinement method[156]. The final resolutions for both maps were estimated based on a gold-standard Fourier shell correlation cutoff of 0.143[157]. Map sharpening was done in RELION[155] post-processing. Data collection parameters and related items are summarized in **Table 2.1**.

The same methods were used for the atomic structures of both EV-D68:Fab EV68-159 and EV-D68:Fab EV68-228. The X-ray crystallography model of the EV-D68 Fermon strain (PDB: 4WM8) was selected as a starting reference for model building and was manually fitted into the density maps using the program Chimera[100]. Using the initial fitting as a basis, the models were rebuilt in Coot[158] and refined using real-space-refinement in PHENIX[159] to correct for outliers and poorly fitted rotamers. Chimera[100], Coot[158] and CCP4i2-PISA[160] were used to determine the binding interface residues. The final atomic models were validated in MolProbity[161]. Refinement statistics are described in **Table 2.1**.

### 2.3.6 Data availability

The coordinates and maps of EV-D68:Fab EV68-159 and EV-D68:Fab EV68-228 have been deposited in Protein Data Bank (accession codes: 6WDS, 6WDT, respectively) and Electron Microscopy Data Bank (accession codes: EMD-21647, EMD-21648, respectively).

## 2.4 Results

### 2.4.1 Structural features of the immune complexes

Two potent neutralizing human mAbs, EV68-159 and EV68-228, were used to generate immune complexes with the EV-D68 strain (US/MO/14-18947) for cryo-EM studies. The final density maps attained a resolution of 2.9Å and 3.1Å, respectively **(Fig. 2.1, Fig. 2.2, Fig. 2.3 and Table. 2.1)**. The structures reveal two distinct binding sites: EV68-159 binds around the three-fold axes, whereas EV68-228 binds around the five-fold axes between depressions that form the canyon regions **(Fig. 2.1, Fig. 2.4)**. Thus, for each Fab, a total of 60 copies bind to the virus particle. The

Fab variable domains, which interact with the viral surface, display strong densities similar to the viral capsid proteins, and an atomic model of each Fab was built together with the four viral capsid proteins. In contrast, the Fab constant domains, which are located further from the viral surface, display weaker and comparatively broken densities, and were excluded from atomic model building. The backbone of the polypeptide chains and the majority of amino acid side chains are well-ordered in the density maps, demonstrating the critical features of the binding interfaces between virus particle and Fab molecule. For both models, the viral surface residues that were facing and within a 4Å distance from the Fab were identified as the footprint **(Fig. 2.1C, Fig. 2.5 and Table. 2.2)**. The footprints show that both Fab molecules are located within one protomer.

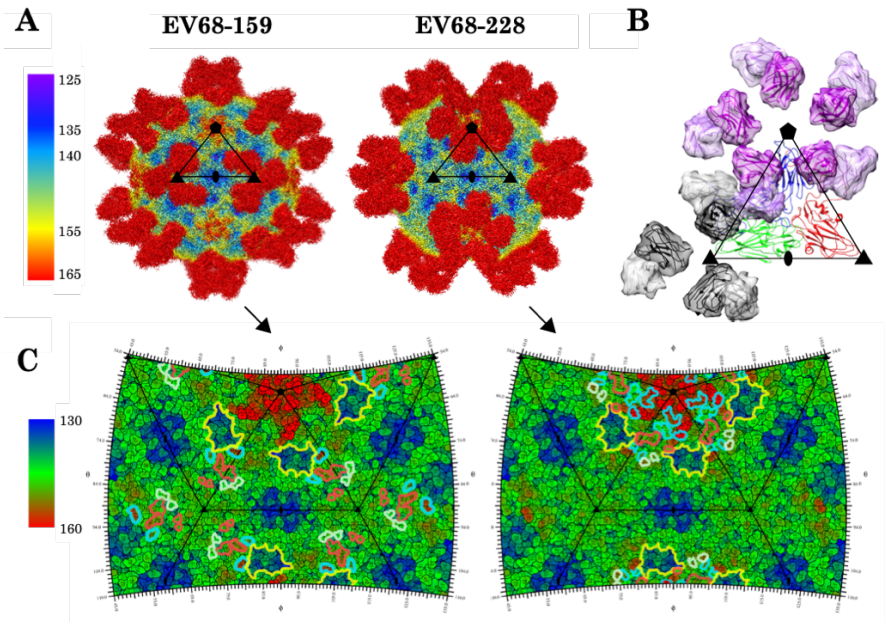


**Fig. 2.1. Structural feature comparison between two immune complexes.** (**A**) Radially colored cryo-EM maps of EV-D68:Fab EV68-159 (left) or EV-D68:Fab EV68-228 (right). Each map is projected down a two-fold axis of symmetry. The five-, three-, and two-fold axes of each asymmetric unit are depicted using a triangle labeled with one pentagon, two small triangles, and one oval, respectively. (**B**) Binding position comparison on an asymmetric unit. Viral proteins are colored in blue (VP1), green (VP2) and red (VP3). Fab molecules are colored in grey (EV68-159) or purple (EV68-228), and the heavy or light chains are shown in the same colors with dark or light intensities, respectively. (**C**) Footprints of EV68-159 Fab (left) or EV68-228 Fab (right). Radially colored 2D projections of the viral surface were created with RIVEM. Virus surface residues facing any atoms from the Fab molecules within a distance of 4 Å are outlined in light blue (VP1), light green (VP2) and light red (VP3). The canyon region is outlined in yellow. Scale bars in (**A**) and (**C**) indicate radial distance measured in Å.

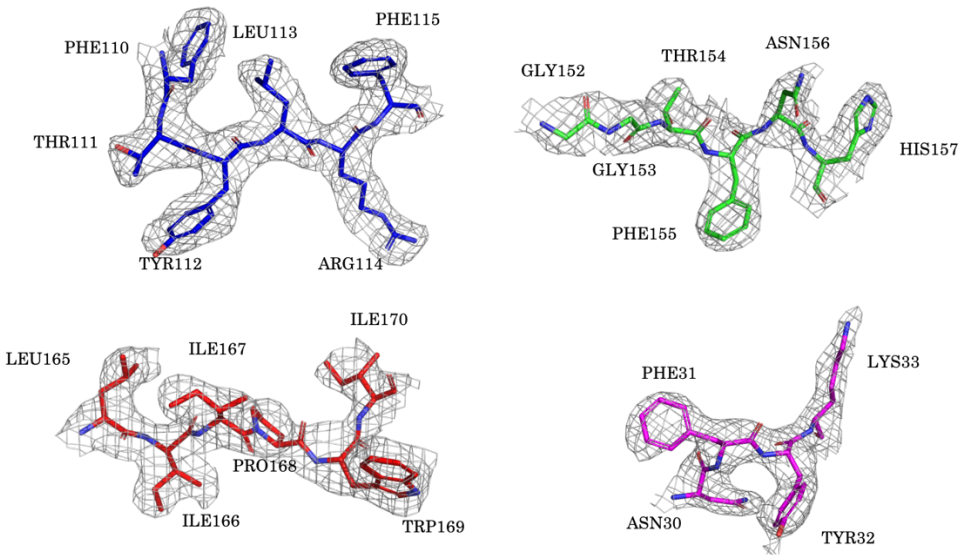


**Fig. 2.2. Representative densities from the EV-D68: Fab EV68-228 electron density map.** Viral proteins are colored in blue (VP1), green (VP2), red (VP3) and magenta (VP4).

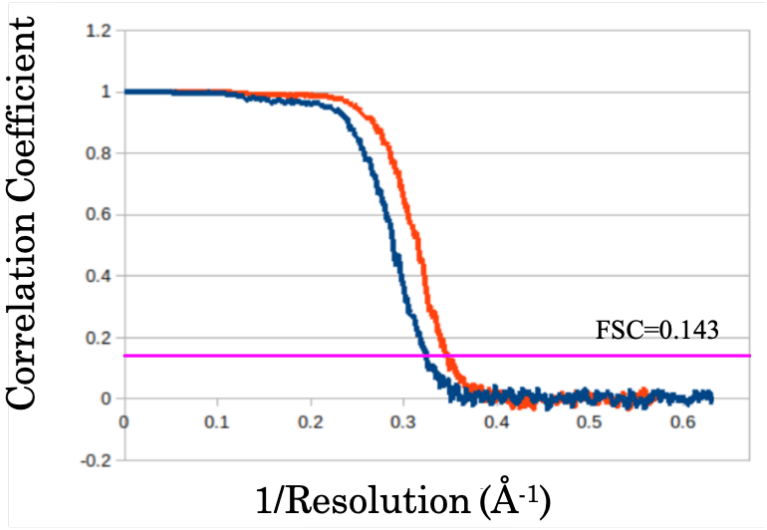


**Fig. 2.3. Estimates of immune complex map resolutions.** Map resolutions are estimated based on the gold-standard Fourier shell correlation (FSC) cutoff of 0.143. The final resolutions for EV68-159 (red curve) or EV68-228 (blue curve) complexes are 2.9 Å or 3.1 Å, respectively.

**Table 2.1. Cryo-EM data acquisition parameters and refinement statistics.**

| | **EV-D68:Fab EV68-159** | **EV-D68:Fab EV68-228** |
|---|---|---|
| Magnification | 81,000X | 64,000X |
| Camera | K2 Summit direct electron detector (Gatan) | K3 Direct Detection Camera (Gatan) |
| Voltage (kV) | 300 | 300 |
| Pixel size (Å) | 0.874 | 0.662 |
| Defocus range (μm) | 0.7-3.5 | 0.7-2.0 |
| Total electron dose (electrons/Å2) | 31.4 | 44.2 |
| Particles picked | 42,078 | 27,390 |
| Particles used | 30,554 | 20,194 |
| Map resolution (FSC threshold =0.143) | 2.9 | 3.1 |
| **Model building and refinement** | | |
| Model building reference (PDB code) | 4WM8 | 4WM8 |
| MolProbity score | 1.93 | 1.96 |
| Clash score | 9.05 | 8.7 |
| Rotamer outliers (%) | 0.46 | 0.00 |
| r.m.s.d | | |
| Bond length (Å) | 0.005 | 0.005 |
| Bond angles (°) | 0.691 | 0.689 |
| Ramachandran plot (%) | | |
| Favored | 93.08 | 91.70 |
| Allowed | 6.92 | 8.20 |
| Outliers | 0.00 | 0.10 |

**Table 2.2. Structural contact amino acid residues of EV-D68 and respective Fabs.** Heavy and light chains are labeled as H and L, respectively. Notably, only direct interactions that are clearly observed in the electron density maps at high resolution are listed. This differs from contact residues highlighted in the roadmaps (Fig. 2.1C, Fig. 2.5), which use a 4Å cutoff for displaying the overall footprint at maximum hydrogen bonding distance.

| Viral amino acid | Fab amino acid | Potential interaction |
|---|---|---|
| **EV68-159** | | |
| VP1: GLU271 | L: ILE95 | Hydrogen bond |
| VP1: ARG272 | L: SER26 | Hydrogen bond |
| | L: SER27 | Hydrogen bond |
| | L: ASP94 | Salt bridge |
| VP1: ASP285 | L: LYS51 | Salt bridge |
| VP3: GLU59 | H: ARG102 | Hydrogen bond |
| VP3: SER60 | H: GLY100 | Hydrogen bond |
| VP3: MET64 | H: TYR56 | Hydrogen bond |
| VP3: GLU65 | H: SER51 | Hydrogen bond |
| | H: THR52 | Hydrogen bond |
| | H: SER53 | Hydrogen bond |
| **EV68-228** | | |
| VP1: LYS71 | H: SER30 | Hydrogen bond |
| VP1: ARG72 | H: TYR27 | Hydrogen bond |
| VP1: SER73 | H: ASN31 | Hydrogen bond |
| VP1: GLY129 | H: SER73 | Hydrogen bond |
| VP1: LYS268 | L: ASP92 | Salt bridge |
| VP2: ASN136 | L: SER30 | Hydrogen bond |
| VP3: GLY 234 | H: ASN102 | Hydrogen bond |
| VP3: LEU236 | H: ASN102 | Hydrogen bond |
| VP3: ASP237 | H: TYR34 | Hydrogen bond |
| | H: SER100 | Hydrogen bond |
| | H: CYS101 | Hydrogen bond |
| | H: ASN102 | Hydrogen bond |
| VP3: HIS238 | H: TYR53 | Hydrogen bond |
| | H: TYR54 | Hydrogen bond |
| VP3: GLU243 | H: TYR33 | Hydrogen bond |

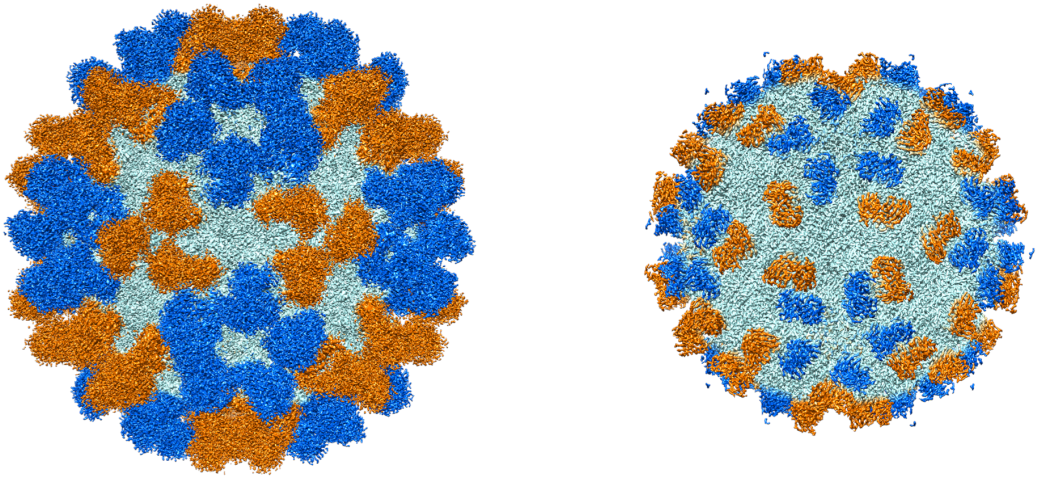

**Fig. 2.4. Comparison of the Fab binding sites.** EV68-159 and EV68-228 are colored in gold and blue, respectively, and the viral surface is colored in cyan. The left panel shows both variable domains and constant domains, whereas the right panel shows only the variable domains, demonstrating that the footprints of the two Fabs do not overlap.

### 2.4.2 EV-D68:Fab EV68-159 complex reveals new epitopes

In the EV-D68:Fab EV68-159 complex, each Fab masks a viral surface area around 990Å$^2$. The heavy chain of EV68-159 contributes approximately 77% of the masked surface areas. At the binding interface **(Fig. 2.6, Table. 2.2)**, essential interactions are found between the EV68-159 light chain and three residues on the C-terminus of VP1: Glu271 and Arg272 **(Fig. 2.7A)** and Asp285 **(Fig. 2.7B)**. Residues Glu271 and Arg272 form hydrogen bonds with complementarity-determining region (CDR)3 and CDR1 and Arg272 and Asp285 form salt bridges with CDR3 and CDR2 residues, respectively. A series of hydrogen bonds was found between the heavy chain CDR2 and CDR3 and the VP3 N-terminal loop before the B-β strand (βB) **(Fig. 2.6, Fig. 2.7C)**. In general, the epitope that EV68-159 Fab binds is distinct from the classical NIm sites and the previously reported ones in the EV-D68 murine mAb studies.

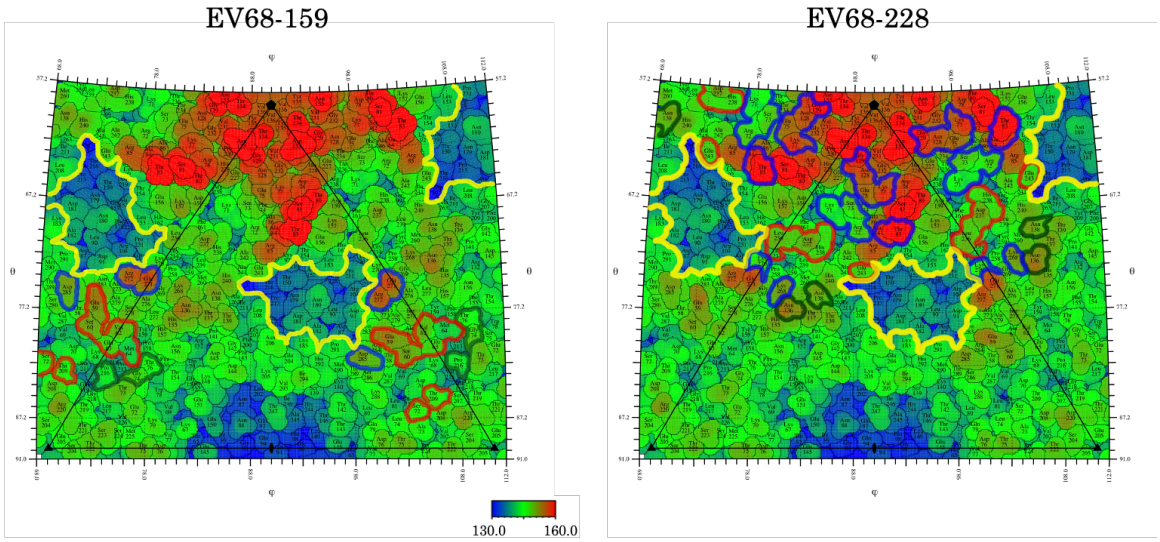


**Fig. 2.5. Roadmaps showing an enlarged view of the Fab footprints.** The radially colored 2D projection of the viral surface was created with RIVEM. Virus surface residues facing any atoms from the Fab molecules within a distance of 4 Å are outlined in light blue (VP1), light green (VP2) and light red (VP3). The canyon region is outlined in yellow.

### 2.4.3 EV68-228 neutralizes EV-D68 through another mechanism

In the EV-D68:Fab EV68-228 complex, each Fab masks approximately 1,170Å$^2$ of the viral capsid surface. Similar to EV68-159, the heavy chain of the EV68-228 Fab dominates the interaction with the viral capsid by masking around 84% of the surface area. The binding interface **(Fig. 2.6, Table. 2.2)** is stabilized mainly by hydrogen bonds formed between the heavy chain CDRs and the VP1 βB as well as the VP3 C-terminus **(Fig. 2.7D)**. Hydrogen bonds are also found between the heavy chain framework region 3 and the VP1 DE loop, which corresponds to the classical picornavirus immunogenic site NIm-IB, and between the light chain CDR1 and the VP2 EF loop, which corresponds to NIm-II. Furthermore, a salt bridge is observed between light chain CDR3 and the Lys268 in the VP1 C-terminus.

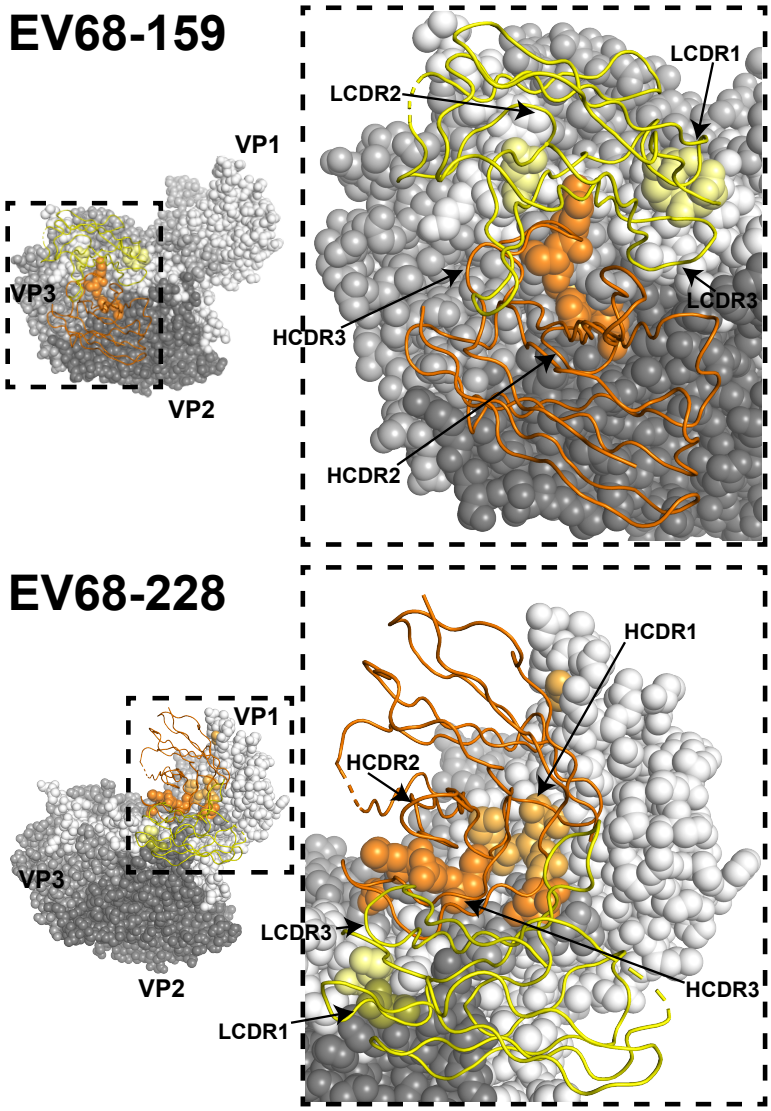


**Fig. 2.6. Close-up view of the binding interfaces of EV68-159 and EV68-228.** The viral capsid is shown as surface and the Fab is shown in a cartoon representation. VP1, VP2 and VP3 are colored in white, dark grey and silver, respectively. Heavy or light chains are colored in orange or yellow, respectively. Viral residues making interactions are colored based on the heavy and light chains, and the color intensities vary based on which of the VPs is involved in the contact. The heavy and light chain complementarity-determining regions (HCDR and LCDR, respectively) involved in the binding interfaces are shown with arrows.

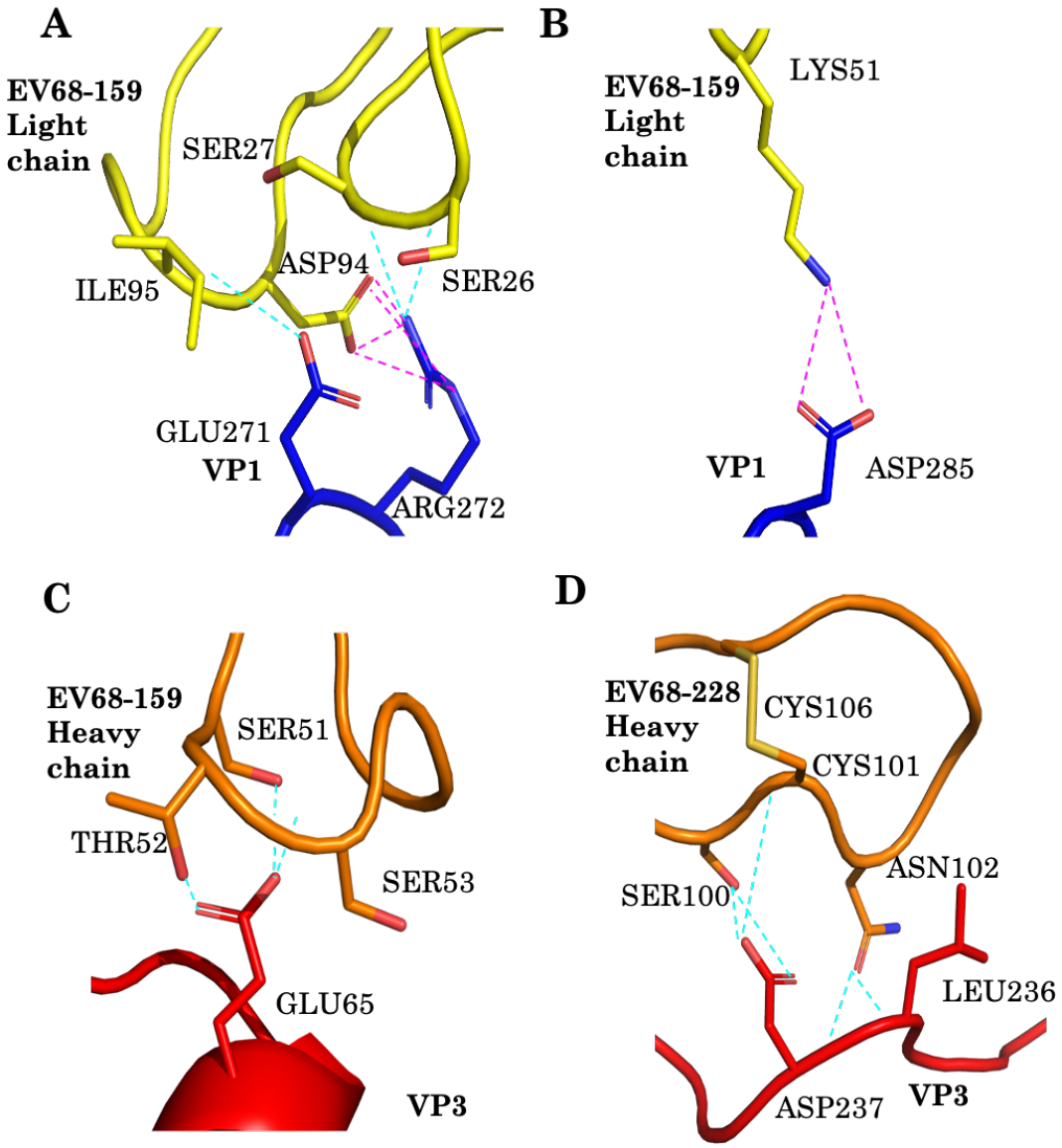


**Fig. 2.7. Detailed view of virion-Fab interactions. (A)** Representative interactions at the binding interface of EV-D68:Fab EV68-159 **(A, B and C)** and EV-D68:Fab EV68-228 **(D).** Hydrogen bonds are colored in cyan and salt bridges are colored in magenta.

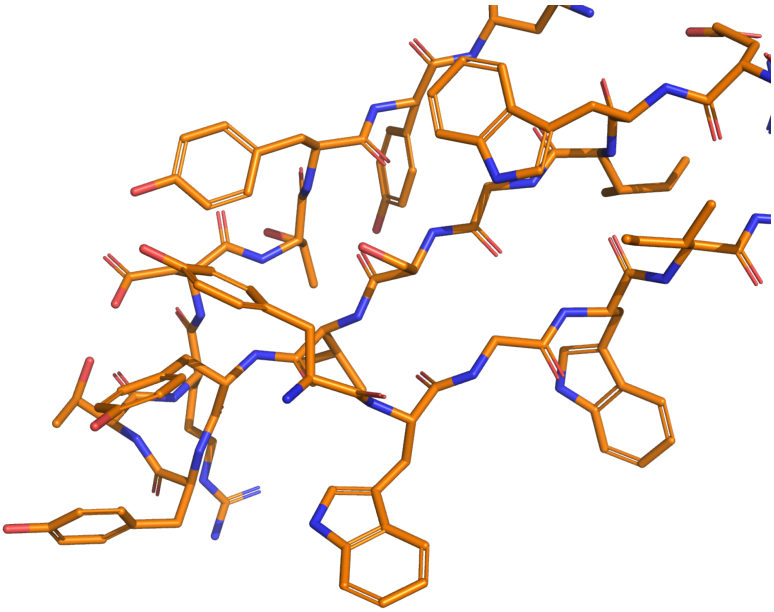

**Fig. 2.8. Bulky side chains of the EV68-228 Fab heavy chain.** This view shows an example of bulky side chains forming a hydrophobic interaction network to stabilize the EV68-228 Fab, which also is seen in the structure of the EV68-159 Fab.

### 2.4.4 A cysteine on EV68-228 heavy chain plays special roles in the immune complex

Bulky side chains are frequently observed at the interface for both Fabs and act to stabilize the structures through aromatic interaction networks **(Fig. 2.8)**. Furthermore, disulfide bonds are also detected between CDR1 and CDR3 in heavy and light chains. Another pair of cysteines, Cys101 and Cys106, are found within the CDR3 of the EV68-228 heavy chain and may form a disulfide bond since they are at the correct distance and orientation **(Fig. 2.7D)**. Specifically, when the contour levels are reduced, the densities of the two cysteine side chains are connected. As described above for the EV-D68: Fab EV68-228 complex, hydrogen bonds are formed between the heavy chain CDR3 and the VP3 C-terminal residues adjacent to the canyon involving Cys101, forming both a hydrogen bond and a disulfide bond **(Fig. 2.7D, Table. 2.2)**. These cysteine residues play critical roles in stabilizing both Fab structure and the virus-Fab binding interface.

## 2.5 Discussion

The EV68-159 Fab binds around the three-fold axes **(Fig. 2.1, Fig. 2.4)** and neutralizes EV-D68 by interacting through a unique immunogenic site. The heavy chain interacts with the VP3

N-terminal loop, which likely prevents the virus from uncoating, since the N-termini of the four VPs contribute to capsid stability[67]. The light chain, on the other hand, interacts extensively with three VP1 C-terminal residues neighboring the canyon, Glu271, Arg272 and Asp285 **(Fig. 2.7A, Table. 2.2)**. These three residues, as well as Glu59 on the N-terminal loop of VP3, are adjacent to the sialic acid receptor binding site[119], suggesting that the EV68-159 Fab blocks virus from binding to its receptor(s). In particular, these three VP1 residues are located on the EV-D68-specific immunoreactive peptide, which is a 22-amino acid long VP1 C-terminal peptide that is associated with AFM[35]. By blocking this specific position, the EV68-159 Fab is potentially able to prevent neuro-invasion of EV-D68 in patients, which is especially significant for future vaccine design.

The EV68-228 Fab binds around the five-fold axes **(Fig. 2.1, Fig. 2.4)** and recognizes a few classical NIms[23], [86]. Other than that, each Fab may also prevent the virus from uncoating by binding part of the VP1 βB, inhibiting externalization of the N-terminus of VP1, which is required for entry. In addition, the Fab footprint includes residues on the C-terminus of VP3 **(Fig. 2.7D)**, which are not part of a classical NIm, especially residues Gly234, Leu236 and Glu243 **(Table. 2.2)**. These three residues are adjacent to the canyon[2] receptor binding site **(Fig. 2.1C, Fig. 2.5)**, suggesting that EV68-228 could block the virus from binding to receptors. Furthermore, Lys268 is two residues away from the recently found VP1 C-terminal immunoreactive peptide described above, showing the potential of this Fab to prevent neuro-invasion as well.

The potential disulfide bond in the CDR3 of EV68-228 heavy chain is a structural moiety that has now been observed in broadly neutralizing antiviral human mAbs for a number of viruses, including both hepatitis C virus[162] and influenza A virus[163]. The intervening 4 amino acids between cysteines form a smaller structured loop at the most distal tip of the full CDR3 loop, stabilizing the CDR3 in a preconfigured state optimal for binding the viral antigen. For EV68-228, specifically, the Cys101 is also able to interact with VP3 via a hydrogen bond besides making a partially occupied disulfide bond with Cys106 **(Fig. 2.7D)**, participating in both CDR3 loop stabilization and interaction with antigen.

Generally speaking, the structures of the immune complexes reveal details of the specific interactions between EV-D68 and the Fab molecules and the neutralization mechanisms, which could bring strong impact in developing therapeutic strategies against EV-D68 and other related EVs.

# 3. STRUCTURAL BASIS OF HUMAN ENTEROVIRUS D94 REPRESENTING DIFFERENT STAGES DURING VIRAL ENTRY

The content of this chapter includes text and data of a manuscript in preparation.

## 3.1 Abstract

Human enterovirus D94 (EV-D94) has been found in association with acute flaccid paralysis, a polio-like central nervous system complication, and potentially diabetes. In addition, high prevalence of this virus is found among Finnish population. Here we present the cryo-EM structures of full native EV-D94 virions, an EV-D94 uncoating intermediate and empty viral particles of EV-D94 at 2.9 Å, 2.6 Å and 2.9 Å resolution, respectively. The structural features, including the shape and orientation of surface loops, canyon and pocket factor, reveal the details of immunogens, receptor usage and viral stability in EV-D94. Moreover, comparisons of these three EV-D94 structures shed light on the enterovirus uncoating process. These results can serve as a starting point for vaccine or anti-viral drug development to prevent or treat infections caused by EV-D94 and related enteroviruses.

## 3.2 Introduction

Picornaviruses, a family of small, non-enveloped RNA viruses with an approximately 30 nm diameter capsid, are associated with many animal and human diseases[14]. An important genus in this family, Enterovirus (EV), contains a range of human pathogens [e.g., EVs, human rhinoviruses (HRVs) and polioviruses (PVs)] which are responsible for health issues in millions of people globally every year[12], [14], [164]; with symptoms ranging from mild respiratory illness[20], [165] to severe neurological infections[19], [39], [166]. Human Enterovirus D94 (EV-D94) is a relatively new serotype, which has been identified from sewage and an acute flaccid paralysis case[167], [168]. In addition, EV-D94 has been suggested as a diabetogenic enterovirus due to its ability to infect pancreatic islet β-cells[22]. As a potentially serious human health threat, EV-D94 may be more severe than has been assumed previously. However, the molecular mechanisms of EV-D94 infection are still poorly understood.

An EV capsid contains 60 identical protomers, each consisting of 4 unique structural proteins: VP1, VP2, VP3 and VP4. VP1, VP2 and VP3, each contain a classical jelly roll fold motif and form the external capsid shell with an icosahedral pseudo T=3 symmetry. VP4 lines the internal surface of the capsid as well as the N-termini of the other 3 structural proteins[14], [23], [24]. All of the N-termini, together with the β-strands of VP1, VP2 and VP3, maintain the capsid stability[67]. Different insertions on the β-strands decorate the exterior of the capsid. Hypervariable loops of the insertions have been shown to be the neutralizing immunogen sites (NIms) and are labeled as NIm-I, NIm-II and NIm-III according to their association with VP1, VP2 and VP3, respectively[23], [86]. At each of the five-fold axes, a deep depression on the viral surface called the "canyon" surrounds a "plateau", a higher altitude region above the mean viral surface. The canyon is usually used as a site for binding the host cell receptor. The "north rim" is formed by VP1, whereas the "south rim" is composed of multiple copies the VP1 N-terminus, the VP1 GH loop, as well as the carboxy (C-) termini of VP2 and VP3. The GH loop of VP1 also forms the canyon floor[1], [14], [23], [24], [84], [127]. The hydrophobic pocket underneath the canyon floor is a feature common to many EVs. The pocket frequently contains a small, non-protein molecule called the "pocket factor", which is believed to be a fatty acid molecule contributing to capsid stability as well as playing an important role during the infection process[1], [82], [93], [169]–[171].

The initial step of EV infection is the binding between virus and receptor, which previous studies have shown to involve binding to Immunoglobulin (Ig)-like receptors or carbohydrate receptors like sialic acid. This in turn destabilizes the EV capsid and expels the "pocket factor". However, only the Ig-like receptors, but not sialic acid, are able to trigger uncoating and the formation of the altered- (A-) particle [1], [119]. An A-particle is considered an intermediate state of an EV virion that is characterized by open channels at the two-fold axes, a 4% expanded capsid size, externalized N-termini of VP1 and loss of VP4[14], [82], [124], [125], with reduced infectivity and less stable[82], [97], [172]. The formation of the A-particle is essential for the release of the viral genome into the host cell cytoplasm[70], [76], [82], [97].

EV-D94 belongs to the EV-D species and shares high sequence identity (~85%) with its closest relative EV-D68, a human pathogen that mainly causes common cold symptoms among

children but sometimes leads to neurological issues[35], [147], [173]–[176]. It has been reported that both EV-D94 and EV-D68 use sialic acid as a carbohydrate receptor. However, EV-D94 has a broader tissue tropism[22], suggesting that EV-D94 recognizes distinct proteinaceous receptors or even uses different infection pathways.

Here, we describe the cryo-electron microscopy (cryo-EM) structures of 3 different states of EV-D94: full mature particles (2.9 Å), A-particles (2.6 Å) and empty particles (2.9 Å). The structures reported in this study reveal information about general structural features at an atomic level as well as the early stage uncoating process of EV-D94, while providing a platform for the potential development of a vaccine or anti-viral drugs against EV-D94 and related EVs.

## 3.3 Materials and methods

### 3.3.1 Cell lines and viruses

Human Rhabdomyosarcoma (RD, CCL-136, American Type Culture Collection) cells were cultured with Dulbecco's Modified Eagle Medium (DMEM, Sigma-Aldrich) supplemented with 10% heat inactivated fetal bovine serum (HI-FBS, Sigma-Aldrich) and 1X nonessential amino acid (NEAA, Life Technologies). The EV-D94 E210 strain was obtained from the National Institute of Public Health and the Environment in the Netherlands, passaged in RD cells and kept at -80 ℃ for storage.

### 3.3.2 Propagation and purification of EV-D94

To grow viruses for structural studies, RD cells were cultured to 80% confluency and then infected with EV-D94 at 33 °C. A mixture of cells and medium was collected 48 hours post infection when complete cell death was observed and then spun down at 4,500 RPM (JA-10 rotor) for 15 minutes to separate cells and supernatant. The cell pellet was resuspended by pipetting multiple times to break intact cells and release the virus in them. This mixture was then spun down together with the previous supernatant at 9,500 RPM (JA-10 rotor) for 50 minutes and the supernatant was spun down at 48,000 RPM (50.2ti rotor) for 2 hours. The pellets were resuspended and incubated in 250 mM HEPES, 250 mM NaCl (pH 7.5) buffer and then treated with final concentration 5 mM $MgCl_2$, 0.01 mg/mL deoxyribonuclease (DNase) (Sigma-Aldrich), 0.8

mg/mL trypsin (Sigma-Aldrich), 15 mM EDTA and 1% (m/v) n-lauryl-sarcosine. The sample was spun down at 48,000 RPM (50.2ti rotor) for 2 hours with a 30% sucrose cushion. After centrifugation, the pellet was again resuspended and incubated in 250 mM HEPES, 250 mM NaCl (pH 7.5) buffer and applied onto a potassium tartrate gradient (10-40%, w/v) and separated at 36,000 RPM (SW41 rotor) for 2 hours. The lowest and the most dominant band, indicating particles with the highest sedimentation coefficient, was harvested and buffer exchanged against a buffer containing 20 mM Tris, 120 mM NaCl, 1 mM EDTA (pH 8.0).

### 3.3.3 Cryo-EM

For cryo-EM grid preparation, 3.5 µL of purified EV-D94 were applied to a glow-discharged 400 mesh lacey carbon film copper grid (Ted Pella Inc.). At a humidity of 75%, grids were blotted for 4 seconds and plunge frozen (Cryoplunge 3 system, Gatan) in liquid ethane. Samples were imaged on a 300 kV Titan Krios transmission electron microscope (ThermoFisher) equipped with a BioQuantum energy filter and a K2 detector. Movies were acquired using Leginon[149] at a nominal magnification of 81,000x in super resolution mode with a calibrated pixel size of 0.874 Å per pixel. The defocus range was set to 0.7-3.5 µm and a total dose of 27 $e^-/Å^2$ during a 10 seconds exposure was used for each movie split over 50 frames.

### 3.3.4 Image processing

A total of 1390 movies were recorded in one session. Motion between individual frames within one movie was estimated and subsequently corrected using MotionCor2[150] as implemented in the Appion pipeline[151], in parallel with the data collection. CTF estimation on the aligned and averaged frames was done using CTFFIND4[152]. Particles were selected manually from 50 micrographs using the Appion Manual Picker[151] and used to generate templates by 2D classification in XMIPP[153]. Afterwards, 210,926 particles were selected by automated template matching as implemented in FindEM[154]. The particles were extracted and normalized using RELION[155] and sorted and classified using 2D and 3D classification in the same program. The final classification yielded a total of 7,374 full particles, 34,954 empty particles and 165,338 A-particles. The three types of particles were reconstructed using the program JSPR[156] using a gold-standard refinement approach[157]. The resolution of all three EV-D94

structures was estimated using the Fourier shell correlation[177] at a threshold of 0.143. All maps were sharpened before model building using RELION[155].

### 3.3.5 Model building and refinement

The asymmetric units of the three EV-D94 structures, including VP1, VP2, VP3 and VP4, were manually built into the density maps based on the crystal structure of EV-D68 (PDB: 4wm8) using the program COOT[158] and refined using the program Phenix[159]. Multiple rounds of model rebuilding in COOT[158] and real space refinement in Phenix[159] were done to improve the model fitting against the cryo-EM density maps. The final model quality was evaluated based on Molprobity[161].

## 3.4 Results

### 3.4.1 Structure determination

EV-D94 was cultivated in RD cells and purified using ultracentrifugation. The lowest and the most dominant band with the highest sedimentation coefficient was harvested and used for cryo-EM data collection **(Fig. 3.1A)**. A total of 210,926 particles were extracted from 1,389 micrographs and sorted into 7,374 full particles, 34,954 empty particles and 165,338 uncoating intermediate A-particles using two-dimensional (2D) **(Fig. 3.1B)** and 3D classification in RELION[155] **(Fig. 3.1C)**. These classes were subsequently reconstructed and refined using JSPR[156], using a gold-standard approach. The final maps for the full particle, A-particle and empty particle reached resolutions of 2.9 Å, 2.6 Å and 2.9 Å **(Fig. 3.2A)**, respectively, according to the Fourier shell correlation (FSC) at 0.143, allowing accurate fitting of the amino acid backbone and side chains **(Fig. 3.3)**. The atomic models were manually built in COOT[158] and refined using Phenix[159].

### 3.4.2 The atomic model of EV-D94 full particle

The overall structure of EV-D94 is similar to EV-D68 and other viruses of the EV genus. The three large structural proteins, VP1, VP2 and VP3, each have an eight-stranded antiparallel “jelly roll” fold. The surface of the capsid follows pseudo T=3 icosahedral symmetry with VP1 located around the five-fold axes and VP2 and VP3 extending through the two-fold and three-fold axes

**(Fig. 3.2A, B)**. Around the "plateau" region at each of the five-fold axis, EV-D94 has two rings of protruding loops **(Fig. 3.2A, C)**. The VP1 BC loop (the loop that joins β strand B and C) forms the protrusion of the outer ring around the five-fold axis, whereas the VP1 DE loop forms the protrusion of the inner ring near the five-fold vertex. Some residues located in the two loop regions correspond to the NIm-IA and NIm-IB sites that are recognized by neutralizing antibodies to other EVs[23], [86] **(Fig. 3.2C, Fig. 3.4A, B)**. Among typical EV-D species, residues on and close to the NIm sites are the least conserved regions in VP1, with the exception of the NIm-IB residues on the BC loop, which are very conserved **(Fig. 3.5)**. The BC and DE loops in EV-D94 extend further from the viral surface in comparison to other neuro-invasive EVs like EV-D68 and EV-A71 **(Fig. 3.6A, B)**. The densities for the two loop regions, however, are not as good as the densities for the rest of the virus, indicating some amount of flexibility, but remaining sufficiently defined to allow model building **(Fig. 3.4C)**.

### 3.4.3 The "south rim" of the EV-D94 canyon has a different shape

Like other EVs, VP1 of EV-D94 forms the "north rim" of the canyon. The VP1 GH loop contributes to the formation of the canyon floor and the "south rim" of the canyon. The C-termini of VP1 and VP3 as well as the VP2 EF loop complete the "south rim" of the canyon **(Fig. 3.4A)**. The overall shape of the canyon in EV-D94 is similar to EV-D68. However, residues 204-212 on the VP1 GH loop of EV-D94 are extended in comparison to EV-D68, which alters the shape of the "south rim" of the canyon and likely contributes to a different receptor specificity during viral attachment. This extended GH loop region is found in both EV-A71 and PV-1, where EV-A71 has a broader shape and PV-1 has an elongated configuration that is extending away from the viral center **(Fig. 3.6C)**. In addition, the VP2 EF loop that also forms the "south rim" of the canyon is shorter in EV-D94 than what has been described for both EV-A71 and PV-1.

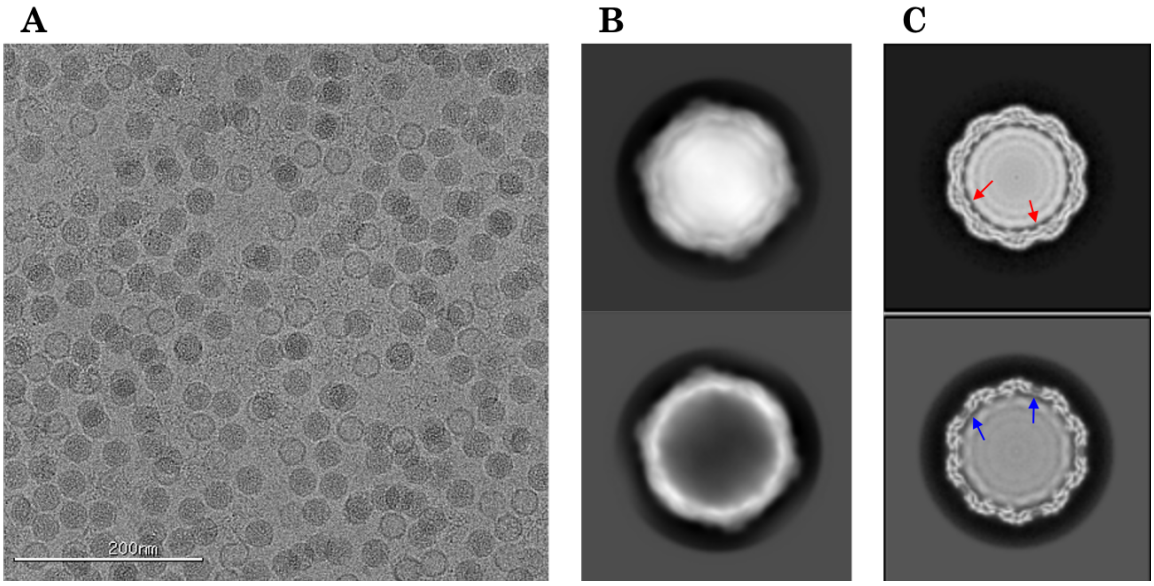


**Fig. 3.1. Cryo-EM of EV-D94. (A)** Cryo-EM image of EV-D94 particles (scale bar = 200nm). **(B)** 2D class averages of the virus. After 2D classification, two types of EV-D94 particles were identified: a "full class" that contains inner density (upper panel; 172712 particles) and an "empty class" that contains no inner density (lower panel; 34954 particles). The inner density corresponds to the genomic material of the virus. **(C)** Cross sections of the 3D classes obtained by refining the full particles obtained from 2D classification show two distinct structural states. The central slice of the full particles (upper panel) shows a filled core and the presence of VP4 indicated with red arrows. The central slice of the A-particles (lower panel) lacks a strong internal density and is missing VP4. The resulting holes on the surface of the capsid and between the capsid proteins and the genomic material are indicated with blue arrows.

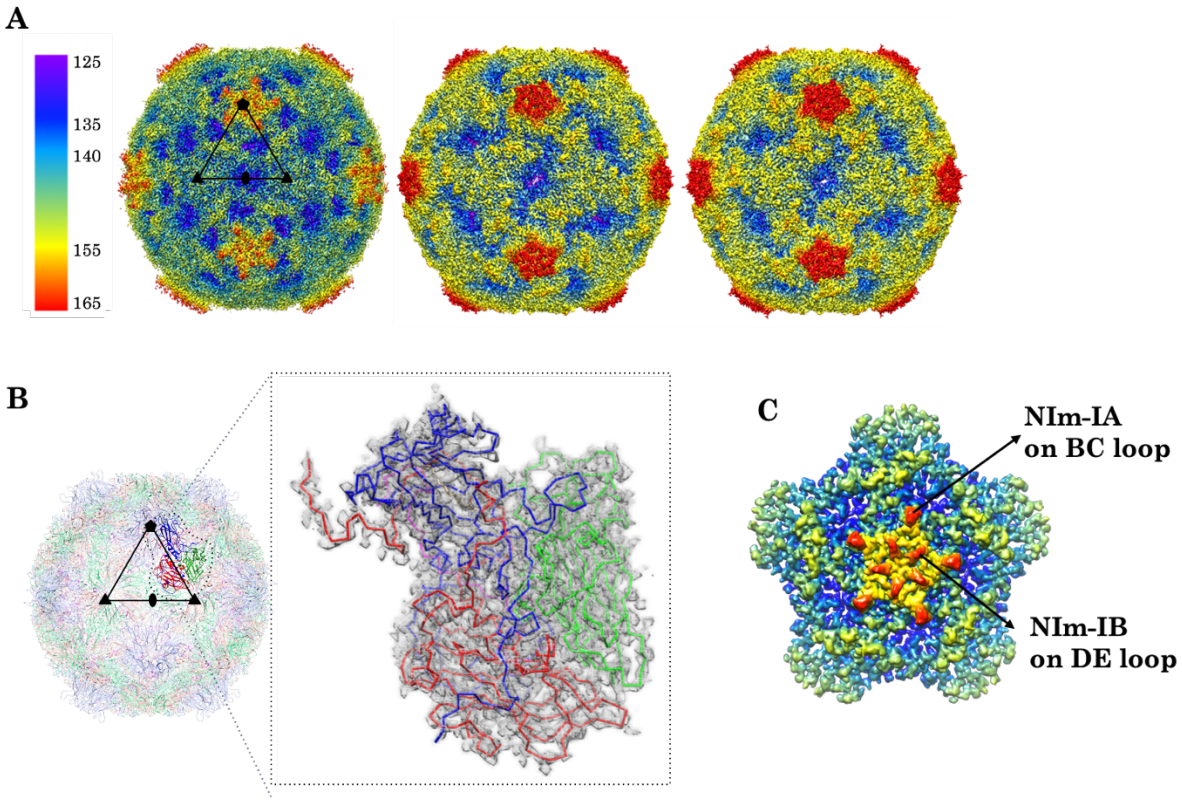


**Fig. 3.2. Structural overview of EV-D94. (A)** Cryo-EM structures of EV-D94 full particle, A-particle and empty particle looking down a two-fold axis. The outline of an icosahedral asymmetric unit of the full particle is represented by a black pentagon, an oval and rectangles, respectively. The holes on the two-fold axes on the A-particle and empty particle are outlined by red circles. **(B)** Ribbon diagram of EV-D94 full particle along a five-fold axis (left). The density of an asymmetric unit is shown in gray with VP1 in blue, VP2 in green, VP3 in red and VP4 shown in magenta (right). **(C)** Two rings of protruding loops at the five-fold axis are surrounded by the canyon regions of EV-D94.

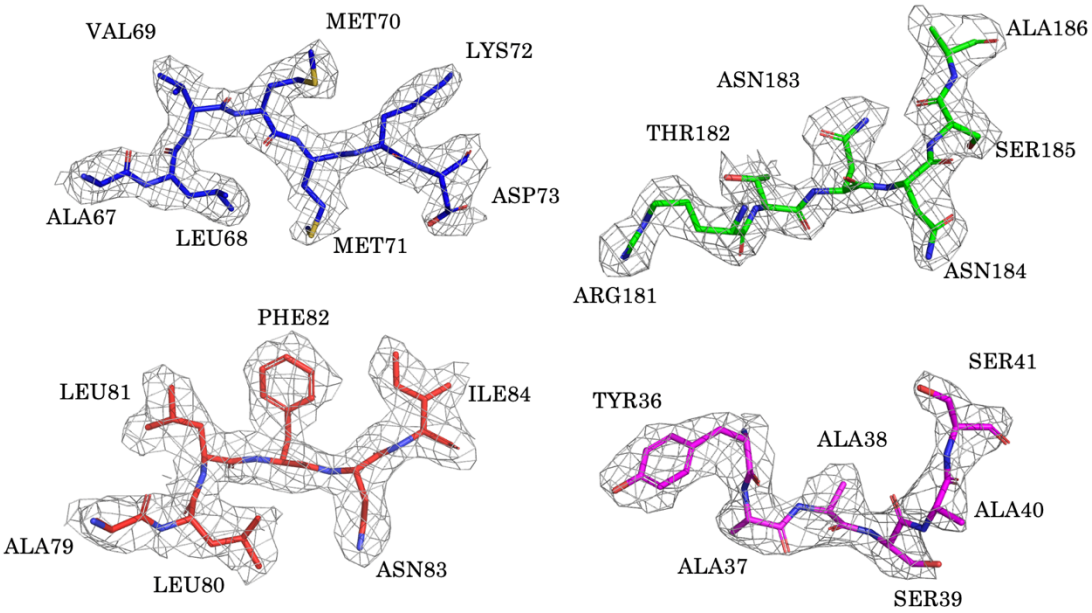


**Fig. 3.3. Electron density map sections from the EV-D94 full particle.** VP1, VP2, VP3 and VP4 are colored in blue, green, red and magenta, respectively.

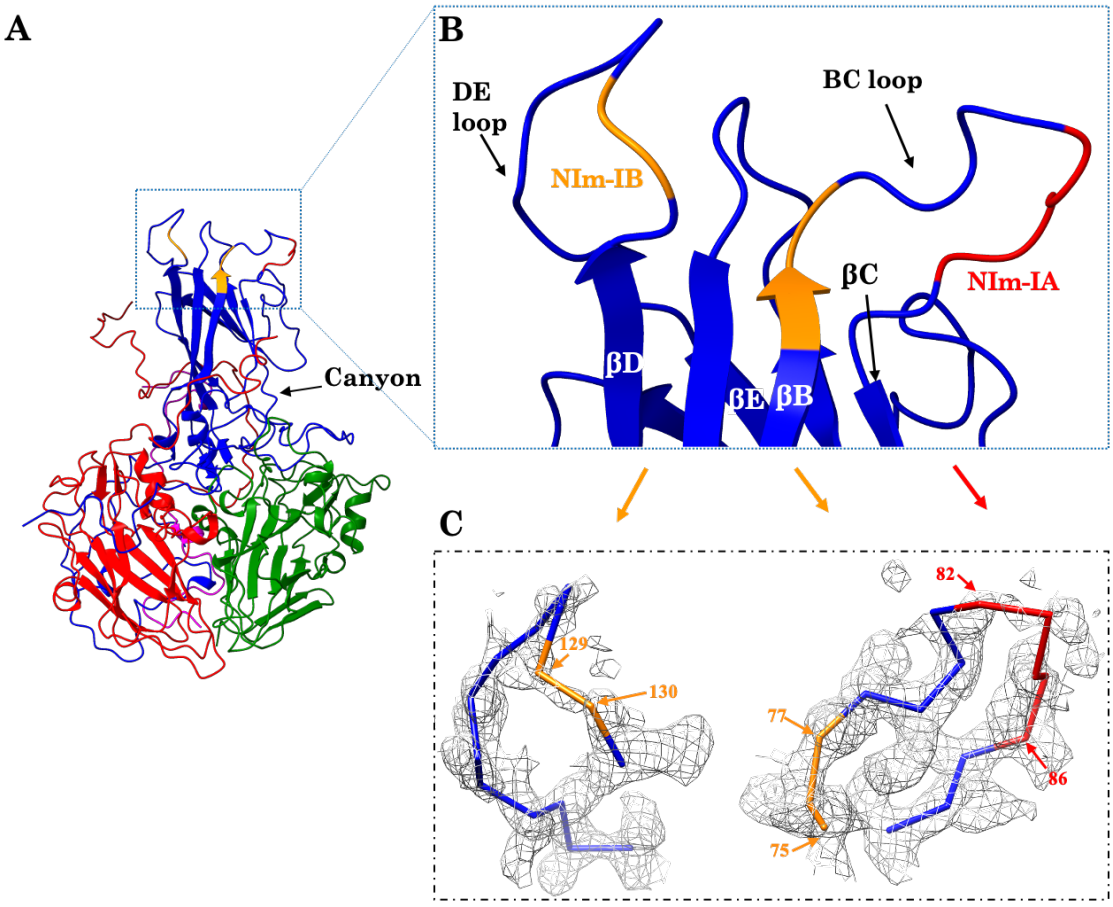


**Fig. 3.4. The VP1 NIm sites viewed from an icosahedral asymmetric unit. (A)** An icosahedral asymmetric unit of the full particle shown as a ribbon. The VPs are colored following the same color scheme as in Figure 3.3. The NIm-IA and NIm-IB regions on the BC and DE loops are colored in red and orange, respectively. **(B)** A closed-up view of the two protruding loops on VP1. Different β-strands, loops and the NIm regions are labeled. **(C)** The Cα backbone of the BC (right panel) and DE (left panel) loops (shown in ribbon) build into the cryo-EM density map (gray). The NIm-IA and NIm-IB regions are colored in red and orange, respectively, and the NIms are labeled.

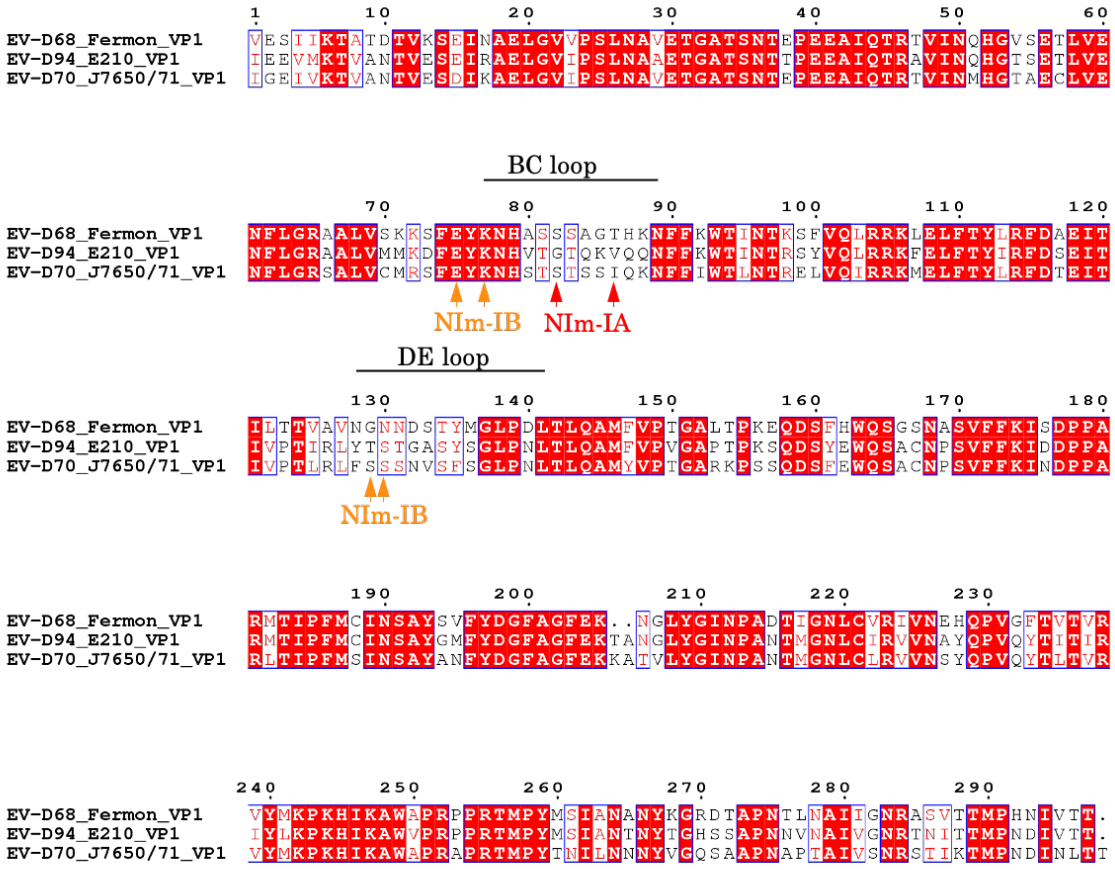


**Fig. 3.5. Sequence alignment of the VP1 proteins of 3 typical viruses from the EV-D species.** The specific residues in NIm-IA and NIm-IB sites are marked in red and orange arrows, respectively. The specific residue positions are based on[2], [23], [86]. The BC and DE loops are labeled based on[2] and previous published EV-D68 structures (PDB: 4wm8, 6crr) and the EV-D94 structure reported here.

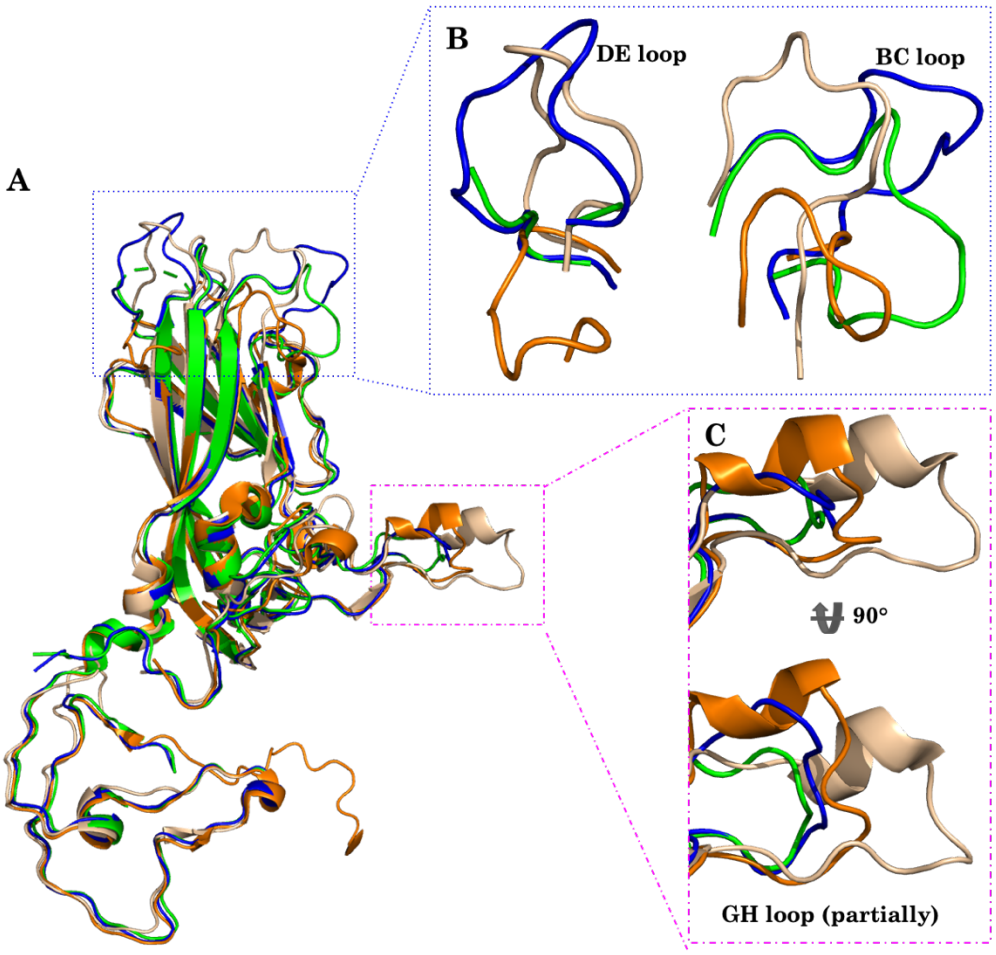


**Fig. 3.6. VP1 comparison between EV-D94 and 3 classical EVs. (A)** Superposition of VP1 of EV-D94, EV-D68[2] (PDB: 4wm8), EV-A71[27] (PDB: 3vbs) and PV-1[178] (PDB:1asj) colored in blue, green, orange and gold, respectively. **(B)** The BC and DE loops are highlighted with a blue box. **(C)** The partial GH loops which form the "south rim" of the canyon are highlighted with a magenta box.

### 3.4.4 The hydrophobic pocket and the pocket factor

The hydrophobic pocket, located underneath the canyon floor, is a common feature in all EV structures. The pocket is usually occupied by pocket factor, which contributes to capsid stability. The same feature is observed in the VP1 pocket of EV-D94. The electron density of the EV-D94 pocket factor shows some discontinuity at a sigma level of 1.0, which may be due to the flexibility in this area of the molecule **(Fig. 3.7A)**. Increasing the sigma level leads to a continuous density located in the pocket. Based on these observations, the pocket factor of EV-D94 is likely to be an 18 carbon-long fatty acid molecule, similar to the pocket factors of EV-A71 and PV-1 **(Fig. 3.7B)**.

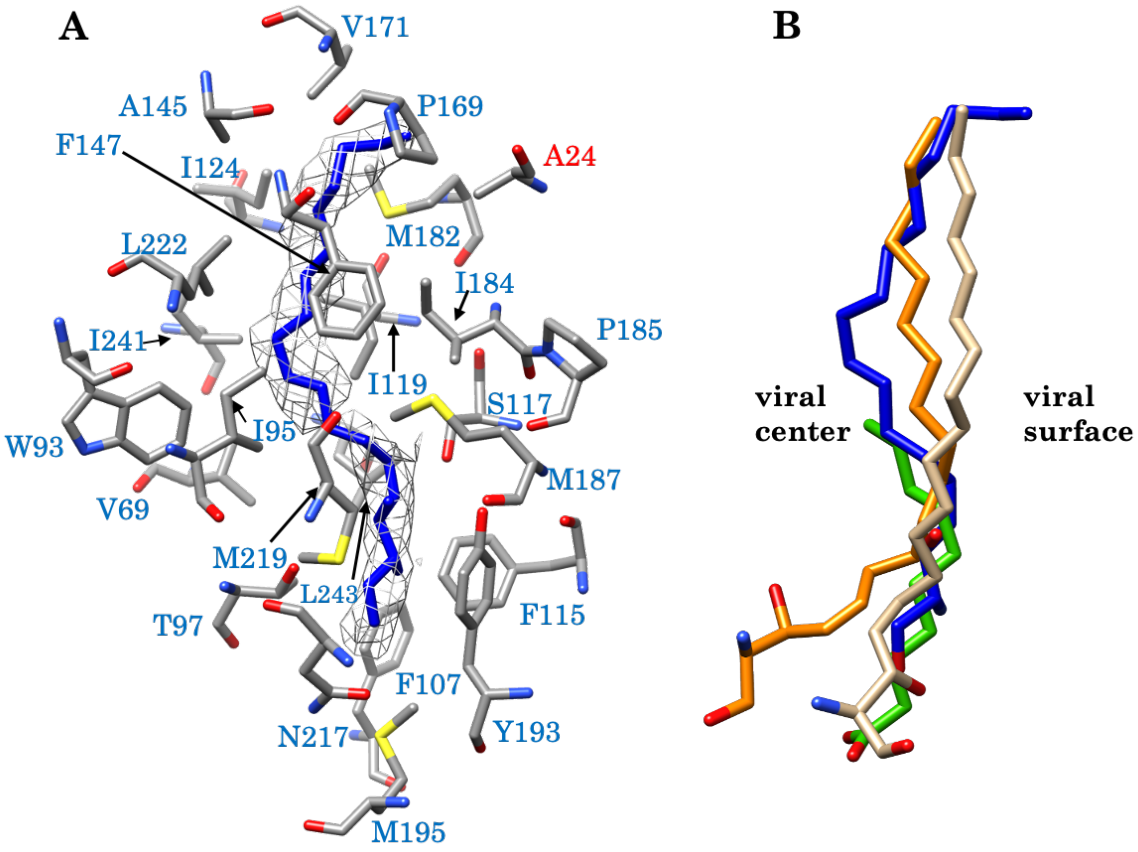


**Fig. 3.7. The EV-D94 pocket factor. (A)** The pocket factor of EV-in the cryo-EM density map together with the residues that are interacting with it. The VP1 residues are labeled in blue and a VP3 residue is labeled in red, corresponding to the color scheme of the VPs used in other figures. Ile184 on VP1 is the residue that defines the orientation of EV-D94 pocket factor. **(B)** Superposition of the pocket factor of EV-D94 (blue), EV-D68 (green), EV-A71 (orange) and PV-1 (gold). EV-D94 contains a pocket factor that is closely related to EV-A71 and PV-1. The citations for EV-D68, EV-A71 and PV-1 are the same as in Fig. 3.6.

Sphingosine ($C_{18}H_{37}NO_2$), the pocket factor identified in EV-A71 and PV-1[26], [179], fits the density observed in EV-D94, but with a slightly different orientation due to the curvature of the density. In contrast, EV-D68 has a shorter pocket factor with only 10 carbon atoms[2] **(Fig. 3.7)**. However, as in EV-D68, the orientation of the EV-D94 pocket factor is controlled by Ile184 **(Fig 3.7A)**. Furthermore, residues that are in contact with the pocket factor are highly conserved between EV-D68 and EV-D94.

### 3.4.5 A conserved site could bind sialic acid

The three most studied EV-D species viruses, EV-D68, EV-D70 and EV-D94, are known to utilize sialic acid as a carbohydrate receptor[180]. The crystal structure of EV-D68 binding sialylated glycan receptor shows that Arg270, Pro274 and Asn275 on VP1, as well as Asp91, Arg95, Arg104, Asp232, Pro231, and Ile233 on VP3 form polar interactions with sialic acid[119]. These residues are conserved within EV-D68 and EV-D94, except for Arg270 in VP1, which is mutated to lysine in some EV-D68 isolates, and to histidine in EV-D94. Furthermore, these residues also show the same orientation in EV-D68 and EV-D94, with the exception of Arg95 in VP3 which has a different configuration in comparison to the other EVs **(Fig. 3.8)**.

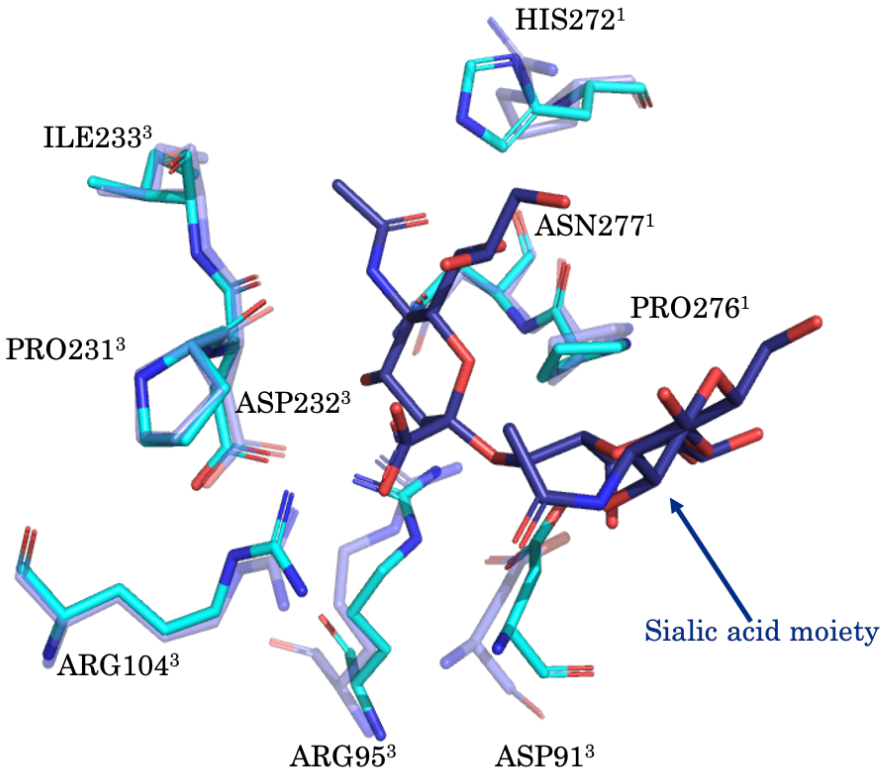


**Fig. 3.8. Superposition of the EV-D94 and EV-D68 residues that interact with the sialic acid moiety.** The EV-D94 and EV-D68 residues are colored in cyan and light purple, respectively, and the sialic acid moiety is colored in navy. The EV-D68 residues and the sialic acid moiety are adapted from[119](PDB: 5bno). Nitrogen and oxygen atoms are colored in blue and red. The VP1 and VP3 residues are indicated with a superscript. The residue labeling is based on EV-D94.

### 3.4.6 The atomic models of EV-D94 A-particle and empty particle

The EV-D94 A-particle **(Fig. 3.2A, Fig. 3.9)** shows the typical conformational changes associated with uncoating described in other EVs[97]. This includes the missing electron densities of VP4, the first 41 residues at the VP1 N-terminus, the pocket factor as well as the externalization of residues 42-52 on VP1. Besides, EV-D94 A-particle also loses the last 26 residues on the VP1 C-terminus and the last 14 residues on the VP3 C-terminus. Furthermore, the VP1 BC and DE loops containing the NIm-IA and NIm-IB sites become disordered **(Fig. 3.9B, C)**. Importantly, the VP1 CD, EF and GH loops shift towards the viral center about 1.5-2.5 Å (Cα atoms unless specified else way) **(Fig. 3.9B, D)**, causing the collapse of the hydrophobic pocket. In VP2, a helix (residue 91-98) at the two-fold axis moves about 1.5 Å away. In addition, the N-terminal region (residue 41-57) and the C-terminus (residue 240-247) which are both close to the two-fold axis become more flexible **(Fig. 3.9E)**. These changes promote an opening at the two-fold axis on a global scale. This opening is also contributed by the VP3 α2 helix on the EF loop (residues 144-151), which moves about 3-4 Å away from the two-fold axis **(Fig. 3.9G)**. The VP3 GH loop, which forms a compact loop in the full particle, is elongated and externalized in the A-particle and interacts with the externalized residues on VP1 N-terminus described above **(Fig. 3.9F)**. Furthermore, the VP3 FG loop becomes more structured and the HI loops of VP2 and VP3 both move 1.5-3 Å towards the three-fold axis **(Fig. 3.9H)**, promoting hydrogen bonding between VP2 and VP3 around the three-fold axis **(Fig. 3.10)**. The A-particle and the empty particle of EV-D94 have high structural similarity to each other, with the major difference between the two is the presence or absence of the genomic material **(Fig. 3.1B)** which likely exits through the pores located at the two-fold axis.

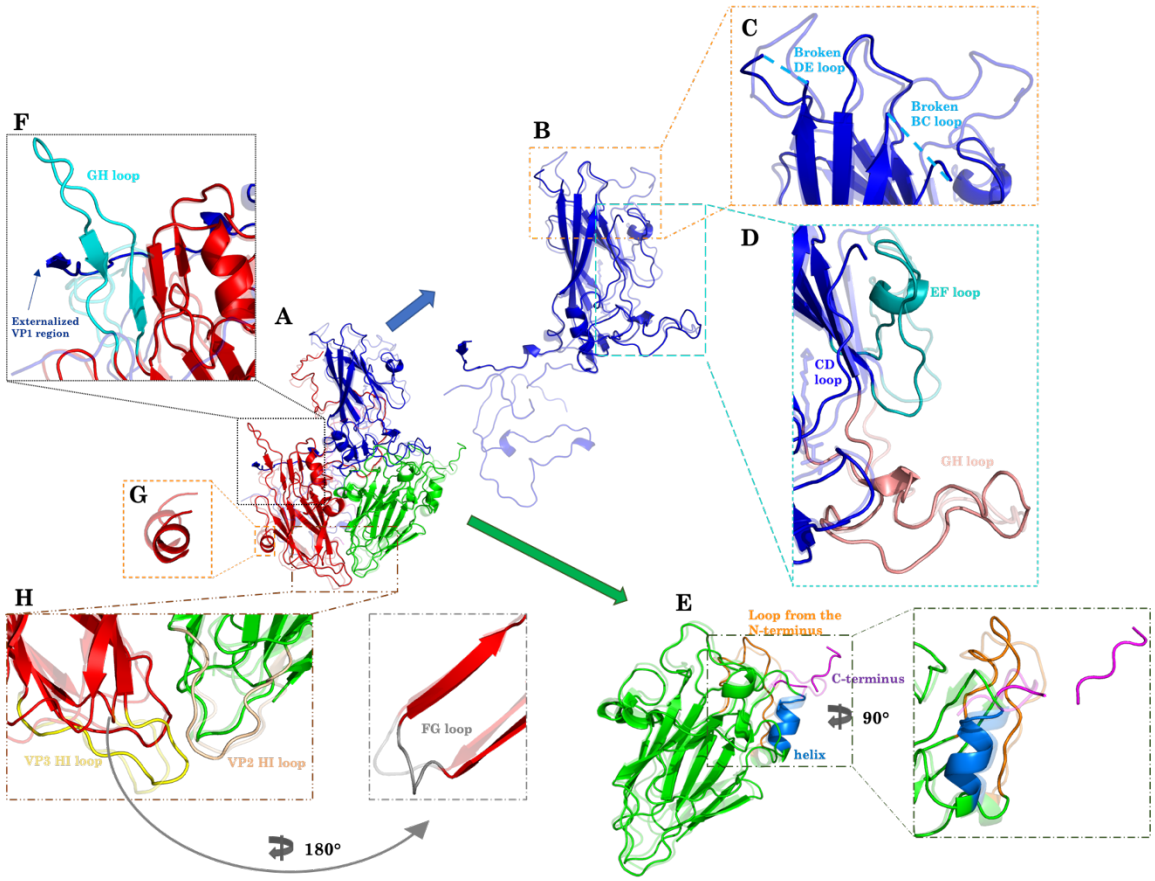


**Fig. 3.9. Comparison between EV-D94 A-particle and full particle. (A)** Superposition of the EV-D94 A-particle and full particle protomers. VP1, VP2 and VP3 are shown in blue, green and red respectively. The chains in the A-particle are shown in bold colors, whereas the ones in the full particle are shown in the same colors with 70% transparency. **(B)** An enlarged view of the VP1 comparison. **(C)** An enlarged view comparing the VP1 BC and DE loops (dash lines indicate broken loops) and **(D)** the VP1 EF (highlighted in teal) and GH loops (pink). **(E)** An enlarged view comparing VP2. The N-terminal region (orange), C-terminus (purple) and the helix (marine) are emphasized. **(F)** An enlarged view comparing VP3 GH loops (cyan), **(G)** α2 helix on EF loop as well as **(H)** Comparison of the region of VP2 HI loop (yellow) and VP3 HI loop (wheat). A view of the VP3 FG loops (grey) is also shown.

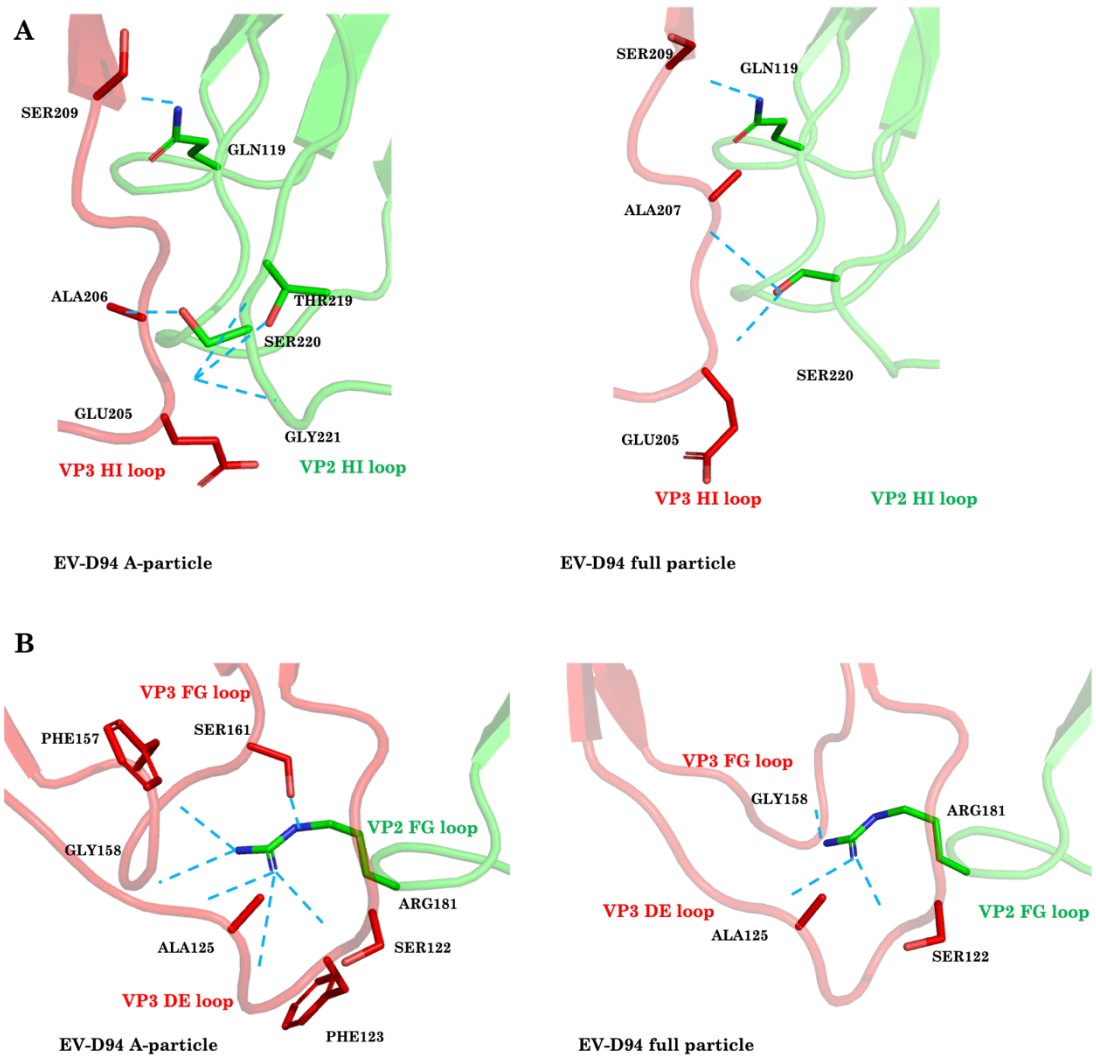


**Fig. 3.10. Potential hydrogen bonds between VP2 and VP3 of EV-D94 A-particle and full particle around the three-fold axis.** Comparisons are done at **(A)** VP2 and VP3 HI loops and **(B)** FG loops. Potential hydrogen bonds are colored in blue, and VP2 and VP3 portions are colored in green and red, respectively.

## 3.5 Discussion

It has been reported that EV-D94 has a broad tissue tropism, including pancreatic islets and human leukocyte cell lines, suggesting that EV-D94 has the potential to directly or indirectly induce type-I diabetes[22]. This altered tissue tropism is affected by receptor usage. For majority of the EVs the "canyon" acts as the receptor binding site[1], [84] and is critical for understanding receptor usage. Even though EV-D94 shares high sequence identity with EV-D68, EV-D94 has an expanded GH loop at the "south rim" of the canyon **(Fig. 3.6C)**, resulting a different canyon shape,

which could indicate a unique receptor usage which may further affect the cell tropism. In addition, even though the receptor of EV-D94 has not yet been identified, a previous study suggested EV-D94 is able to use sialic acid as a carbohydrate receptor like EV-D68[119], [180]. Based on the structure of the EV-D94 full particle, the sialic acid binding site is conserved structurally **(Fig. 3.8)**, suggesting that sialic acid may play an important role during EV-D94 infection.

Another characteristic feature of EVs is their high "plateau" surrounded by a deep "canyon" at each of the five-fold axes. The "plateau" region of EV-D94 contains two protruding loops, the BC and DE loop [23], [86] **(Fig. 3.4)**. These extended loops are not conserved among EVs. For instance, EV-A71 and EV-D68 have less elongated BC loops and short or disordered DE loops **(Fig. 3.6A, B)**, the latter resulting in a small depression at each of the five-fold vertices[2], [27]. However, the BC and DE loops for PV-1[178] are comparable in size to those in EV-D94, pointing towards a potential link between these two neuro-invasive viruses.

Based on the EV-D94 full particle structure, the potential pocket factor of EV-D94 corresponds to a fatty acid molecule with approximately 18 carbon atoms, comparable to what has been described for EV-A71 and PV-1 [26], [27], [178] **(Fig. 3.7)**. Having a longer pocket factor may enhance the stability of EV-D94, since EV-D68 and some rhinoviruses, which are sensitive to the higher temperature and acidic environments[97], [181], [182] contain pocket factors that are either shorter (with 10 to 12 carbon atoms) [2], [71], [183] or potentially absent [23], [184].

The structure of the EV-D94 A-particle indicates an uncoating process structurally similar to other EVs. Importantly, the VP1 CD, EF and GH loops shift towards the viral center **(Fig. 3.9B, D)**, potentially causing the collapse of the hydrophobic pocket and the expulsion of the pocket factor. Moreover, the protein dynamics in VP2 and VP3 promotes the formation of a pore at the two-fold axis, which is presumably used for RNA translocation **(Fig. 3.9E, G)**. The VP3 GH loop is externalized and associated with the externalized VP1 N-terminus, likely facilitating the exit of RNA. Specially, around the three-fold axis, the VP3 FG loop becomes more compact **(Fig 3.9H)**, bringing more hydrogen bonding options with the VP2 FG loop. Additional hydrogen bonds are also found between VP2 and the VP3 HI loop **(Fig. 3.10)**. Due to these shifts, each protomer is more densely packed at the three-fold axis. However, these shifts, at the same time, also cause

separations between the three protomers that meet at the three-fold axis, which may further destabilize the capsid.

The atomic models for EV-D94 full particle, A-particle and empty particle, as reported here, not only introduce structural features of EV-D94, but also establish details of EV uncoating process, which provide meaningful knowledge in developing therapeutic strategies against EV-D94 and other related EVs in the long run.

# 4. STRUCTURAL STUDY OF HUMAN ENTEROVIRUS D68 COMPLEXED WITH AN INHIBITOR

## 4.1 Abstract

Human enterovirus D68 (EV-D68) is one of the leading causes of childhood respiratory diseases and severe EV-D68 infections sometimes lead to polio-like neurological disorders. However, to date there are no antiviral treatments available. Pleconaril, a rhinovirus inhibitor that is also able to bind and inhibit EV-D68 infections, has been used as a template for developing anti-EV compounds. Here, we present the structure of EV-D68 in complex with a recently developed pleconaril derivative. Our initial data shows that this compound binds into the hydrophobic pocket, leading to conformational changes in the canyon region and potentially altering the viral entry process.

## 4.2 Introduction

Enterovirus (EV) is a virus genus which contains various human pathogens, including the widely known poliovirus (PV) and varieties of human rhinoviruses (HRVs). Starting in the 21$^{st}$ century, EV-D68, another member within this genus, has become a notable public health threat worldwide. EV-D68 primarily causes respiratory illness in children, but some central nervous system diseases similar to polio are also found in EV-D68 infections[20], [35], [174], [185]. Currently there are no approved drugs to treat EV-D68 infections.

To develop strategies against viral infection, it is important to understand the structure of a virion. Like other EVs, an EV-D68 capsid is composed of 60 copies of four viral proteins (VPs): VP1, VP2, VP3 and VP4. The VP1, VP2 and VP3 compose the external surface of the capsid following pseudo T=3 icosahedral symmetry[2], [23], [24]. A crevice, called the “canyon”, encircles each of the five-fold axes on the external surface and serves as the receptor binding site during viral entry. Underneath the canyon and in the core of VP1, a hydrophobic pocket is present. For some EVs, a “pocket factor”, a fatty-acid molecule that functions in capsid stability, is found inside the pocket. During viral entry, the host cell receptor binds to the canyon, pushes the canyon

floor and squeezes the pocket, destabilizing and transforming the viral capsid and triggering genome release. If a pocket factor exists, it will be expelled during this process[1], [82], [84].

Many anti-EV inhibitors have been developed based on their potential to bind to the pocket region[1], [186]. These inhibitors are pocket binding molecules which simply fill the empty pocket or compete with the pocket factor to occupy the pocket space in order to stabilize the viral capsid and prevent the virus from uncoating. Furthermore, some of these inhibitors are able to change the shape of the pocket roof, which is also the canyon floor. This change in the canyon can also prevent the virus from binding to receptors, based on the mechanism described above. An example of this type of inhibitor are the WIN compounds developed against some HRVs[1], [102], [105].

Pleconaril, another notable pocket binding molecule, is capable of inhibiting 215 EVs and 90% of HRVs[107], [108]. Importantly, pleconaril has shown high clinical efficiency in adult patients with a common cold[187]. Moreover, pleconaril proved to be an adequate inhibitor against EV-D68 prototype *in vitro* by binding to the pocket and replacing the native short pocket factor[2]. Even though pleconaril was not approved for medical use due to significant side effects[188], [189], studies of pleconaril use against EVs still position the inhibitor as a promising template for the development of anti-EV therapeutics[190], [191]. Especially, some pleconaril derivatives have been generated and tested against EV-D68[189]. Here, we present the 3.3 Å cryo-electron microscopic (cryo-EM) structure of EV-D68 in complex with an inhibitor derived from pleconaril. We show that the inhibitor binds in the hydrophobic pocket of EV-D68 in a manner similar to pleconaril. Importantly, this inhibitor also triggers conformational changes in the canyon region, which potentially interferes with virus binding to receptors.

## 4.3 Materials and methods

### 4.3.1 Cell lines, viruses and inhibitors

Human Rhabdomyosarcoma (RD, CCL-136) cells were purchased from American Type Culture Collection (ATCC) and were used in virus propagation. The RD cell were cultured using Dulbecco's Modified Eagle Medium (DMEM, Sigma-Aldrich) supplied with 10% heat inactivated fetal bovine serum (HI-FBS, Sigma-Aldrich) and 1X non-essential amino acids

(NEAA, Life Technologies). The EV-D68 US/MO/14-18947 strain (EV-D68 MO strain) (GenBank accession no. AIS73051.1) was obtained from BEI Resources, National Institute of Allergy and Infectious Diseases, National Institute of Health. The virus stock was passaged in RD cells and preserved at -80 ℃. The inhibitors (molecule ID: 11526091, 11526092 and 11526093) were supplied by Collaborations Pharmaceuticals, Inc.

### 4.3.2 Propagation and purification of EV-D68

RD cells were cultured at 37 ℃ to 80% confluency and then infected with EV-D68 at a multiplicity of infection (MOI) of around 0.01. Viruses were grown at 33 ℃. After 2 days post infection, the cells and supernatant were harvested and spun down at 9,500 RPM (JA-10 rotor). The cell pellets were collected and lysed by three freeze and thaw cycles and spun down to isolate the virus inside cell debris. Subsequently, all supernatants were spun down at 48,000 RPM (50.2ti rotor) for 2 hours. The pellets were incubated and resuspended in 250 mM HEPES (pH=7.5), 250 mM NaCl buffer and then supplemented with a final concentration of 5 mM $MgCl_2$, 0.01 mg/mL deoxyribonuclease (DNase) (Sigma-Aldrich), 0.8 mg/mL trypsin and 1% (w/v) n-lauryl-sarcosine. After another round of centrifugation at 48,000 RPM (50.2ti rotor) for 2 hours, the resulting pellet was incubated and resuspended in 250 mM HEPES (pH=7.5), 250 mM NaCl buffer and then loaded onto a potassium tartrate gradient (10% to 40%, w/v) and spun down at 36,000 RPM (SW41 rotor) for 2 hours. The purified EV-D68 full particle band was extracted and buffer exchanged against 20mM Tris, 120mM NaCl (pH=8.0) buffer to remove the potassium tartrate.

### 4.3.3 Sample preparation

The inhibitors (molecule ID: 11526091, 11526092 and 11526093) were supplied by Collaborations Pharmaceuticals, Inc. as powder (3 mg each). For each inhibitor, a 10 mg/mL stock solution was made by dissolving the compound in DMSO. The purified EV-D68 full particles (approximately 1 mg/mL in 20mM Tris, 120mM NaCl, pH=8.0 buffer) were split into 3 parts, and each was incubated with a final concentration of 0.2 mg/mL (in PBS) inhibitor (molar ratio 1:2000) at 4 ℃ for 20 hours. 3.5 μL of control (EV-D68 viruses alone) and each of the virus-inhibitor mixtures was applied on a glow-discharged 400 mesh lacey carbon film copper grid (Ted Pella Inc.), blotted for 3.5 seconds at 75% to 80% humidity, and plunge frozen in liquid ethane.

### 4.3.4 Cryo-EM and data processing

Grids were pre-screened using a 200 kV Talos F200C Microscope (Thermo Fisher Scientific). The cryo-EM dataset for the EV-D68-inihibitor-11526093 was collected on a 300 kV Titan Krios Microscope (Thermo Fisher Scientific). A total of 641 movies were collected with a K3 direct electron detection camera (Gatan) at a magnification of 64,000X using the program Leginon[149], with a super resolution pixel size of 0.662 Å. The defocus range varied from 0.7 to 2 µm. A total electron dose of 36.06 electrons/$Å^2$ over 2.6 seconds was split into 50 frames. The dataset was processed using cryoSPARC v2.14.2[192], including the following steps: motion correction, CTF-estimation, particle picking and extraction, 2-dimensional (2D) classification and 3D reconstruction. The final resolution was estimated based on a gold-standard Fourier shell correlation cutoff of 0.143[157]. The X-ray crystallography model of EV-D68 Fermon strain (PDB: 4wm8) was used as a reference model, and was manually built into the EV-D68-inihibitor-11526093 density map using Chimera[100]. The model was adjusted in Coot[158] and refined using PHENIX[159].

## 4.4 Results

### 4.4.1 Virus production and sample screening

Full EV-D68 virus particles were separated by potassium tartrate density gradient and shown as a blue dominant band in the tube **(Fig. 4.1A)**. The purified virus was extracted from the tube and used in preparing a grid for each virus-inhibitor complex and a virus control. The EV-D68 control grid **(Fig. 4.1B)**, together with the grids containing samples of EV-D68 in complex with inhibitor-11526091 **(Fig. 4.1C)**, inhibitor-11526092 and inhibitor-11526093 **(Fig. 4.1D)**, were screened using a 200 kV Talos F200C Microscope. On grids containing EV-D68-inhibitor-11526091 and EV-D68-inhibitor-11526093, viral particles were observed. The particle density of EV-D68-inhibitor-11526093 and the control were similar **(Fig. 4.1D)**, whereas the particle density of EV-D68-inhibitor-11526091 was less than the control **(Fig. 4.1C)**. The grid of EV-D68-inhibitor-11526092 was too icy and no particles were visible.

### 4.4.2 Preliminary results for the binding of inhibitor-11526093

The reconstruction of EV-D68-inihibitor-11526093 complex reached a resolution of 3.3 Å, showing clear electron density for the protein backbone and side chains **(Fig. 4.2)**. However, the density for inhibitor-11526093 **(Fig. 4.3A)** in the VP1 hydrophobic pocket is not as well defined as the density of the four viral proteins and is very fragmented at a reasonable contour level **(Fig. 4.3B)**, indicating the occupancy of the inhibitor may be low. By increasing the sigma levels, the density of the inhibitor becomes better defined, and fitting of the inhibitor molecule is possible **(Fig. 4.3C)**. Compared to the structure of EV-D68 complexed with pleconaril[2] (PDB: 4wm7) **(Fig. 4.4A)**, the inhibitor and pleconaril both bind to the VP1 pocket in a similar manner. Residues in contact with both the inhibitor and pleconaril are conserved. The inhibitor has a few more atoms than pleconaril and associates with slightly more residues. **(Fig. 4.4B)**.

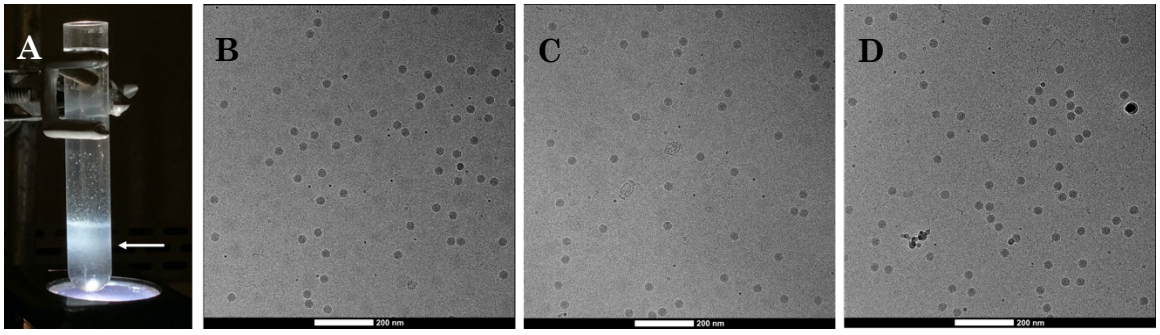


**Fig. 4.1. Virus production and sample screening. (A)** EV-D68 full particles are visible as a dominant blue band (white arrow) after centrifugation. Cryo-EM micrographs of **(B)** EV-D68 control as well as EV-D68 in complex with **(C)** inhibitor-11526091 and **(D)** inhibitor 11526093 are shown at a magnification of 57,000X. The scale bar indicates 200nm. EV-D68-inhibitor-11526093 (D) exhibits a similar particle density to the EV-D68 control (B).

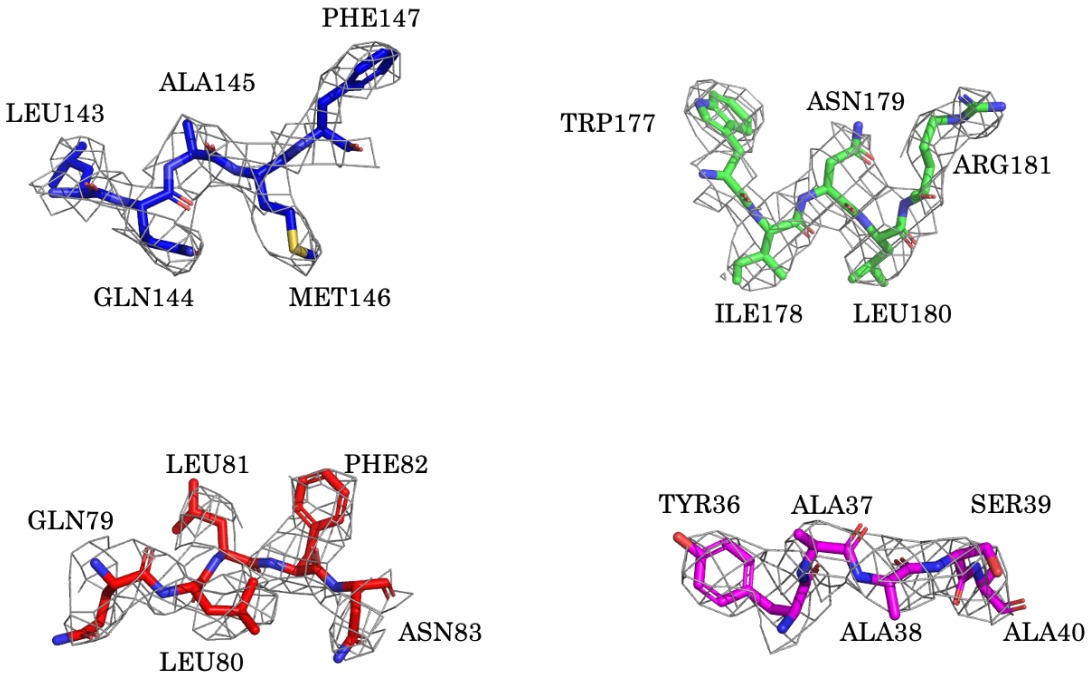


**Fig. 4.2. Representative electron densities of EV-D68-inihibitor-11526093.** The resolution of the complex is 3.3 Å. The backbone and sidechains of the amino acids fit in to the density nicely. VP1, VP2, VP3 and VP4 are colored in blue, green, red and magenta, respectively. VP1, VP2, VP3 and VP4 are colored in blue, green, red and magenta, respectively.

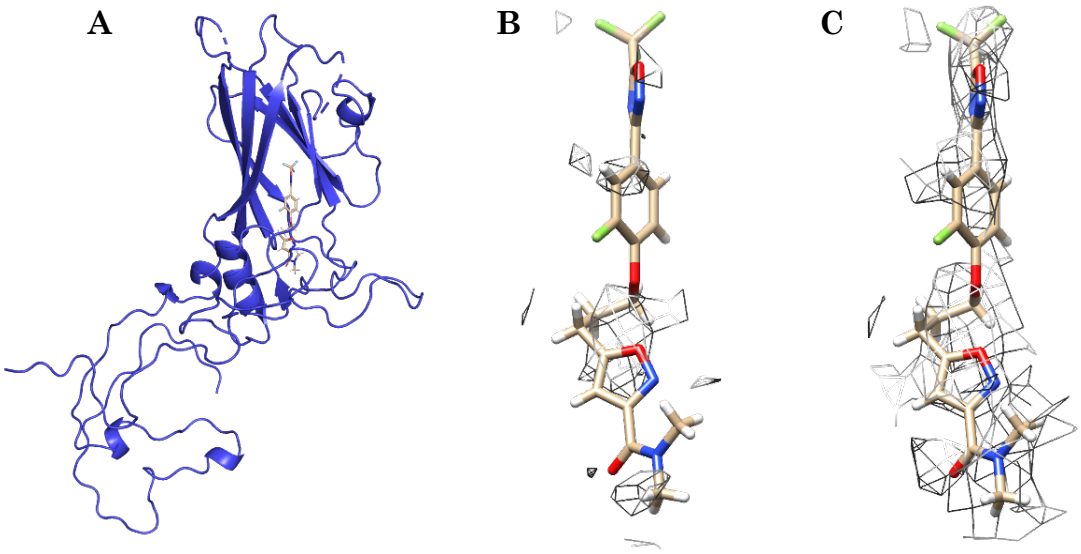


**Fig. 4.3. The binding position and the electron density of inhibitor-11526093 (preliminary data). (A)** The inhibitor was found in the VP1 hydrophobic pocket. **(B)** The electron density of the inhibitor, however, was weaker and less defined compared to the electron densities of the viral proteins. At a contour level around 1 r.m.s.d, the inhibitor density is broken. **(C)** A contour level around 0.6 r.m.s.d allows a better visualization of the inhibitor density. Overall, the weaker density indicates the occupancy of the inhibitor may be low.

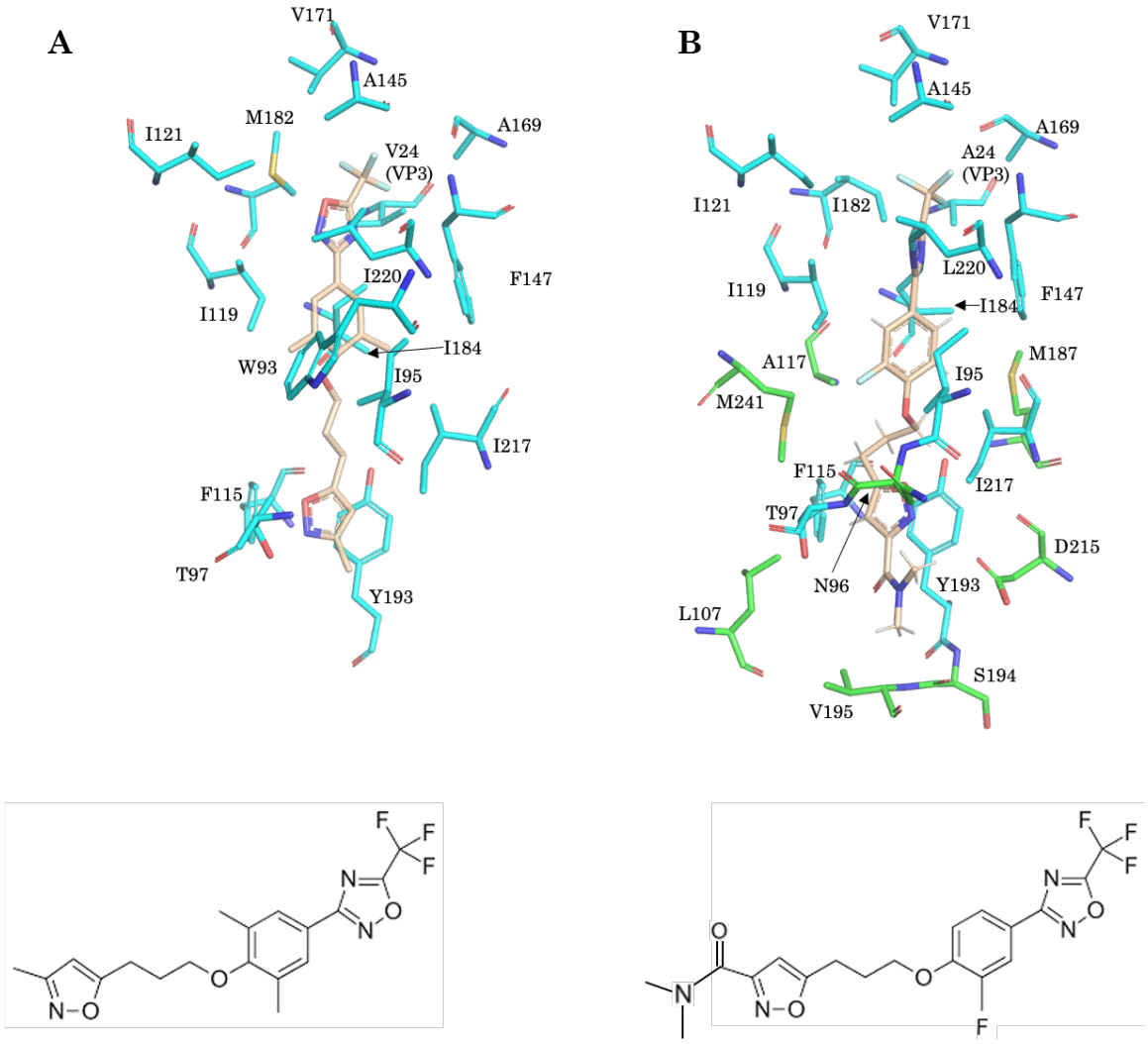


**Fig. 4.4. Structural comparison of EV-D68 complexed with (A) pleconaril (PDB: 4wm7) and (B) inhibitor-11526093.** Residues within a 4 Å distance to any pleconaril or inhibitor-11526093 atoms are presented in the figure. These residues are highly conserved. The inhibitor **(B)** has additional atoms and is associated with more residues. Shared conserved residues are colored in cyan and the additional inhibitor residues are colored in green. Pleconaril and inhibitor-11526093 are colored gold in their respective panels. The chemical structures of the two compounds are presented at the bottom of each panel.

### 4.4.3 Possible dynamics in VP1

Comparison of VP1 of the native EV-D68 MO strain structure[97] (PDB: 6crr) to the EV-D68-inhibitor11526093 structure shows potential dynamic changes in the EF and GH loops **(Fig. 4.5A)**. Residues 213-218 on the GH loop moved approximately 2 Å (measured based on the C$\alpha$ atoms) outward and away from the hydrophobic pocket. Similar movements were observed for

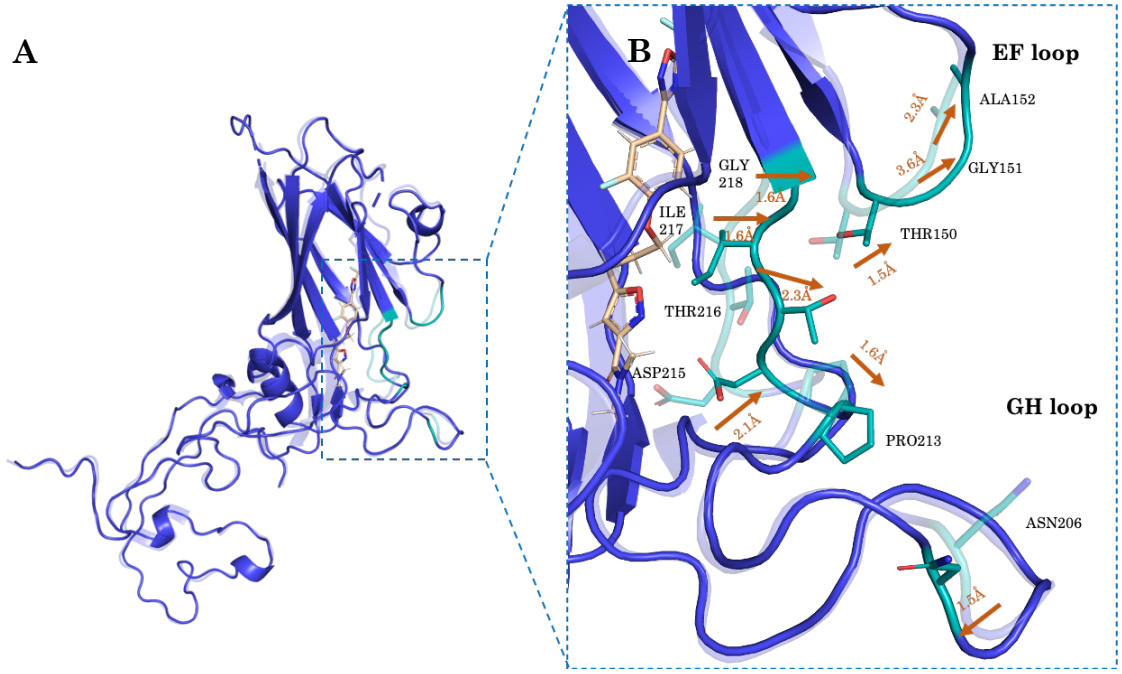


**Fig. 4.5. VP1 comparison: before and after inhibitor-11526093 binding. (A)** Overlaid structural diagrams of the native EV-D68 VP1[97] (PDB: 6crr) and VP1 after inhibitor binding are colored in transparent blue and solid blue, respectively. Inhibitor-11526093 is shown in gold. The observed dynamics are colored in transparent (native) or solid (after inhibitor binding) teal and highlighted in a blue box. **(B)** A zoomed in view of the changes observed on the EF and GH loops. Residues which moved are shown as sticks. Measurements of movement distance of the residues, based on the C$\alpha$ atoms, are provided in orange with accompanying arrows to indicate direction.

residues 150-152 on the EF loop, especially Gly151 which moved 3.6 Å outward. Movement of Asn206 on the GH loop is also visible. Since the GH loop forms much of the canyon and the EF loop is adjacent to the "north rim" of the canyon, these residue shifts described above **(Fig. 4.5B)** presumably bring conformational changes to the canyon region overall.

## 4.5 Discussion

Pleconaril is an efficient pocket binding inhibitor of many EVs[99], [107], [108] including EV-D68[2]. The three inhibitors tested in this study, 11526091, 11526092 and 11526093, were derived from pleconaril. During the screening process, particle density was significantly reduced in the EV-D68-inhibitor-11526091 sample, indicating the potential that inhibitor-11526091 destroys EV-D68 virions at the tested concentration **(Fig. 4.1C)**. The same holds true for inhibitor-11526092 for which no viral particles were visible after incubation. Distortions of the viral particles may change the overall sample conditions, which potentially affect the freezing results. Generally speaking, the binding and freezing conditions for EV-D68-inihibitor-11526091 and EV-D68-inihibitor-11526092 need to be verified in further experiments. The EV-D68-inihibitor-11526093 sample **(Fig. 4.1D)** was the only one selected for data collection and further studies.

Inhibitor-11526093 density was found in the hydrophobic pocket as expected **(Fig. 4.3A)**, since pleconaril is known to bind in the same region while complexing with EV-D68[2]. Residues associated with the inhibitor were also highly conserved when compared to pleconaril [2] **(Fig. 4.4)**, indicating the inhibitor and pleconaril bind EV-D68 in very similar manners. However, unlike what is reported the structure of EV-D68 complexed with pleconaril (the ILE211 on VP1 GH loop moves towards the pocket and possibly blocks the pocket entryway once pleconaril enters[2]), the inhibitor brings more changes on the VP1 GH loop and EF loop presumably by pushing them outward from the pocket. Residues 213-218 on GH loop that not only forms the “north rim” of the canyon, but also locates close to the canyon floor which at the same time acts as the pocket roof[1] that the inhibitor is tightly associated with, have gone through this movement, suggesting that the inhibitor may push the “north rim” of the canyon, which triggers more dynamics in the canyon region that potentially alters receptor binding and affects viral entry **(Fig. 4.5)**. This preliminary result is similar to the HRV-B14 and WIN compound study which shows that pocket space is easily occupied by the WIN compound with the canyon shape changing, leading to an inhibition of the host cell receptor binding[1].

Overall, our results delineate that inhibitor-11526093 possibly occupies the empty pocket of EV-D68 MO strain virus [97] and enlarges the pocket slightly by pushing the GH loop. This may trigger further conformational changes in the canyon region, preventing receptor binding and viral

entry. Even though the occupancy of the inhibitor may be low, there is also a possibility that the inhibitor binds to the pocket, changes the canyon and dissociates from the viral capsid. In general, inhibitor-11526093 shows good potential in the anti-EV-D68 therapeutic field.

# LIST OF REFERENCES


[1] M. G. Rossmann, "Viral cell recognition and entry," *Curr. Sci.*, 1996, doi: 10.1142/9789814513357_0029.

[2] Y. Liu *et al.*, "Structure and inhibition of EV-D68, a virus that causes respiratory illness in children," *Science (80-. ).*, 2015, doi: 10.1126/science.1261962.

[3] CDC-Global Health, "What Is Polio?," *Centers from Disease Control and Prevention*. 2017.

[4] N. A. Ward, "Poliomyelitis: A review," *Trop. Doct.*, 1983, doi: 10.1177/004947558301300108.

[5] B. Trevelyan, M. Smallman-Raynor, and A. D. Cliff, "The spatial dynamics of poliomyelitis in the United States: From epidemic emergence to vaccine-induced retreat, 1910-1971," *Annals of the Association of American Geographers*. 2005, doi: 10.1111/j.1467-8306.2005.00460.x.

[6] M. A. Pallansch, M. S. Oberste, and J. Lindsay Whitton, "Enteroviruses: Polioviruses, coxsackieviruses, echoviruses, and newer enteroviruses," in *Fields Virology: Sixth Edition*, 2013.

[7] M. M. Mehndiratta, P. Mehndiratta, and R. Pande, "Poliomyelitis: Historical Facts, Epidemiology, and Current Challenges in Eradication," *The Neurohospitalist*, 2014, doi: 10.1177/1941874414533352.

[8] B. Snell, D. Balducci, and D. A. J. Tyrrell, "'Polioencephalitis': A Clinical and Laboratory Study," *Br. Med. J.*, 1957, doi: 10.1136/bmj.2.5037.126.

[9] M. S. Oberste, K. Maher, D. R. Kilpatrick, and M. A. Pallansch, "Molecular Evolution of the Human Enteroviruses: Correlation of Serotype with VP1 Sequence and Application to Picornavirus Classification," *J. Virol.*, 1999, doi: 10.1128/jvi.73.3.1941-1948.1999.

[10] M. K. Cooney, J. P. Fox, and G. E. Kenny, "Antigenic groupings of 90 rhinovirus serotypes," *Infect. Immun.*, 1982, doi: 10.1128/iai.37.2.642-647.1982.

[11] M. S. Oberste, K. Maher, D. R. Kilpatrick, M. R. Flemister, B. A. Brown, and M. A. Pallansch, "Typing of human enteroviruses by partial sequencing of VP1," *J. Clin. Microbiol.*, 1999, doi: 10.1128/jcm.37.5.1288-1293.1999.

[12] R. Zell *et al.*, “ICTV virus taxonomy profile: Picornaviridae,” *J. Gen. Virol.*, 2017, doi: 10.1099/jgv.0.000911.

[13] O. S. Nikonov, E. S. Chernykh, M. B. Garber, and E. Y. Nikonova, “Enteroviruses: Classification, diseases they cause, and approaches to development of antiviral drugs,” *Biochemistry (Moscow)*. 2017, doi: 10.1134/S0006297917130041.

[14] V. R. Racaniello, “Picornaviridae: The viruses and their replication,” in *Fields Virology: Sixth Edition*, 2013.

[15] R. Zell, “Picornaviridae—the ever-growing virus family,” *Archives of Virology*. 2018, doi: 10.1007/s00705-017-3614-8.

[16] D. Lugo and P. Krogstad, “Enteroviruses in the early 21st century: New manifestations and challenges,” *Current Opinion in Pediatrics*. 2016, doi: 10.1097/MOP.0000000000000303.

[17] S. Jain, B. Patel, and G. C. Bhatt, “Enteroviral encephalitis in children: Clinical features, pathophysiology, and treatment advances,” *Pathogens and Global Health*. 2014, doi: 10.1179/2047773214Y.0000000145.

[18] A. Muehlenbachs, J. Bhatnagar, and S. R. Zaki, “Tissue tropism, pathology and pathogenesis of enterovirus infection†,” *J. Pathol.*, 2015, doi: 10.1002/path.4438.

[19] P. C. McMinn and P. Van Tu, “Viral CNS Infections: Enterovirus Infections That Cause Central Nervous System Disease (including Poliomyelitis),” in *Hunter’s Tropical Medicine and Emerging Infectious Disease: Ninth Edition*, 2012.

[20] M. S. Oberste *et al.*, “Enterovirus 68 is associated with respiratory illness and shares biological features with both the enteroviruses and the rhinoviruses,” *J. Gen. Virol.*, 2004, doi: 10.1099/vir.0.79925-0.

[21] T. Imamura *et al.*, “Detection of enterovirus 68 in serum from pediatric patients with pneumonia and their clinical outcomes,” *Influenza Other Respi. Viruses*, 2014, doi: 10.1111/irv.12206.

[22] T. Smura *et al.*, “Cellular tropism of human enterovirus D species serotypes EV-94, EV-70, and EV-68 in vitro: Implications for pathogenesis,” *J. Med. Virol.*, 2010, doi: 10.1002/jmv.21894.

[23] M. G. Rossmann *et al.*, “Structure of a human common cold virus and functional relationship to other picornaviruses,” *Nature*, vol. 317, no. 6033, pp. 145–153, 1985, doi: 10.1038/317145a0.

[24] J. M. Hogle, M. Chow, and D. J. Filman, “Three-dimensional structure of poliovirus at 2.9 Å resolution,” *Science (80-. ).*, 1985, doi: 10.1126/science.2994218.

[25] N. Verdaguer, D. Garriga, and I. Fita, “X-Ray crystallography of viruses,” *Subcell. Biochem.*, 2013, doi: 10.1007/978-94-007-6552-8_4.

[26] P. Plevka, R. Perera, J. Cardosa, R. J. Kuhn, and M. G. Rossmann, “Crystal structure of human enterovirus 71,” *Science*. 2012, doi: 10.1126/science.1218713.

[27] X. Wang *et al.*, “A sensor-adaptor mechanism for enterovirus uncoating from structures of EV71,” *Nat. Struct. Mol. Biol.*, 2012, doi: 10.1038/nsmb.2255.

[28] E. Hendry *et al.*, “The crystal structure of coxsackievirus A9: New insights into the uncoating mechanisms of enteroviruses,” *Structure*, 1999, doi: 10.1016/S0969-2126(00)88343-4.

[29] C. Xiao *et al.*, “The crystal structure of coxsackievirus A21 and its interaction with ICAM-1,” *Structure*, 2005, doi: 10.1016/j.str.2005.04.011.

[30] P. Plevka *et al.*, “Interaction of Decay-Accelerating Factor with Echovirus 7,” *J. Virol.*, 2010, doi: 10.1128/jvi.00837-10.

[31] D. Bhella *et al.*, “The Structure of Echovirus Type 12 Bound to a Two-domain Fragment of Its Cellular Attachment Protein Decay-accelerating Factor (CD 55),” *J. Biol. Chem.*, 2004, doi: 10.1074/jbc.M311334200.

[32] M. G. Rossmann, “Structure of viruses: A short history,” *Quarterly Reviews of Biophysics*. 2013, doi: 10.1017/S0033583513000012.

[33] K. M. Jones, S. Balalla, A. Theadom, G. Jackman, and V. L. Feigin, “A systematic review of the worldwide prevalence of survivors of poliomyelitis reported in 31 studies,” *BMJ Open*. 2017, doi: 10.1136/bmjopen-2016-015470.

[34] K. Y. Lee, “Enterovirus 71 infection and neurological complications,” *Korean Journal of Pediatrics*. 2016, doi: 10.3345/kjp.2016.59.10.395.

[35] N. Mishra *et al.*, “Antibodies to enteroviruses in cerebrospinal fluid of patients with acute flaccid myelitis,” *MBio*, 2019, doi: 10.1128/mBio.01903-19.

[36] J. Masa-Calles *et al.*, “Acute flaccid paralysis (AFP) surveillance: challenges and opportunities from 18 years’ experience, Spain, 1998 to 2015,” *Eurosurveillance*, 2018, doi: 10.2807/1560-7917.ES.2018.23.47.1700423.

[37] R. Pebody *et al.*, “An increase in reports of acute flaccid paralysis (AFP) in the United Kingdom, 1 January 2018-21 January 2019: Early findings,” *Eurosurveillance*, 2019, doi: 10.2807/1560-7917.ES.2019.24.6.1900093.

[38] N. McLaren *et al.*, “Characteristics of patients with acute flaccid myelitis, United States, 2015-2018,” *Emerg. Infect. Dis.*, 2020, doi: 10.3201/eid2602.191453.

[39] H. I. Huang and S. R. Shih, “Neurotropic enterovirus infections in the central nervous system,” *Viruses*. 2015, doi: 10.3390/v7112920.

[40] I. Gaaloul *et al.*, “Coxsackievirus B detection in cases of myocarditis, myopericarditis, pericarditis and dilated cardiomyopathy in hospitalized patients,” *Mol. Med. Rep.*, 2014, doi: 10.3892/mmr.2014.2578.

[41] J. Ren *et al.*, “Structures of Coxsackievirus A16 Capsids with Native Antigenicity: Implications for Particle Expansion, Receptor Binding, and Immunogenicity,” *J. Virol.*, 2015, doi: 10.1128/jvi.01102-15.

[42] M. Chen *et al.*, “Epidemiological and genetic characteristics of EV71 in hand, foot, and mouth disease in Guangxi, southern China, from 2010 to 2015,” *PLoS One*, 2017, doi: 10.1371/journal.pone.0188640.

[43] J. Chen *et al.*, “Coxsackievirus A10 atomic structure facilitating the discovery of a broad-spectrum inhibitor against human enteroviruses,” *Cell Discov.*, 2019, doi: 10.1038/s41421-018-0073-7.

[44] J. E. Gern and A. C. Palmenberg, “Rhinoviruses,” in *Fields Virology: Sixth Edition*, 2013.

[45] E. Kieninger, O. Fuchs, P. Latzin, U. Frey, and N. Regamey, “Rhinovirus infections in infancy and early childhood,” *European Respiratory Journal*. 2013, doi: 10.1183/09031936.00203511.

[46] Y. Liu *et al.*, “Atomic structure of a rhinovirus C, a virus species linked to severe childhood asthma,” *Proc. Natl. Acad. Sci. U. S. A.*, 2016, doi: 10.1073/pnas.1606595113.

[47] V. Parikh *et al.*, “Rhinovirus C15 Induces Airway Hyperresponsiveness Via Calcium Mobilization in Airway Smooth Muscle,” *Am. J. Respir. Cell Mol. Biol.*, 2019, doi: 10.1165/rcmb.2019-0004oc.

[48] K. Park *et al.*, “Acute hemorrhagic conjunctivitis epidemic caused by coxsackievirus A24 variants in Korea during 2002-2003,” *J. Med. Virol.*, 2006, doi: 10.1002/jmv.20508.

[49] L. Zhang *et al.*, “Molecular epidemiology of acute hemorrhagic conjunctivitis caused by coxsackie A type 24 variant in China, 2004-2014,” *Sci. Rep.*, 2017, doi: 10.1038/srep45202.

[50] K. Harada, T. Fujimoto, Y. Asato, and E. Uchio, “Virological and epidemiological analysis of coxsackievirus A24 variant epidemic of acute hemorrhagic conjunctivitis in Okinawa, Japan, in 2011,” *Clin. Ophthalmol.*, 2015, doi: 10.2147/OPTH.S81386.

[51] C. G. Sutcliffe and W. J. Moss, “Viral Infections with Cutaneous Lesions: Nonpolio Enterovirus Mucocutaneous Infections,” in *Hunter’s Tropical Medicine and Emerging Infectious Disease: Ninth Edition*, 2012.

[52] N. Mistry, H. Inoue, F. Jamshidi, R. J. Storm, M. S. Oberste, and N. Arnberg, “Coxsackievirus A24 Variant Uses Sialic Acid-Containing O-Linked Glycoconjugates as Cellular Receptors on Human Ocular Cells,” *J. Virol.*, 2011, doi: 10.1128/jvi.05597-11.

[53] K. Sandelin, M. Tuomioja, and H. Erkkilä, “Echovirus Type 7 Isolated from Conjunctival Scrapings,” *Scand. J. Infect. Dis.*, 1977, doi: 10.3109/inf.1977.9.issue-2.03.

[54] H. Jaïdane and D. Hober, “Role of coxsackievirus B4 in the pathogenesis of type 1 diabetes,” *Diabetes and Metabolism*. 2008, doi: 10.1016/j.diabet.2008.05.008.

[55] L. C. Stene *et al.*, “Enterovirus infection and progression from islet autoimmunity to type 1 diabetes: The Diabetes and Autoimmunity Study in the Young (DAISY),” *Diabetes*, 2010, doi: 10.2337/db10-0866.

[56] A. B. Sioofy-Khojine *et al.*, “Molecular epidemiology of enteroviruses in young children at increased risk of type 1 diabetes,” *PLoS One*, 2018, doi: 10.1371/journal.pone.0201959.

[57] S. Brenner and R. W. Horne, “A negative staining method for high resolution electron microscopy of viruses,” *BBA - Biochim. Biophys. Acta*, 1959, doi: 10.1016/0006-3002(59)90237-9.

[58] S. C. Harrison, “Principles of virus structure,” in *Fields Virology: Sixth Edition*, 2013.

[59] S. Yuan *et al.*, “Cryo-EM structure of a herpesvirus capsid at 3.1 Å,” *Science (80-. ).*, 2018, doi: 10.1126/science.aao7283.

[60] L. Zhu *et al.*, “Structures of Coxsackievirus A10 unveil the molecular mechanisms of receptor binding and viral uncoating,” *Nat. Commun.*, 2018, doi: 10.1038/s41467-018-07531-0.

[61] L. Xu *et al.*, “Atomic structures of Coxsackievirus A6 and its complex with a neutralizing antibody,” *Nat. Commun.*, 2017, doi: 10.1038/s41467-017-00477-9.

[62] Q. Fang *et al.*, “Near-atomic structure of a giant virus,” *Nat. Commun.*, 2019, doi: 10.1038/s41467-019-08319-6.

[63] D. Zhou *et al.*, “Unexpected mode of engagement between enterovirus 71 and its receptor SCARB2,” *Nature Microbiology*. 2019, doi: 10.1038/s41564-018-0319-z.

[64] S. S. Hasan *et al.*, “A human antibody against Zika virus crosslinks the E protein to prevent infection,” *Nat. Commun.*, 2017, doi: 10.1038/ncomms14722.

[65] F. Long *et al.*, “Structural basis of a potent human monoclonal antibody against Zika virus targeting a quaternary epitope,” *Proc. Natl. Acad. Sci. U. S. A.*, 2019, doi: 10.1073/pnas.1815432116.

[66] M. G. Rossmann and J. E. Johnson, “Icosahedral RNA Virus Structure,” *Annu. Rev. Biochem.*, 1989, doi: 10.1146/annurev.bi.58.070189.002533.

[67] D. J. Filman, R. Syed, M. Chow, A. J. Macadam, P. D. Minor, and J. M. Hogle, “Structural factors that control conformational transitions and serotype specificity in type 3 poliovirus.,” *EMBO J.*, 1989, doi: 10.1002/j.1460-2075.1989.tb03541.x.

[68] M. Chow, J. F. E. Newman, D. Filman, J. M. Hogle, D. J. Rowlands, and F. Brown, “Myristylation of picornavirus capsid protein VP4 and its structural significance,” *Nature*, vol. 327, no. 6122, pp. 482–486, 1987, doi: 10.1038/327482a0.

[69] A. V. Paul, A. Schultz, S. E. Pincus, S. Oroszlan, and E. Wimmer, “Capsid protein VP4 of poliovirus is N-myristoylated.,” *Proc. Natl. Acad. Sci. U. S. A.*, 1987, doi: 10.1073/pnas.84.22.7827.

[70] A. Panjwani *et al.*, “Capsid Protein VP4 of Human Rhinovirus Induces Membrane Permeability by the Formation of a Size-Selective Multimeric Pore,” *PLoS Pathog.*, 2014, doi: 10.1371/journal.ppat.1004294.

[71] M. A. Oliveira *et al.*, “The structure of human rhinovirus 16,” *Structure*, 1993, doi: 10.1016/0969-2126(93)90008-5.

[72] E. Arnold and M. G. Rossmann, “Analysis of the structure of a common cold virus, human rhinovirus 14, refined at a resolution of 3.0 Å,” *J. Mol. Biol.*, 1990, doi: 10.1016/0022-2836(90)90076-X.

[73] T. D. Goddard *et al.*, “UCSF ChimeraX: Meeting modern challenges in visualization and analysis,” *Protein Sci.*, 2018, doi: 10.1002/pro.3235.

[74] J. K. Lewis, B. Bothner, T. J. Smith, and G. Siuzdak, “Antiviral agent blocks breathing of the common cold virus,” *Proc. Natl. Acad. Sci. U. S. A.*, 1998, doi: 10.1073/pnas.95.12.6774.

[75] N. Reisdorph *et al.*, “Human rhinovirus capsid dynamics is controlled by canyon flexibility,” *Virology*, 2003, doi: 10.1016/S0042-6822(03)00452-5.

[76] J. Baggen, H. J. Thibaut, J. R. P. M. Strating, and F. J. M. Van Kuppeveld, “The life cycle of non-polio enteroviruses and how to target it,” *Nature Reviews Microbiology*. 2018, doi: 10.1038/s41579-018-0005-4.

[77] Q. Li, A. G. Yafal, Y. M. Lee, J. Hogle, and M. Chow, “Poliovirus neutralization by antibodies to internal epitopes of VP4 and VP1 results from reversible exposure of these sequences at physiological temperature.,” *J. Virol.*, 1994, doi: 10.1128/jvi.68.6.3965-3970.1994.

[78] U. Katpally, T.-M. Fu, D. C. Freed, D. R. Casimiro, and T. J. Smith, “Antibodies to the Buried N Terminus of Rhinovirus VP4 Exhibit Cross-Serotypic Neutralization,” *J. Virol.*, 2009, doi: 10.1128/jvi.00557-09.

[79] P. Sauter *et al.*, “A part of the VP4 capsid protein exhibited by coxsackievirus B4 E2 is the target of antibodies contained in plasma from patients with type 1 diabetes,” *J. Med. Virol.*, 2008, doi: 10.1002/jmv.21171.

[80] T. Pulli, H. Lankinen, M. Roivainen, and T. Hyypiä, “Antigenic sites of coxsackievirus A9,” *Virology*, 1998, doi: 10.1006/viro.1997.8908.

[81] M. A. Jiménez-Clavero, A. Douglas, T. Lavery, J. A. Garcia-Ranea, and V. Ley, “Immune recognition of swine vesicular disease virus structural proteins: Novel antigenic regions that are not exposed in the capsid,” *Virology*, 2000, doi: 10.1006/viro.2000.0256.

[82] J. M. Bergelson and C. B. Coyne, “Picornavirus entry,” *Adv. Exp. Med. Biol.*, 2013, doi: 10.1007/978-1-4614-7651-1_2.

[83] U. Katpally and T. J. Smith, “Pocket Factors Are Unlikely To Play a Major Role in the Life Cycle of Human Rhinovirus,” *J. Virol.*, 2007, doi: 10.1128/jvi.00441-07.

[84] M. G. Rossmann, “The canyon hypothesis. Hiding the host cell receptor attachment site on a viral surface from immune surveillance,” *Journal of Biological Chemistry*. 1989.

[85] D. C. Pevear *et al.*, “Conformational change in the floor of the human rhinovirus canyon blocks adsorption to HeLa cell receptors.,” *J. Virol.*, 1989, doi: 10.1128/jvi.63.5.2002-2007.1989.

[86] B. Sherry, A. G. Mosser, R. J. Colonno, and R. R. Rueckert, “Use of monoclonal antibodies to identify four neutralization immunogens on a common cold picornavirus, human rhinovirus 14.,” *J. Virol.*, 1986, doi: 10.1128/jvi.57.1.246-257.1986.

[87] P. D. Minor *et al.*, “Location and primary structure of a major antigenic site for poliovirus neutralization,” *Nature*, 1983, doi: 10.1038/301674a0.

[88] B. Sherry and R. Rueckert, “Evidence for at least two dominant neutralization antigens on human rhinovirus 14.,” *J. Virol.*, 1985, doi: 10.1128/jvi.53.1.137-143.1985.

[89] R. J. Colonno, J. H. Condra, S. Mizutani, P. L. Callahan, M. E. Davies, and M. A. Murcko, “Evidence for the direct involvement of the rhinovirus canyon in receptor binding,” *Proc. Natl. Acad. Sci. U. S. A.*, 1988, doi: 10.1073/pnas.85.15.5449.

[90] P. R. Kolatkar, J. Bella, N. H. Olson, C. M. Bator, T. S. Baker, and M. G. Rossmann, “Structural studies of two rhinovirus serotypes complexed with fragments of their cellular receptor,” *EMBO J.*, 1999, doi: 10.1093/emboj/18.22.6249.

[91] J. Baggen *et al.*, “Role of enhanced receptor engagement in the evolution of a pandemic acute hemorrhagic conjunctivitis virus,” *Proc. Natl. Acad. Sci. U. S. A.*, 2017, doi: 10.1073/pnas.1713284115.

[92] Y. He *et al.*, “Interaction of coxsackievirus B3 with the full length coxsackievirus-adenovirus receptor,” *Nat. Struct. Biol.*, 2001, doi: 10.1038/nsb1001-874.

[93] D. M. Belnap *et al.*, “Three-dimensional structure of poliovirus receptor bound to poliovirus.”

[94] E. Neumann, R. Moser, L. Snyers, D. Blaas, and E. A. Hewat, “A Cellular Receptor of Human Rhinovirus Type 2, the Very-Low-Density Lipoprotein Receptor, Binds to Two Neighboring Proteins of the Viral Capsid,” *J. Virol.*, 2003, doi: 10.1128/jvi.77.15.8504-8511.2003.

[95] Y. A. Bochkov and J. E. Gern, “Rhinoviruses and Their Receptors: Implications for Allergic Disease,” *Current Allergy and Asthma Reports*. 2016, doi: 10.1007/s11882-016-0608-7.

[96] Y. Sun *et al.*, “Cryo-EM structure of rhinovirus C15a bound to its cadherin-related protein 3 receptor,” *Proc. Natl. Acad. Sci. U. S. A.*, 2020, doi: 10.1073/pnas.1921640117.

[97] Y. Liu, J. Sheng, A. L. W. van Vliet, G. Buda, F. J. M. van Kuppeveld, and M. G. Rossmann, “Molecular basis for the acid-initiated uncoating of human enterovirus D68,” *Proc. Natl. Acad. Sci. U. S. A.*, 2018, doi: 10.1073/pnas.1803347115.

[98] J. K. Muckelbauer *et al.*, “The structure of coxsackievirus B3 at 3.5 å resolution,” *Structure*, 1995, doi: 10.1016/S0969-2126(01)00201-5.

[99] Y. Zhang *et al.*, “Structural and Virological Studies of the Stages of Virus Replication That Are Affected by Antirhinovirus Compounds,” *J. Virol.*, 2004, doi: 10.1128/jvi.78.20.11061-11069.2004.

[100] E. F. Pettersen *et al.*, “UCSF Chimera - A visualization system for exploratory research and analysis,” *J. Comput. Chem.*, 2004, doi: 10.1002/jcc.20084.

[101] M. G. Rossmann, Y. He, and R. J. Kuhn, “Picornavirus-receptor interactions,” *Trends in Microbiology*. 2002, doi: 10.1016/S0966-842X(02)02383-1.

[102] G. D. Diana, M. J. Otto, and M. A. McKinlay, “Inhibitors of picornavirus uncoating as antiviral agents,” *Pharmacol. Ther.*, 1985, doi: 10.1016/0163-7258(85)90005-1.

[103] A. G. Mosser and R. R. Rueckert, “WIN 51711-dependent mutants of poliovirus type 3: evidence that virions decay after release from cells unless drug is present.,” *J. Virol.*, 1993, doi: 10.1128/jvi.67.3.1246-1254.1993.

[104] M. S. Smyth and J. H. Martin, “Picornavirus uncoating,” *Journal of Clinical Pathology - Molecular Pathology*. 2002, doi: 10.1136/mp.55.4.214.

[105] C. Xiao, M. A. McKinlay, and M. G. Rossmann, “Chapter 16. Design of Capsid-binding Antiviral Agents Against Human Rhinoviruses,” in *Structural Virology*, 2010.

[106] S. C. Feil *et al.*, “An orally available 3-ethoxybenzisoxazole capsid binder with clinical activity against human rhinovirus,” *ACS Med. Chem. Lett.*, 2012, doi: 10.1021/ml2002955.

[107] R. Dolin, “Miscellaneous Antiviral Agents (Interferons, Imiquimod, Pleconaril),” in *Mandell, Douglas, and Bennett’s Principles and Practice of Infectious Diseases*, 2014.

[108] D. C. Pevear, T. M. Tull, M. E. Seipel, and J. M. Groarke, “Activity of pleconaril against enteroviruses,” *Antimicrob. Agents Chemother.*, 1999, doi: 10.1128/aac.43.9.2109.

[109] A. Tijsma *et al.*, “The capsid binder vapendavir and the novel protease inhibitor SG85 inhibit enterovirus 71 replication,” *Antimicrob. Agents Chemother.*, 2014, doi: 10.1128/AAC.03328-14.

[110] W. Huang *et al.*, “Complete genome sequences of nine enterovirus D68 strains from patients of the Lower Hudson Valley, New York, 2016,” *Genome Announc.*, 2016, doi: 10.1128/genomeA.01394-16.

[111] E. Wimmer, “Genome-linked proteins of viruses,” *Cell*. 1982, doi: 10.1016/0092-8674(82)90335-x.

[112] A. V. Paul and E. Wimmer, “Initiation of protein-primed picornavirus RNA synthesis,” *Virus Res.*, 2015, doi: 10.1016/j.virusres.2014.12.028.

[113] H. B. Pathak, S. O. Hyung, I. G. Goodfellow, J. J. Arnold, and C. E. Cameron, “Picornavirus genome replication: Roles of precursor proteins and rate-limiting steps in oriI-dependent VPg uridylylation,” *J. Biol. Chem.*, 2008, doi: 10.1074/jbc.M806101200.

[114] M. F. Ypma-Wong, P. G. Dewalt, V. H. Johnson, J. G. Lamb, and B. L. Semler, “Protein 3CD is the major poliovirus proteinase responsible for cleavage of the p1 capsid precursor,” *Virology*, 1988, doi: 10.1016/0042-6822(88)90172-9.

[115] C. Badorff *et al.*, “Enteroviral protease 2A cleaves dystrophin: Evidence of cytoskeletal disruption in an acquired cardiomyopathy,” *Nat. Med.*, 1999, doi: 10.1038/6543.

[116] D. Flather and B. L. Semler, “Picornaviruses and nuclear functions: Targeting a cellular compartment distinct from the replication site of a positive-strand RNA virus,” *Frontiers in Microbiology*. 2015, doi: 10.3389/fmicb.2015.00594.

[117] M. Vlasak *et al.*, “The Minor Receptor Group of Human Rhinovirus (HRV) Includes HRV23 and HRV25, but the Presence of a Lysine in the VP1 HI Loop Is Not Sufficient for Receptor Binding,” *J. Virol.*, 2005, doi: 10.1128/jvi.79.12.7389-7395.2005.

[118] W. Wei *et al.*, “ICAM-5/Telencephalin Is a Functional Entry Receptor for Enterovirus D68,” *Cell Host Microbe*, 2016, doi: 10.1016/j.chom.2016.09.013.

[119] Y. Liu *et al.*, “Sialic acid-dependent cell entry of human enterovirus D68,” *Nat. Commun.*, 2015, doi: 10.1038/ncomms9865.

[120] X. Zhao *et al.*, “Human Neonatal Fc Receptor Is the Cellular Uncoating Receptor for Enterovirus B,” *Cell*, 2019, doi: 10.1016/j.cell.2019.04.035.

[121] S. Hafenstein *et al.*, “Interaction of Decay-Accelerating Factor with Coxsackievirus B3,” *J. Virol.*, 2007, doi: 10.1128/jvi.00931-07.

[122] C. B. Coyne and J. M. Bergelson, “Virus-induced Abl and Fyn kinase signals permit coxsackievirus entry through epithelial tight junctions,” *Cell*, 2006, doi: 10.1016/j.cell.2005.10.035.

[123] K. M. Hussain, K. L. J. Leong, M. M. L. Ng, and J. J. H. Chu, “The essential role of clathrin-mediated endocytosis in the infectious entry of human enterovirus 71,” *J. Biol. Chem.*, 2011, doi: 10.1074/jbc.M110.168468.

[124] K. L. Shingler *et al.*, “The Enterovirus 71 A-particle Forms a Gateway to Allow Genome Release: A CryoEM Study of Picornavirus Uncoating,” *PLoS Pathog.*, 2013, doi: 10.1371/journal.ppat.1003240.

[125] K. Lyu *et al.*, “Human Enterovirus 71 Uncoating Captured at Atomic Resolution,” *J. Virol.*, 2014, doi: 10.1128/jvi.03029-13.

[126] Y. Zhao *et al.*, “Hand-foot-and-mouth disease virus receptor KREMEN1 binds the canyon of Coxsackie Virus A10,” *Nat. Commun.*, 2020, doi: 10.1038/s41467-019-13936-2.

[127] S. Yamayoshi, K. Fujii, and S. Koike, “Receptors for enterovirus 71,” *Emerg. Microbes Infect.*, 2014, doi: 10.1038/emi.2014.49.

[128] L. Pérez and L. Carrasco, “Entry of poliovirus into cells does not require a low-pH step.,” *J. Virol.*, 1993, doi: 10.1128/jvi.67.8.4543-4548.1993.

[129] “Activation, Exposure and Penetration of Virally Encoded, Membrane-Active Polypeptides During Non enveloped Virus Entry,” in *Advances in Protein and Peptide Sciences*, 2013.

[130] V. Ambros and D. Baltimore, “Purification and properties of a HeLa cell enzyme able to remove the 5’-terminal protein from poliovirus RNA,” *J. Biol. Chem.*, 1980.

[131] E. Arnold *et al.*, “Implications of the picornavirus capsid structure for polyprotein processing,” *Proc. Natl. Acad. Sci. U. S. A.*, 1987, doi: 10.1073/pnas.84.1.21.

[132] D. Sun *et al.*, “Apoptosis and Autophagy in Picornavirus Infection,” *Frontiers in Microbiology*. 2019, doi: 10.3389/fmicb.2019.02032.

[133] I. H. K. Too *et al.*, “Enterovirus 71 infection of motor neuron-like NSC-34 cells undergoes a non-lytic exit pathway,” *Sci. Rep.*, 2016, doi: 10.1038/srep36983.

[134] H. Cong, N. Du, Y. Yang, L. Song, W. Zhang, and P. Tien, “Enterovirus 71 2B Induces Cell Apoptosis by Directly Inducing the Conformational Activation of the Proapoptotic Protein Bax,” *J. Virol.*, 2016, doi: 10.1128/jvi.01499-16.

[135] S. M. Robinson *et al.*, “Coxsackievirus B Exits the Host Cell in Shed Microvesicles Displaying Autophagosomal Markers,” *PLoS Pathog.*, 2014, doi: 10.1371/journal.ppat.1004045.

[136] C. Zhang *et al.*, “High-yield production of recombinant virus-like particles of enterovirus 71 in Pichia pastoris and their protective efficacy against oral viral challenge in mice,” *Vaccine*, 2015, doi: 10.1016/j.vaccine.2015.03.034.

[137] H. Y. Li, J. F. Han, C. F. Qin, and R. Chen, “Virus-like particles for enterovirus 71 produced from Saccharomyces cerevisiae potently elicits protective immune responses in mice,” *Vaccine*, 2013, doi: 10.1016/j.vaccine.2013.05.019.

[138] F. Zhang *et al.*, “Oral immunization with recombinant enterovirus 71 VP1 formulated with chitosan protects mice against lethal challenge,” *Virol. J.*, 2014, doi: 10.1186/1743-422X-11-80.

[139] F. H. Chen *et al.*, “VP1 of Enterovirus 71 Protects Mice Against Enterovirus 71 and Coxsackievirus B3 in Lethal Challenge Experiment,” *Front. Immunol.*, 2019, doi: 10.3389/fimmu.2019.02564.

[140] P. T. I. Yee and C. L. Poh, “Development of novel vaccines against enterovirus-71,” *Viruses*. 2015, doi: 10.3390/v8010001.

[141] A. M. De Palma, I. Vliegen, E. De Clercq, and J. Neyts, “Selective inhibitors of picornavirus replication,” *Medicinal Research Reviews*. 2008, doi: 10.1002/med.20125.

[142] T. C. Chen, K. F. Weng, S. C. Chang, J. Y. Lin, P. N. Huang, and S. R. Shih, “Development of antiviral agents for enteroviruses,” *Journal of Antimicrobial Chemotherapy*. 2008, doi: 10.1093/jac/dkn424.

[143] P. J. Buontempo *et al.*, “SCH 48973: A potent, broad-spectrum, antienterovirus compound,” *Antimicrob. Agents Chemother.*, 1997, doi: 10.1128/aac.41.6.1220.

[144] M. S. Collett *et al.*, “Antiviral activity of pocapavir in a randomized, blinded, placebo-controlled human oral poliovirus vaccine challenge model,” *J. Infect. Dis.*, 2017, doi: 10.1093/infdis/jiw542.

[145] J. D. Ma, A. N. Nafziger, G. Rhodes, S. Liu, and J. S. Bertino, “Duration of pleconaril effect on cytochrome P450 3A activity in healthy adults using the oral biomarker midazolam,” *Drug Metab. Dispos.*, 2006, doi: 10.1124/dmd.105.007831.

[146] M. R. Vogt *et al.*, “Human antibodies neutralize enterovirus D68 and protect against infection and paralytic disease,” *Sci. Immunol.*, vol. 5, no. 49, pp. 1–13, 2020, doi: 10.1126/sciimmunol.aba4902.

[147] H. Cassidy, R. Poelman, M. Knoester, C. C. V. Leer-Buter, and H. G. M. Niesters, “Enterovirus D68 -the new polio?,” *Frontiers in Microbiology*. 2018, doi: 10.3389/fmicb.2018.02677.

[148] Q. Zheng *et al.*, “Atomic structures of enterovirus D68 in complex with two monoclonal antibodies define distinct mechanisms of viral neutralization,” *Nat. Microbiol.*, 2019, doi: 10.1038/s41564-018-0275-7.

[149] C. Suloway *et al.*, “Automated molecular microscopy: The new Leginon system,” *J. Struct. Biol.*, 2005, doi: 10.1016/j.jsb.2005.03.010.

[150] S. Q. Zheng, E. Palovcak, J. P. Armache, K. A. Verba, Y. Cheng, and D. A. Agard, “MotionCor2: Anisotropic correction of beam-induced motion for improved cryo-electron microscopy,” *Nature Methods*. 2017, doi: 10.1038/nmeth.4193.

[151] G. C. Lander *et al.*, “Appion: An integrated, database-driven pipeline to facilitate EM image processing,” *J. Struct. Biol.*, 2009, doi: 10.1016/j.jsb.2009.01.002.

[152] A. Rohou and N. Grigorieff, “CTFFIND4: Fast and accurate defocus estimation from electron micrographs,” *J. Struct. Biol.*, 2015, doi: 10.1016/j.jsb.2015.08.008.

[153] C. O. S. Sorzano *et al.*, “XMIPP: A new generation of an open-source image processing package for electron microscopy,” *J. Struct. Biol.*, 2004, doi: 10.1016/j.jsb.2004.06.006.

[154] A. M. Roseman, “FindEM - A fast, efficient program for automatic selection of particles from electron micrographs,” in *Journal of Structural Biology*, 2004, doi: 10.1016/j.jsb.2003.11.007.

[155] S. H. W. Scheres, “RELION: Implementation of a Bayesian approach to cryo-EM structure determination,” *J. Struct. Biol.*, 2012, doi: 10.1016/j.jsb.2012.09.006.

[156] F. Guo and W. Jiang, “Single particle cryo-electron microscopy and 3-D reconstruction of viruses,” *Methods Mol. Biol.*, 2014, doi: 10.1007/978-1-62703-776-1_19.

[157] S. H. W. Scheres and S. Chen, “Prevention of overfitting in cryo-EM structure determination,” *Nature Methods*. 2012, doi: 10.1038/nmeth.2115.

[158] P. Emsley, B. Lohkamp, W. G. Scott, and K. Cowtan, “Features and development of Coot,” *Acta Crystallogr. Sect. D Biol. Crystallogr.*, 2010, doi: 10.1107/S0907444910007493.

[159] P. D. Adams *et al.*, “PHENIX: A comprehensive Python-based system for macromolecular structure solution,” *Acta Crystallogr. Sect. D Biol. Crystallogr.*, 2010, doi: 10.1107/S0907444909052925.

[160] L. Potterton *et al.*, “CCP 4 i 2: The new graphical user interface to the CCP 4 program suite,” *Acta Crystallogr. Sect. D Struct. Biol.*, 2018, doi: 10.1107/S2059798317016035.

[161] V. B. Chen *et al.*, “MolProbity: All-atom structure validation for macromolecular crystallography,” *Acta Crystallogr. Sect. D Biol. Crystallogr.*, 2010, doi: 10.1107/S0907444909042073.

[162] A. I. Flyak *et al.*, “HCV Broadly Neutralizing Antibodies Use a CDRH3 Disulfide Motif to Recognize an E2 Glycoprotein Site that Can Be Targeted for Vaccine Design,” *Cell Host Microbe*, 2018, doi: 10.1016/j.chom.2018.10.009.

[163] S. Bangaru *et al.*, “A Site of Vulnerability on the Influenza Virus Hemagglutinin Head Domain Trimer Interface,” *Cell*, 2019, doi: 10.1016/j.cell.2019.04.011.

[164] J. K. Fieldhouse, X. Wang, K. A. Mallinson, R. W. Tsao, and G. C. Gray, “A systematic review of evidence that enteroviruses may be zoonotic,” *Emerging Microbes and Infections*. 2018, doi: 10.1038/s41426-018-0159-1.

[165] L. Royston and C. Tapparel, “Rhinoviruses and respiratory enteroviruses: Not as simple as ABC,” *Viruses*. 2016, doi: 10.3390/v8010016.

[166] R. E. Rhoades, J. M. Tabor-Godwin, G. Tsueng, and R. Feuer, “Enterovirus infections of the central nervous system,” *Virology*. 2011, doi: 10.1016/j.virol.2010.12.014.

[167] N. Junttila *et al.*, “New enteroviruses, EV-93 and EV-94, associated with acute flaccid paralysis in the Democratic Republic of the Congo,” *J. Med. Virol.*, 2007, doi: 10.1002/jmv.20825.

[168] T. P. Smura *et al.*, “Enterovirus 94, a proposed new serotype in human enterovirus species D,” *J. Gen. Virol.*, 2007, doi: 10.1099/vir.0.82510-0.

[169] M. Smyth, T. Pettitt, A. Symonds, and J. Martin, “Identification of the pocket factors in a picornavirus,” *Arch. Virol.*, 2003, doi: 10.1007/s00705-002-0974-4.

[170] C. Xiao *et al.*, “The crystal structure of coxsackievirus A21 and its interaction with ICAM-1,” *Structure*, 2005, doi: 10.1016/j.str.2005.04.011.

[171] Y. He *et al.*, “Interaction of the poliovirus receptor with poliovirus,” *Proc. Natl. Acad. Sci. U. S. A.*, 2000, doi: 10.1073/pnas.97.1.79.

[172] S. Curry, M. Chow, and J. M. Hogle, “The poliovirus 135S particle is infectious.,” *J. Virol.*, 1996, doi: 10.1128/jvi.70.10.7125-7131.1996.

[173] C. Calvo *et al.*, “Respiratory infections by enterovirus D68 in outpatients and inpatients Spanish children,” *Pediatr. Infect. Dis. J.*, 2016, doi: 10.1097/INF.0000000000000908.

[174] Q. Xiao *et al.*, “Prevalence and molecular characterizations of enterovirus D68 among children with acute respiratory infection in China between 2012 and 2014,” *Sci. Rep.*, 2015, doi: 10.1038/srep16639.

[175] M. Knoester, J. Helfferich, R. Poelman, C. Van Leer-Buter, O. F. Brouwer, and H. G. M. Niesters, “Twenty-nine Cases of Enterovirus-D68-associated Acute Flaccid Myelitis in Europe 2016: A Case Series and Epidemiologic Overview,” *Pediatr. Infect. Dis. J.*, 2019, doi: 10.1097/INF.0000000000002188.

[176] A. Dyda, S. Stelzer-Braid, D. Adam, A. A. Chughtai, and C. R. Macintyre, “The association between acute flaccid myelitis (AFM) and enterovirus D68 (EV-D68) – what is the evidence for causation?,” *Eurosurveillance*. 2018, doi: 10.2807/1560-7917.ES.2018.23.3.17-00310.

[177] P. B. Rosenthal and R. Henderson, “Optimal determination of particle orientation, absolute hand, and contrast loss in single-particle electron cryomicroscopy,” *J. Mol. Biol.*, 2003, doi: 10.1016/j.jmb.2003.07.013.

[178] M. W. Wien, S. Curry, D. J. Filman, and J. M. Hogle, “Structural studies of poliovirus mutants that overcome receptor defects,” *Nat. Struct. Biol.*, 1997, doi: 10.1038/nsb0897-666.

[179] J. M. Hogle, “Poliovirus Cell Entry: Common Structural Themes in Viral Cell Entry Pathways,” *Annu. Rev. Microbiol.*, 2002, doi: 10.1146/annurev.micro.56.012302.160757.

[180] J. Baggen *et al.*, “Enterovirus D68 receptor requirements unveiled by haploid genetics,” *Proc. Natl. Acad. Sci. U. S. A.*, 2016, doi: 10.1073/pnas.1524498113.

[181] C. Tapparel, K. Sobo, S. Constant, S. Huang, S. Van Belle, and L. Kaiser, “Growth and characterization of different human rhinovirus C types in three-dimensional human airway epithelia reconstituted in vitro,” *Virology*, 2013, doi: 10.1016/j.virol.2013.06.031.

[182] J. E. Gern *et al.*, “Inhibition of Rhinovirus Replication In Vitro and In Vivo by Acid-Buffered Saline,” *J. Infect. Dis.*, 2007, doi: 10.1086/512858.

[183] N. Verdaguer, D. Blaas, and I. Fita, “Structure of human rhinovirus serotype 2 (HRV2),” *J. Mol. Biol.*, 2000, doi: 10.1006/jmbi.2000.3943.

[184] R. Zhao *et al.*, “Human rhinovirus 3 at 3.0 Å resolution,” *Structure*, 1996, doi: 10.1016/S0969-2126(96)00128-1.

[185] K. Messacar, M. J. Abzug, and S. R. Dominguez, “2014 outbreak of enterovirus D68 in North America,” *J. Med. Virol.*, 2016, doi: 10.1002/jmv.24410.

[186] T. C. Chen, S. C. Liu, P. N. Huang, H. Y. Chang, J. H. Chern, and S. R. Shih, “Antiviral activity of pyridyl imidazolidinones against enterovirus 71 variants,” *J. Biomed. Sci.*, 2008, doi: 10.1007/s11373-007-9228-5.

[187] F. G. Hayden *et al.*, “Oral pleconaril treatment of picornavirus-associated viral respiratory illness in adults: Efficacy and tolerability in phase II clinical trials,” *Antivir. Ther.*, 2002.

[188] F. G. Hayden *et al.*, “Efficacy and Safety of Oral Pleconaril for Treatment of Colds Due to Picornaviruses in Adults: Results of 2 Double-Blind, Randomized, Placebo-Controlled Trials,” *Clin. Infect. Dis.*, 2003, doi: 10.1086/375069.

[189] A. Egorova, E. Kazakova, B. Jahn, S. Ekins, V. Makarov, and M. Schmidtke, “Novel pleconaril derivatives: Influence of substituents in the isoxazole and phenyl rings on the antiviral activity against enteroviruses,” *Eur. J. Med. Chem.*, 2020, doi: 10.1016/j.ejmech.2019.112007.

[190] J. Wald *et al.*, “Cryo-EM structure of pleconaril-resistant rhinovirus-B5 complexed to the antiviral OBR-5-340 reveals unexpected binding site,” *Proc. Natl. Acad. Sci. U. S. A.*, 2019, doi: 10.1073/pnas.1904732116.

[191] A. Bernard, C. Lacroix, M. G. Cabiddu, J. Neyts, P. Leyssen, and R. Pompei, “Exploration of the anti-enterovirus activity of a series of pleconaril/pirodavir-like compounds,” *Antivir. Chem. Chemother.*, 2015, doi: 10.1177/2040206615589035.

[192] A. Punjani, J. L. Rubinstein, D. J. Fleet, and M. A. Brubaker, “CryoSPARC: Algorithms for rapid unsupervised cryo-EM structure determination,” *Nat. Methods*, 2017, doi: 10.1038/nmeth.4169.

# VITA

In 2012, I came to Purdue University for my undergraduate studies and majored in Biological Sciences with a minor in Creative Writing. During my sophomore year, I worked in Dr. Jeffery Lucas' Lab where I assisted with research on songbirds and my work was used in a 2014 publication. But, by the summer of 2014, I was more interested in the microbiology world, especially viruses. I was fortunate to be accepted as an undergraduate researcher in Dr. Michael G. Rossmann's research laboratory where I did an honor's research project on Rubella virus capsid proteins. I completed my bachelor's degree in 2016 and was accepted into Purdue's Graduate Program (honored with a Ross Fellowship and Dr. P.T. Gilham Graduate Award) and joined the Rossmann Lab as a PhD student. There I explored human enteroviruses from the perspective of structural biology, primarily using cryo-electronic microscopy, including aspects of virus morphology, virus and host cell receptor as well as virus and antibody interactions. In July 2020, I was first author on my first publication "Human antibodies neutralize enterovirus D68 and protect against infection and paralytic disease". *Science Immunology* published the paper and also chose to illustrate our work on the cover. I was selected to present the work at the 2020 American Society for Virology meeting and received a student travel award but unfortunately the meeting was instead held online due to the COVID-19 pandemic. With my Ph.D. studies now complete, I look forward to postdoctoral work and continuing my exploration of the wonders and mysteries of structural virology.

# PUBLICATION

Vogt, M.R., **Fu, J**, Kose N., Williamson, L.E., Bombardi, R., Setliff, I., Georgiev, I.S., Klose, T., Rossmann, M.G., Hurst, B.L., Tarbet, E.B, Bochkov, Y.A., Gern, J.E., Kuhn, R.J., Crowe, J.E. "Human antibodies neutralize enterovirus D68 and protect against infection and paralytic disease," *Sci. Immunol.*, vol. 5, no. 49, pp. 1–13, 2020, doi: 10.1126/sciimmunol.aba4902.